

Characterization of $NaAlH_4$ by 1H -NMR

Von der Fakultät für Mathematik und Physik der Universität Stuttgart
zur Erlangung der Würde eines Doktors der Naturwissenschaften
(Dr. rer. nat.) genehmigte Abhandlung

vorgelegt von

Laura Esther Valiente Banuet
geboren in Mexiko Stadt

Hauptberichter : PD Dr. Günter Majer
Mitberichter : Prof. Dr. Gert Denninger
Tag der Einreichung : 10. Januar 2013
Tag der mündlichen Prüfung : 1. März 2013

Max - Planck - Institut für Intelligente Systeme, Stuttgart
2013

Contents

1 About sodium alanate	3
1.1 Hydrogen as fuel for mobile applications	3
1.2 Hydrogen storage possibilities	4
1.3 Sodium alanate ($NaAlH_4$)	7
1.3.1 Structure and usable capacity	8
1.4 Kinetics of the hydrogen desorption process	10
1.4.1 Doping process – Ti -based catalysts	10
1.5 Prior NMR studies on the alanates – Objectives of the present investigations	12
2 NMR theory	15
2.1 Introduction	15
2.2 NMR interactions	16
2.2.1 Dipolar interaction	16
2.3 Equation of motion - Classical treatment	18
2.3.1 Single spin	18
2.3.2 Rotating frame	19
2.3.3 Ensemble of spins	20
2.4 Pulse NMR	20
2.4.1 Single pulse	22
2.5 Hahn echo	23
2.6 Magic echo	25
2.7 Magic-Hahn echo	28
2.8 Relaxation (Bloch equation)	28

2.8.1	Spin - lattice relaxation	29
2.8.2	Spin - spin relaxation	30
2.9	NMR spectra	31
2.9.1	Momenta expansion	31
2.9.2	Motion reduced second moment	32
2.9.3	The Gaussian approximation	33
2.10	Distance determination by NMR in solids	34
2.11	Motional effects	35
3	Experimental set up	39
3.1	Parts of the measurement process	39
4	Experimental and numerical details	45
4.1	Sample preparation	45
4.2	NMR measurements	47
4.2.1	Measurements of the spectra and the Γ_1 rates as a function of temperature	47
4.2.2	Measurements of the spectra and the Γ_1 rates at a given temperature as a function of time	49
4.2.3	Structure determination measurements	50
4.2.4	Overview	51
5	Results	55
5.1	NMR spectra	56
5.1.1	Spectra of $NaAlH_4$, Na_3AlH_6 , and NaH at room temperature	56
5.1.2	Rigid lattice NMR spectra of $NaAlH_4$	58
5.2	NMR studies of hydrogen dynamics in $NaAlH_4$	64
5.2.1	Hydrogen dynamics and the NMR spectra	64
5.2.2	Hydrogen mobility and spin-lattice relaxation	77
5.3	NMR studies of hydrogen desorption on $NaAlH_4$ samples ball-milled with catalyst (at a constant temperature)	91
5.3.1	Hydrogen desorption studied by changes on the NMR spectra	91
5.3.2	Hydrogen desorption studied by spin-lattice relaxation measurements	92

5.3.3	Interpretation of the measurements as a function of time	96
5.4	Structural analysis of $NaAlH_4$ by NMR	97
6	Summary and Conclusions	103
7	Resümee und Zusammenfassung	107
7.1	Notwendige <i>NMR</i> -Theorie	109
7.2	Experimentelle Grundlagen	111
7.3	NMR Messungen – Ergebnisse	112

Abbreviations

BPP-Model	N. Bloembergen, E. M. Purcell and R. V. Pound Model.
CGH₂	Compressed hydrogen gas, with a storage pressure of about 35 – 70 <i>Mpa</i> .
Conf.	Configuration.
cw	Continuous wave.
DSC	Differential Scanning Calorimetry.
DTF	Density functional theory.
FC	Fuel cell.
FID	Free induction decay.
fcc	Faced-centered cubic.
FT	Fourier transform.
FWHM	Full width at half maximum
GGA	Generalized gradient approximation
GKMR	Graduiertenkolleg Magnetische Resonanz - Uni Stuttgart
\hbar	Planck's constant (divided by 2π).
LQH₂	Liquefied hydrogen gas, at 20 K.
LW	Linewidth
MAS	Magic angle spinning.
ME	Magic echo
MHE	Magic-Hahn echo
NMR	Nuclear magnetic resonance
PCU	Power control unit.
PFG	Pulse field gradient.

r.f.	Radio frequency
RT	Room temperature
REDOR	Rotational-echo double-resonance
SEDOR	Spin-echo double-resonance
S/N	Signal-to-noise ratio
SR-PXD	Synchrotron radiation powder X-ray diffraction.
sw	Spectral width
THF	Tetrahydrofuran, whose molecular formula is given by C_4H_8O .
wt.	Weight.
XRD	X-ray diffraction
1, 2 and 5	Sample ball-milled for 30 minutes with 1, 2 and 5 mole %
mole % sample	$Ti_{13} \cdot 6THF$ catalyst.

1 About sodium alanate

The interest in the alanates resurges since they are reconsidered as promising hydrogen storage materials. This can be very easily followed from the committed ongoing search for new energy sources and the existing possibilities to store hydrogen.

1.1 Hydrogen as fuel for mobile applications

Hydrogen itself is an energy carrier and it can be very efficiently transformed into electrical energy. As it is the most abundant element on the Earth, it could thus be an excellent fuel with a very high availability. Unfortunately, most of the hydrogen atoms are chemically bound to oxygen, as H_2O , and to other gaseous, liquid, or solid compounds. In order to be usable, hydrogen must first be splitted e.g. from water. Hydrogen could be the energy carrier of the future, if an environmentally friendly energy source would be used to produce it: a clean source of energy, with a clean exhaust product¹ (see Figure 1.1).

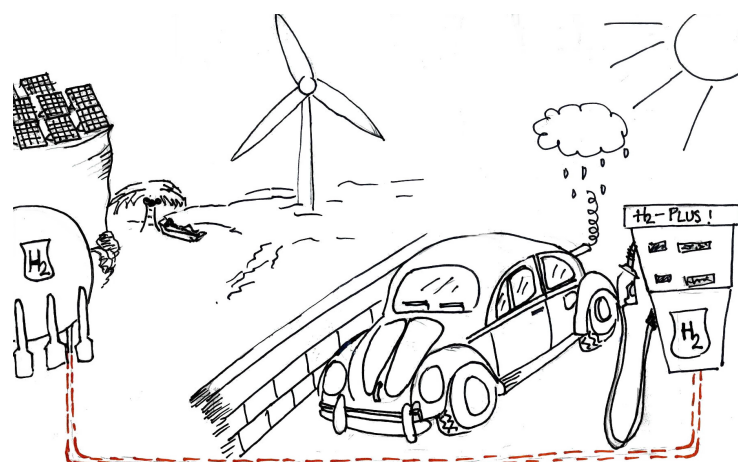


Figure 1.1: The exhaust product of burning the hydrogen together with oxygen is water vapor. Thus hydrogen could be considered a “double-clean energy source” if an environmentally friendly energy source is used to split the water and produce hydrogen.

The chemical energy per mass of the hydrogen (142 MJ kg^{-1}) is at least 3 times larger than that of other chemical fuels (for example, the equivalent value for liquid hydrocarbons is 47 MJ kg^{-1})

¹The exhaust product of hydrogen, by “burning” it electrochemically with oxygen, is water.

[1], [2]. This is because the electrochemical energy is based on the energy of unpaired outer electrons (valence electrons) eager to be stabilized by electrons of other atoms (see Figure 1.2). Each hydrogen has only one proton accompanying the electron (due to its neutrality). It has the best ratio of valence electrons to protons (and neutrons) of all elements in the periodic table. Thus, the energy gain per mass of the hydrogen is very high.

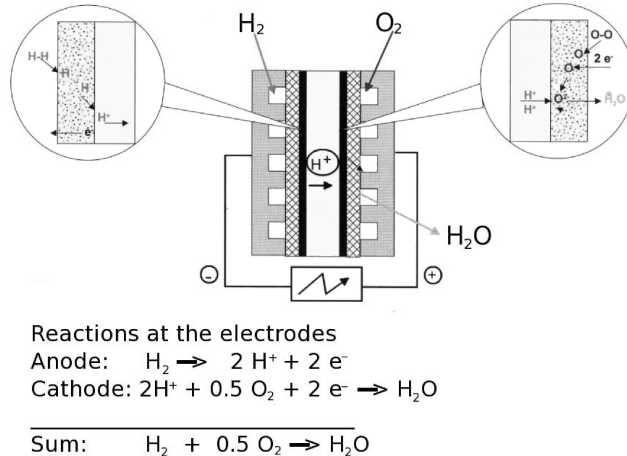


Figure 1.2: Functional principle of a fuel cell (FC) (example of a membrane-FC) [3].

An electrochemical engine, which uses hydrogen as a fuel, produces electricity directly. Therewith, the electricity production has an efficiency not limited by the Carnot cycle². Thus, hydrogen as fuel can be 50 - 60 % more efficient than petrol-air mixtures [1].

The use of hydrogen is therefore considered a possible source of energy for the future, even though there is still the need to find a way how to generate and store hydrogen in an “efficient” way. The topic that bothers us is how to store and transport the hydrogen. This means: how can hydrogen be stored for mobile applications like cars, laptops, mobile phones, etc.?

1.2 Hydrogen storage possibilities

Hydrogen storage systems face a number of problems. In order to store 4 kg of hydrogen at atmospheric pressure (that is the quantity needed in order to drive 400 km with a very average car) we need a tank with 4.4 m diameter³.

Using a hydrogen storage system at high pressure or at very low temperatures (liquid state), less volume is required. Most of the big automobile companies have already produced prototypes running at high pressures (CGH₂: compressed gas with a storage pressure of about 35-70 MPa), or liquefied hydrogen (LH₂: liquid hydrogen at about 20 K). With these cars, one has a similar efficiency to usual cars (max. velocity of 150 km/h and 400 km without refueling need). However, its storage systems, using LH₂ or CGH₂, need also a lot of space for the *operation controllers* of that system. Figure 1.3 shows a prototype of an electrical car from Honda, including the tanks of

²In fact, all electrochemical process are not governed by thermodynamics entropy laws.

³The density of the hydrogen at room temperature is 0.08988 g/l

high pressure hydrogen as fuel together with its *operation controllers*. In both before mentioned storage systems, the needed tank is about three times heavier than those within an average car. Also, it is seven and four times bigger for CGH_2 and LGH_2 , respectively. Thus most of the luggage space has to be sacrificed [4].

Storage systems using LH_2 or CGH_2 face, in addition to the space, more problems. For example, in the case of CGH_2 , the volumetric density does not increase proportionally to the operating pressure as an ideal gas would do. In the case of LH_2 , it is necessary to take into consideration e.g. the effect called *boil-off*. This effect happens when a cryogenic liquid is stored inside the tank. Due to the heat inflow from the outside into the tank, the liquid evaporates constantly. Of course, as the pressure exceeds a given limit, the gas needs to be released through a valve.

Another possibility is to consider the “storage” in hydrogen-rich chemical compounds (e.g. borazane, methanol). This means the decomposition of those compounds into pure hydrogen gas and carbon dioxide. This last possibility however requires the addition of a steam reformer (to extract the hydrogen from the carbon) but also, as already mentioned, it produces the environmentally harmful substance CO_2 . It is hence desirable to find another way to store hydrogen at room temperature, atmospheric pressure, which does not need so much space and which remains environmentally friendly. Several possibilities have been proposed such as:

- activated carbon, carbon nanotubes and carbon nanofibers
- classical metal-hydrides

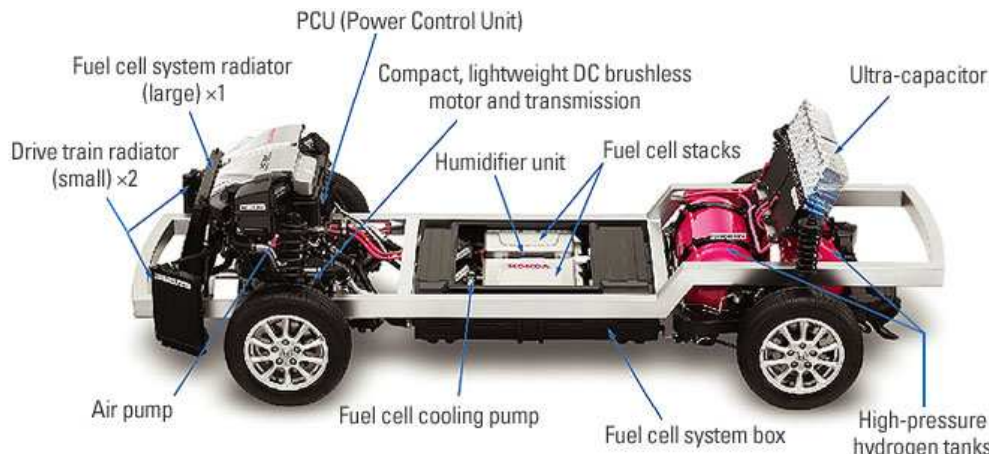


Figure 1.3: Parts of a prototype CGH_2 electric car of Honda [5]. In this case the hydrogen is stored in the “High pressure tanks”. The electricity is generated within the “Fuel cell stacks”. To recycle the water generated by the FC stacks, the “Humidifier unit” is used. The “Power Control Unit” (PCU) regulates the electrical systems (FC stack output, capacitor output, drive motor output, air pump, and the FC cooling pump). This kind of vehicle needs 2 types of cooling systems: the one for the fuel cell itself (“Fuel cell system radiator”) and 2 small drive train radiators (“Drive train radiator”) for the motor. The motor is small and compact with a max. 80 kW (109 PS) and 150 km/h maximum velocity. The “Ultra-capacitor” delivers high-output and assists during start-up or acceleration. It is recharged during breaking.

- complex metal-hydrides

Classical metal-hydrides

The so-called classical metal-hydrides have been considered to be an option for hydrogen storage since quite some time ago. Within this kind of materials, the hydrogen dissociation takes place on the surface of the host metal. The electrons are then transferred into the conduction band of the host metal. The remaining protons diffuse into the bulk and occupy in that way **interstitial sites** of the metal lattice. Hydrogen atoms remain always mobile. Even at ambient conditions, they usually show high diffusion coefficients [6].

The hydrogen is packed in a very dense way in this kind of materials. The minimum distance between the hydrogen atoms would be around 2.1 Å [7], i.e., a high volumetric storage density can be obtained. In this case, we would need a tank with a very similar volume as the tank of a normal car, i.e., of one seventh part of the car shown in Figure 1.3. They are, nevertheless, not so suitable for hydrogen storage because of being so heavy or having very low weight storage densities. At least they are not appropriate for normal applications in which the weight should be as small as possible. Nevertheless, it can be pointed out that the classical metal-hydrides have been in use for submarines for more than a decade. In addition to the weight, most of these materials are quite expensive, too.

The question remains whether there are lighter materials in which hydrogen can be safely stored as in the classical hydrides, with the same volumetric storage capacities, but with higher weight storage capacities?

Carbon materials

Carbon materials were the direct answer to the classical metal hydrides, because they were expected to be able to store in the same way as the classical metal-hydrides – interstitially. But also because of being so light. Everybody expected to achieve a higher weight storage density than with the classical metal hydrides. A lot of effort in several groups (also in ours, see [8]), has been done. However, no one has found a way to store in a reproducible way more than 0.2 wt. % of hydrogen in them.

Mg-based and complex metal-hydrides

Mg-based metal hydrides, together with the so-called complex metal-hydrides have a relatively high volumetric storage density and a high weight storage capacity. In these materials, however, the hydrogen atoms are **bound ionically** and the temperature at which the hydrogen is desorbed is usually very high.

Magnesium hydride, MgH_2 , has the highest hydrogen storage capacity 7.7 wt. % of all known reversible metal-hydrides of this kind. This material is very attractive, as already mentioned, due to its reversibility, high hydrogen storage capacity but also due to its low cost and “good-quality” functional properties: heat resistance, vibration, absorbing, and recyclability. However, in order

to desorb the hydrogen, it is required to go up to 572 K. In order to allow the material to release hydrogen more easily, the material were treated by milling it or by applying a catalyst. By milling, the surface of the material is increased. Micro/nanostructures are formed and also more defects are introduced into the sample. Combining then both treatments (milling and applying an appropriated catalyst) the hydrogen is easier desorbed and temperature of desorption has decreased. Unfortunately without loosing the reversibility, the temperature of desorption has only been reduced up to 502.15 K [9]. A promising onward development of MgH_2 is $Mg(AlH_4)_2$ [10]. This material has a 9.3 wt. % hydrogen content, however, its hydrogen absorption kinetics still needs to be improved [11].

Complex metal-hydrides, specially the alanates and borates (e.g. $NaAlH_4$, $LiBH_4$, $Mg(AlH_4)_2$) are again of special interest because of their relative high volumetric storage density and their high weight storage capacity.

Since 1997, when Bogdanović and Schwickardi [12] dispersed for the first time Ti -based catalysts into sodium tetrahydroaluminate ($NaAlH_4$), they were first considered as a storage material.

The application of catalysts reduces the kinetic barriers for hydrogen release. This means, the desorption temperature of the hydrogen gets lower than without catalyst. Also, the process becomes reversible. Based on these facts, $NaAlH_4$ is considered as a promising hydrogen storage material.

The present work deals with $NaAlH_4$ as a main topic. However, its structure has strong similarities with AGH_4 , where $A = Li, Na, K$ and $G = B, Al, Ga$ [13], [14], [15] or MBH_4 , where $M = Li, Na, K, Rb, Cs$ [16], [17], [18], [19], [20]. At least the hydrogen is often located at the corner of a relatively mobile tetrahedron [9]. Therefrom, the understanding of this compound could help in understanding those other materials.

In the next section, the most important characteristics of sodium alanate are depicted.

1.3 Sodium alanate ($NaAlH_4$)

The industry would like to have a target material with at least 5 wt. % hydrogen storage capacity, and an operating temperature around 300 K⁴. The operating temperature is the one at which the hydrogen will be absorbed or desorbed. The difference in entropy, ΔS , between gaseous and ordered bound hydrogen is always around 100 to 130 J/(KmolH₂). By using the Gibbs energy relation ($\Delta G = \Delta H - T\Delta S$), a reaction enthalpy of about $\Delta H \sim 30 \text{ kJmol}^{-1}H_2$ would be required to get a material with an operating temperature of about 300 K. Thus the hydrogen will be absorbed if $\Delta G < 0$ and consequently desorbed if $\Delta G > 0$. Ti -doped $NaAlH_4/Na_3AlH_6$ has an enthalpy of 37/47 $\text{kJmol}^{-1}H_2$ and an operation temperature of 330 - 440 K. This is the best compromise between storage capacity and the operating temperature of all complex metal-hydrides studied until now [22]. Another important advantage of the sodium alanate is that it is not so expensive.

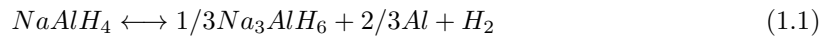
⁴However, for commercial viability it is predicted that the minimum hydrogen-storage capacity must be 6.5 wt. % and 65 g/L hydrogen available, and the decomposition temperature should be between 60 and 120 ° C [9], [21]

The charge and discharge reactions of hydrogen are reversible for $NaAlH_4$ doped with e.g. Ti -based catalysts. The reversibility is, however, not so stable, i.e., part of the H -storage capacity is lost after some cycles.

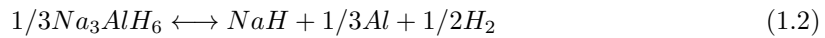
1.3.1 Structure and usable capacity

The thermal decomposition of hydrogen from $NaAlH_4$ occurs in a three-step reaction mechanism. Each step implicates a phase transition and/or a crystal structure modification.

Sodium tetrahydroaluminate - $NaAlH_4$ is transformed into trisodium hexahydroaluminate - Na_3AlH_6 as:



The second step of the decomposition reaction is then given by:



These two decomposition reactions appear to be interdependent as the second transformation commenced only after the first reaction was neared completion [23].

The third decomposition reaction is given by:



During the first two reactions, $NaAlH_4$ and Na_3AlH_6 loose 5.6 wt. % of hydrogen. Since NaH is a very stable compound, we would have to exceed temperatures above 697 K to obtain the rest of the hydrogen [9]. Therefore, the third reaction is not considered for practical applications, and the so-called **usable capacity** remains 5.6 wt. %.

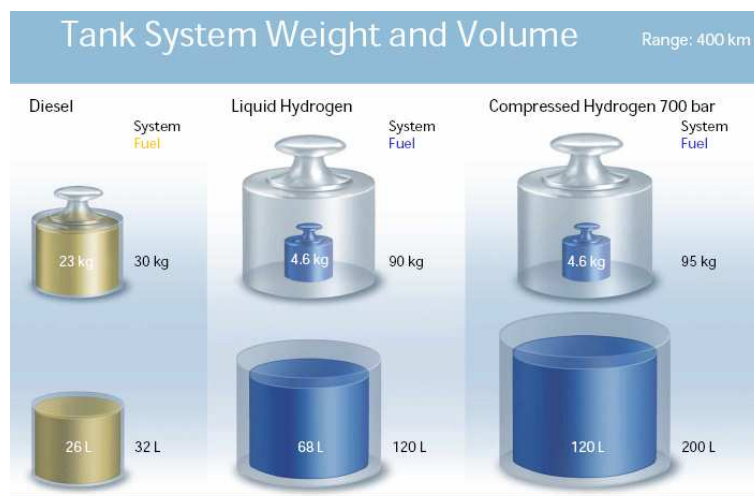


Figure 1.4: Tank systems weight and volume [4]

Coming back to the applicability, in 2006 GM was already producing hydrogen cars with a performance of 400 km without tanking (see Figure 1.4). This systems need, as the figure shows, a tank of 120 or 200 l for $CGLH_2$ and LH_2 respectively. Both tanks have a weight of about 90 kg. That figure does not show the controllers needed for the e.g. cryogenic state of the gas in the LH_2 though. With the hydrogen capacity of $NaAlH_4$ a tank with 4.6 kg usable hydrogen (as in the figure) will need a tank with a volume of 54.8 l and it will weigh 80 kg in total, without so many extra components (see Figure 1.3) or without so high pressures. Thus, by using $NaAlH_4$ one can store hydrogen in a safe and compact way.

$NaAlH_4$ has tetragonal crystal structure, with $a = 5.0119(1)$ Å and $c = 11.3147(5)$ Å. Its space group is $I4_1/a$ [24], [25], [26]. Around each Al atom there are four hydrogen atoms forming a tetrahedron (see Figure 1.5).

The position of the hydrogen atoms are assumed to correspond one to one with the positions of the deuteron atoms in $NaAlD_4$ and were obtained from a Rietveld-type refinements of powder neutron diffraction data [27], [26]. According to those measurements each face of a tetrahedron point toward the face of the first neighbor tetrahedron. The faces are then parallel but inverted. We denote this configuration as $\triangle\triangledown$ -Conf. In the last both references (in Refs. [27] and [26]) the shortest $Al - D$ and $D - D$ bond lengths are 1.626(2) Å and 2.619(1) Å, respectively.

Ab initio calculations of the lattice parameters based on a generalized gradient approximation (GGA) were in good agreement with the data obtained by Rietveld refinement of X-ray and neutron diffraction data. The GGA calculations yielded for the shortest bond lengths 1.631 Å for $Al - H$ bond length and 2.631 Å for the $H - H$ bond length [26].

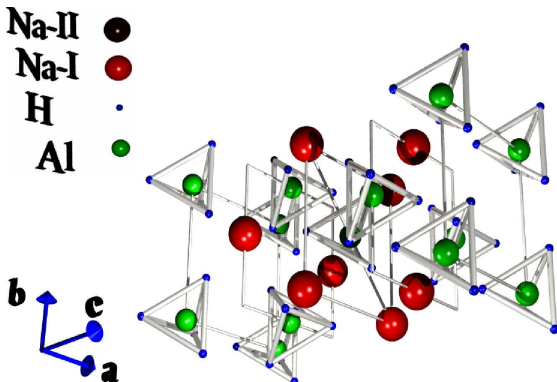


Figure 1.5: Structure of $NaAlH_4$. Al – green, Na – red and H – blue atoms

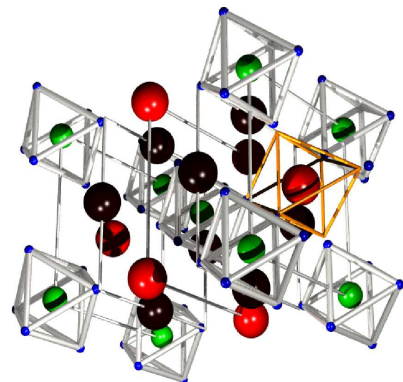


Figure 1.6: Structure of Na_3AlH_6 . Al – green, Na^I – red, Na^{II} – black and H – blue

The structure of Na_3AlH_6 is shown on the Figure 1.6. As it can be seen, the hydrogen atoms are arranged in an octahedral structure around the Al atoms. The structure altogether can be described as a pseudo-cubic arrangement of octahedra AlH_6 with 1/3 of the Na atoms in six-fold coordination ($Na - I$) and 2/3 of Na atoms eight-fold coordinated ($Na - II$) [13]. The lattice parameters are given by $a = 5.408(2)$, $b = 5.538(2)$, $c = 7.757(2)$ Å and $\beta = 89.83(2)^\circ$.

The positions of the hydrogen atoms were deduced from the positions determined on a **deuterated sample** – Na_3AlD_6 [13]. The structure has a $P2_1/n$ space group. The shared corners between

AlH_6 and $Na^I H_6$ can be clearly observed in Figure 1.6 (orange octahedron). One of the C_4 -axis of the AlH_6 -octahedra are expected to be almost parallel to the c -axis of the crystal. Almost parallel because the before mentioned C_4 -axis should be just a bit tilted to c -axis. However, E. Rönnebro *et al.* did not specify the angle. They just mentioned that the octahedra appear to be *less tilted but more deformed* [28]. The distances between the Al and D atoms within the octahedron are, according to the deformation, 1.746, 1.758 and 1.770 Å. This configuration or distortion of the octahedra is also expected in Na_3AlH_6 , from the results obtained by H. Yukawa [29] with Raman spectroscopy.

NaH has a face-centered cubic (fcc) structure, in analogy to the structure of $NaCl$.

1.4 Kinetics of the hydrogen desorption process

In order to speed up the kinetic of the desorption, the samples were ball milled (see Section 4.1). In this way defects are created on the surface and in the interior of the material. This provides sites with low activation energy for diffusion.

Also, by milling the surface area is increased. As the desorbed hydrogen comes mainly from the surface of the material, milling makes the process more efficient [9], i.e., faster.

Catalysts have the function of making the hydrogen desorption of the alanates even much faster. Furthermore, the use of catalyst reduces the desorption temperature and makes the process of hydrogen release reversible. To increase the surface contact, the catalyst is usually dispersed into the system by ball milling.

1.4.1 Doping process – Ti –based catalysts

Several catalysts were studied in screening experiments like $Zr(OPr^i)_4$ (zirconium tetra-n-propoxide), Zr (see e.g. [30], [31], [32]), Pt -powder [33], etc. However, none of them have had such a good efficiency as the Ti –based catalysts like $Ti(Obu^n)_4$ (titanium tetra-n-butoxide) [34], $TiCl_3$ [35], $Ti_{13} \cdot 6\text{THF}$ (THF – tetrahydrofuran, is given by C_4H_8O) [36], [37], $TiCl_2$ [38], TiF_3 [38], [39], $TiBr_4$ [38], Ti/Fe -catalyst [31].

The type and amount of catalyst introduced had an effect on the different critical temperatures, at which the hydrogen was released. The catalysts that we have used until now are $TiCl_3$ and $Ti_{13} \cdot 6\text{THF}$. For both catalysts, the hydrogen desorption and absorption is the faster the more catalyst was used [35], [36].

Figure 1.7 shows the hydrogen thermal desorption of $NaAlH_4$ with those catalysts at 150 °C [36]. The hydrogen desorption curves of the three cases show a stepwise form. This two-step process is described by the equations (1.1) and (1.2). In this figure, a sample with 0.9 mole % $Ti_{13} \cdot 6\text{THF}$ desorbed already 80 % of its hydrogen usable capacity in no more than 1 hour. In contrast the same process on a similar sample but with 1.8 mole % of the same catalyst lasted about 13 minutes. The sample with 2 mole % of $TiCl_3$ needed almost one hour. The hydrogen is desorbed more efficiently using $Ti_{13} \cdot 6\text{THF}$ than $TiCl_3$.

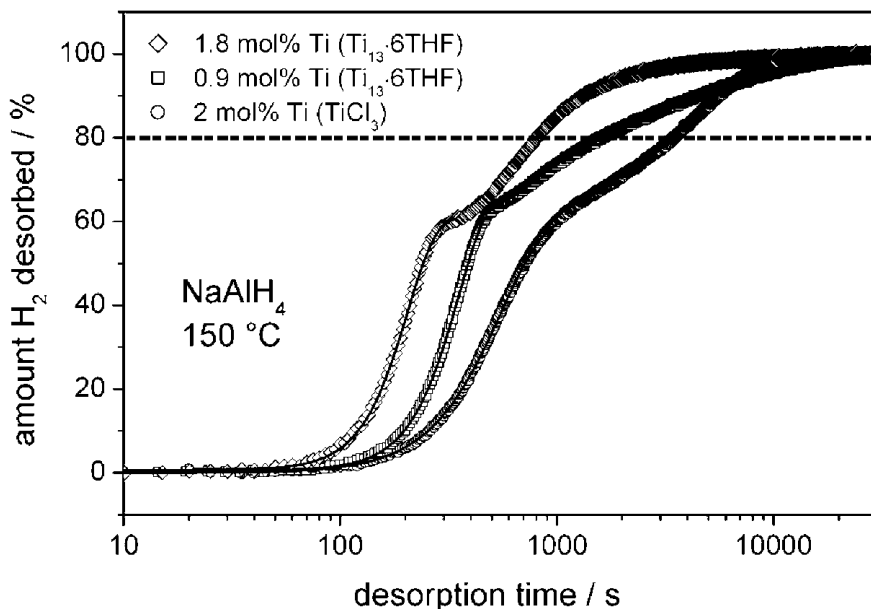


Figure 1.7: Dehydrogenation of NaAlH_4 samples doped with 0.9 and 1.8 mole % $\text{Ti}_{13} \cdot 6\text{THF}$, so as 2 mole % of TiCl_3 [36].

It is believed the Ti -based catalysts produces lattice distortion [40], [9]. When Na^+ or Al^+ ions are substituted by Ti cations, the dopant attracts a large number of hydrogen atoms to its vicinity (up to eight). However, none of them should be tightly bound to facilitate H_2 formation and its release. There is, however, no really persuasive experimental proof of that hypothesis. On the contrary, ab-initio density functional theory (DFT) calculations of titanium solubility in NaAlH_4 found this theory to be thermodynamically unfavorable [41]. From this reference, the substitution of Na or Al would cause lattice parameters to decrease in contradiction with the experimental observations. The role of titanium added in NaAlH_4 is expected to be not of doping but of catalyzing (the formation of TiAl_3 was thermodynamically favorable).

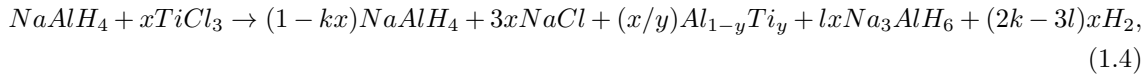
In the following two sections, further information about the two catalysts we used in our laboratory (TiCl_3 and $\text{Ti}_{13} \cdot 6\text{THF}$) is provided.

TiCl_3 catalyst

TiCl_3 was the first Ti -based catalyst that we used in our Laboratory. In terms of hydrogen diffusion, it is not as efficient as $\text{Ti}_{13} \cdot 6\text{THF}$ (see Figure 1.7). As usual, this catalyst is dispersed into the sample via ball milling.

Despite the fact that reversibility had been achieved using catalysts, the storage capacity decreased after several cycles. This was specially observed in the case of TiCl_3 . A possible explanation of why this happens was given by H. Brinks *et al.* [42]. By using a “synchrotron radiation powder X-ray diffraction” (**SR-PXD**) study, they found some indications that a $\text{Al}_{1-y}\text{Ti}_y$ phase, with $y = 0.07$ could be formed. According to this data, they proposed that the hydrogen desorption of the sample of NaAlH_4 with 1 mole % TiCl_3 is going to follow the reactions not given by Equation

(1.1) anymore, but [42]



with $k \sim 1.53$, $k = (3 - 6y)/2y$, and $l = (1 - y)/2y - 3/2$. $NaCl$ was also found in Ref. [43]. The re-absorption should still satisfy Eq. (1.1). After repeated re-absorptions, **there is only a small fraction of free Al left to react** with Na_3AlH_6 . Therefore the successive formation of $NaAlH_4$ is hindered. As a consequence the original hydrogen storage capacity decreases dramatically due to the extra system components. This means an extra dead weight due to the additive and its sub-products will be added such that e.g. with 2 mole wt. % of $TiCl_3$, the original capacity will be reduced 16 % of its original capacity (5.6 wt. %). This yields a maximal storage capacity of only 4.73 wt. % after one cycle. Similar decrements of the hydrogen storage capacities were also found for other catalyst like for example in $Ti(OBu^n)_4$ [44], [45].

$Ti_{13} \cdot 6THF$ catalyst

In 2003 two different groups of researchers almost simultaneously proposed to use $Ti_{13} \cdot 6THF$ as catalyst (see [37], [36]). Regardless of who found it first, the results were very exciting. The times for hydrogen desorption and dehydrogenation were both reduced. The hydrogenation (at 130 bar and 100 °C) occurs at about 10 minutes, whereas before it used to take circa 9 hours. Even more, the H_2 storage capacity remains at 4.5 wt. % after 25 cycles of hydrogenation and dehydrogenation. A complete re-hydrogenation after those cycles takes two hours though [22].

$Ti_{13} \cdot 6THF$ consist of colloidal zero-valence Ti particles that are surrounded by intact THF ligands. These thirteen Ti atoms form a regular cluster with six oxygen atoms (from the THF molecules) in an octahedral configuration, with a distance between the Ti atoms of about 2.83 Å. These small clusters are also known as Ti nanoclusters [36], [37].

The process of hydrogen release with $Ti_{13} \cdot 6THF$ is even less known than that of $TiCl_3$. By any mean, the reduction in size of the particles would in any case help to disperse the catalyst better, which at the same time seems to be responsible for the increase of the reaction rate [36], [37].

1.5 Prior NMR studies on the alanates – Objectives of the present investigations

The tool that we used for this work was NMR, as it is very powerful to characterize or solve the structures of the samples as well as to learn about the mobility of the resonant nuclei. According to the before mentioned possibilities, one can divide the NMR studies in two main groups. The first group “characterized” the samples, which mainly means that the spectra (usually the magic angle spinning (MAS) spectra) were measured. In Ref. [46], they characterized $LiAlH_4$ using different catalysts (Al_3Ti and Al_3Fe) with ^{27}Al -MAS NMR spectra. Later on the thermal decomposition of $LiAlH_4$ was characterized using static, MAS and multiple quantum MAS (MQMAS) ^{27}Al NMR in Ref. [47]. Mamatha *et al.* characterized, also by the MAS spectra on ^{27}Al and ^{23}Na materials like

magnesium, calcium and lithium-magnesium alanates [48]. For us it was important to know if we can **characterize with ^1H static spectra the samples of NaAlH_4 and Na_3AlH_6** . Within this group, it was tried to clarify possible changes in the structure due to e.g. the hydrogen desorption like in Ref. [52]. E. H. Majzoub *et al.* studied the lattice parameter measuring crushed single crystals which are exposed to Ti during its growth. They show that there is no solubility for Ti in NaAlH_4 [53]. Also, from the same group other NMR studies were done to clarify where exactly the catalyst is located using ^{27}Al -MAS and ^{27}Al MQMAS on a heavily doped (33.3 at.) sample [54]. In that last study the ^1H MAS NMR data indicated a possible coordination of the aluminum with oxygen atoms in the THF molecules. V. P. Tarasov and G. A. Kyrakosyan found differences in the quadrupolar coupling constants of ^{27}Al and ^{24}Na between NaAlH_4 and NaAlD_4 [55]. Finally in Ref. [51], M. H. W. Verkuijlen *et al* characterize, using ^1H , ^{23}Na and ^{27}Al solid state NMR, pure NaAlH_4 and $TiCl_3$ -doped NaAlH_4 by Hahn-solid-Hahn [56], [57] echo magic echo and magic sandwich echo[58]. Our interest was to know if there are **structural differences between NaAlH_4 with and without catalyst**.

In the second group, one is concerned with the mobility of the hydrogen. J. Senegas *et al.* [49] found that thermic activated motional narrowing of Na_3AlH_6 can be quantitatively explained by the rotation of the $[\text{AlH}_6]^-$ groups around its C_4 -symmetry axis. This was confirmed by us in Refs. [50] and [8]. Also, in Ref. [8] the exponential recoveries of two untreated samples (without catalyst and not ball-milled) were measured at room temperature. M. H. W. Verkuijlen *et al* found this process can be successfully described (besides a fast rotational motion around one single C_4 axis) by a slower rotation around the other thermally activated rotation jumps of AlH_6 cluster assuming a slower rotation around the other two C_4 axes. The activation barrier of the last process is given by $E_a = 25 \text{ kJ/mol}$, with an attempt frequency of $\nu_0 = 4 \times 10^{10} \text{ Hz}$ [51]. Important was for us to know **how the different mobilities were influenced as a function of temperature** (in the transition from NaAlH_4 to Na_3AlH_6) **for diverse milling times or catalyst proportions**. Therefore we measured systematically as a function of temperature the spectra and the inversion recovery of samples with different catalyst and milling times.

The theory necessary to follow the present work is presented in the next chapter.

2 NMR theory

In this section the NMR theory relevant for this work is presented.

2.1 Introduction

A nucleus with **spin angular** momentum different from zero has a **magnetic moment** which is proportional like:

$$\hat{\mu} = \gamma_n \hbar \hat{\mathbf{I}}, \quad (2.1)$$

where γ_n is called the gyromagnetic ratio, \hbar is the Planck's constant divided by 2π and finally $\hat{\mu}$ and $\hat{\mathbf{I}}$ are the magnetic moment and angular moment operators, respectively.

By applying a constant magnetic field \mathbf{B}_0 along the z -direction to a magnetic dipole $\hat{\mu}$, the dipole tries to align to the same direction (see Figure 2.2). Using the potential energy, we get the Hamiltonian describing the interaction with a constant magnetic field

$$\hat{\mathcal{H}}_Z = -\hat{\mu} \cdot \mathbf{B}_0 \quad (2.2)$$

$$= -\gamma_n \hbar \hat{\mathbf{I}} \cdot \mathbf{B}_0 = -(\gamma_n \hbar B_0) \hat{I}_z \quad (2.3)$$

$$= -\omega_0 \hbar \hat{I}_z, \quad (2.4)$$

where $\omega_0 = -\gamma_n B_0$ is known as the **Larmor Frequency** and \hat{I}_z has the eigenvalues: $I, I-1, \dots, 1-I$, or $-I$. In the classical representation, for example with protons ($I = \pm 1/2$), we have two different orientations with energies $E_\uparrow = \frac{1}{2}\hbar\nu$ and $E_\downarrow = -\frac{1}{2}\hbar\nu$. When the magnetic moment is aligned along the field, it will have a lower energy than when it is aligned in the opposite direction. The energy splitting between the possible levels is given by $\hbar\nu$ and it is called **Zeeman splitting**. \mathcal{H}_z in Equation (2.3) is the so-called Zeeman Hamiltonian.

Nuclear magnetic resonance (NMR) spectroscopy uses the effect of absorption of the radiofrequency radiation which is generated by applying to the nuclei a strong static magnetic field. Absorption of the radiation causes the nuclear spin to flip between different orientations. After absorbing energy the nuclei will re-emit the radiation and return to the lower-energy state. For a proton in a field of 1 Tesla, the rotation frequency would be 42.5 MHz.

2.2 NMR interactions

The time-dependent evolution of a spin system is governed by interactions, which can be separated in external and internal interactions.

External interactions are the magnetic fields used to manipulate the quantum states of the spins in order to get information about the internal interactions or to override certain interactions like spin coupling. Using the high-field approximation, one assumes that the spin system dynamics is dominated by the strong interaction with the external magnetic field. The manipulations of the quantum states consist on the application of one or several strong r.f.-pulses (see section 2.4).

In solid state NMR, the most elementary **internal interaction** is due to direct **dipole - dipole interaction** between nuclear spins. Other interactions of the nuclear spins are due to the interaction between electrons and the nucleus. These other interactions are known as *chemical shift*, *Knight shift*, *quadrupole interaction*, and *indirect spin-spin interactions*. Chemical shift and Knight shift cause a deviation of the nuclear Larmor frequency (see Equation (2.3)). However, when working with low resolution NMR (low resonance frequency and without using Magic Angle Spinning (MAS), as we do) it is usually not possible to differentiate the shifts in the spectra due to the overlapping of the different contributions. Since we are measuring proton NMR, the quadrupole interaction is absent because the quadrupole moment equals zero for protons. Therefore those interactions (interactions between the electrons and the nuclei) will not be discussed in this work.

The spin-spin interactions consist of secular and non-secular terms. The term “non-secular” in this context indicates that spin transitions are induced which do not conserve the Zeeman energy in the high-field limit. For spectroscopic purpose one can restrict oneself to the consideration of the secular parts, generating either no spin transitions or only transitions conserving the spin Zeeman energy [59]. The secular approximation is very useful in order to simplify the description of the dipolar interactions, and to follow the path of the magnetization after a given pulse sequence. Usually, only after the “path” is found, the non-secular terms are considered (See Section 2.8).

2.2.1 Dipolar interaction

The interaction between spins gives rise to the so-called homonuclear dipolar interaction, and the heteronuclear dipolar interactions. Homonuclear corresponds to spins of the same kind of nuclei and heteronuclear to spins of different nuclei.

The Hamiltonian due to the dipolar interaction between two spins j and k is represented by

$$\mathcal{H}_D = b_{jk} \left(3(\hat{\mathbf{I}}_j \cdot \mathbf{e}_{jk})(\hat{\mathbf{I}}_k \cdot \mathbf{e}_{jk}) - \hat{\mathbf{I}}_j \cdot \hat{\mathbf{I}}_k \right) \quad (2.5)$$

where \mathbf{e}_{jk} is the unit vector parallel to the line joining the centers of the two nuclei (see Figure 2.1). b_{jk} is the so-called **dipolar coupling constant** and its magnitude is given by:

$$b_{jk} = -\frac{\mu_0 \hbar}{4\pi} \frac{\gamma_j \gamma_k}{r_{jk}^3}, \quad (2.6)$$

where r_{jk} is the distance between both spins and μ_0 is, as usual, the permeability of free space.

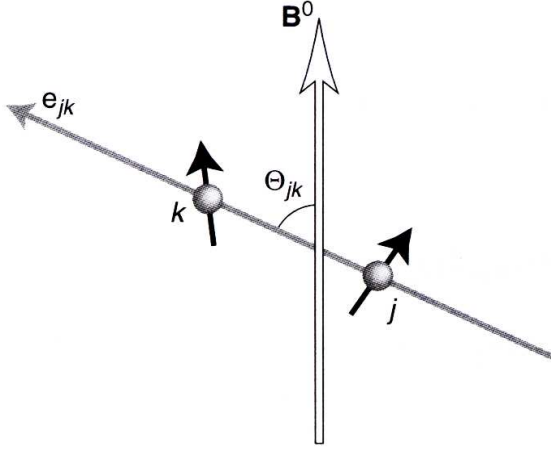


Figure 2.1: Interaction between two spins. Θ_{jk} is the angle formed by the vector joining the dipoles, e_{jk} , and the static magnetic field \mathbf{B}^0 [60].

The form of the secular dipole coupling depends on whether the spins \mathbf{I}_j and \mathbf{I}_k are of the same isotopic species or not. This is intuitively clear since the energy level differences between energy eigenstates depend directly on the type of nuclei.

Homonuclear dipolar interaction

If the spins are of the same type (homonuclear case) the secular dipolar Hamiltonian is given by

$$\hat{\mathcal{H}}_{II}(\Theta_{jk}) = d_{jk}(3\hat{I}_{jz}\hat{I}_{kz} - \hat{\mathbf{I}}_j \cdot \hat{\mathbf{I}}_k), \quad (2.7)$$

where d_{jk} is the **secular dipolar coupling** given by

$$d_{jk} = b_{jk} \frac{1}{2}(3\cos^2 \Theta_{jk} - 1). \quad (2.8)$$

Note that, contrary to the dipolar coupling constant (Equation (2.6)), the secular dipolar coupling depends on the orientation of the spin pair with respect to the magnetic field. Θ_{jk} is the angle between the vector joining the spins and the external magnetic field, i.e., $\cos \Theta_{jk} = \mathbf{e}_{jk} \cdot \mathbf{e}_z$ (see Figure 2.1).

Heteronuclear dipolar interaction

For heteronuclear interaction, the secular part of the direct dipolar Hamiltonian is given by:

$$\hat{\mathcal{H}}_{IS}(\Theta_{jk}) = d_{jk} 2\hat{I}_{jz}\hat{I}_{kz}, \quad (2.9)$$

where d_{jk} is given also by the Equation (2.8).

2.3 Equation of motion - Classical treatment

2.3.1 Single spin

A constant magnetic field \mathbf{B}_0 applied to a magnetic dipole ($\hat{\mu}$) will cause a torque \mathbf{D} . The magnetic dipole will describe a circular precession around the z -axis with a constant angular velocity and its Hamiltonian is given by the Equation (2.3) (see Figure 2.2).

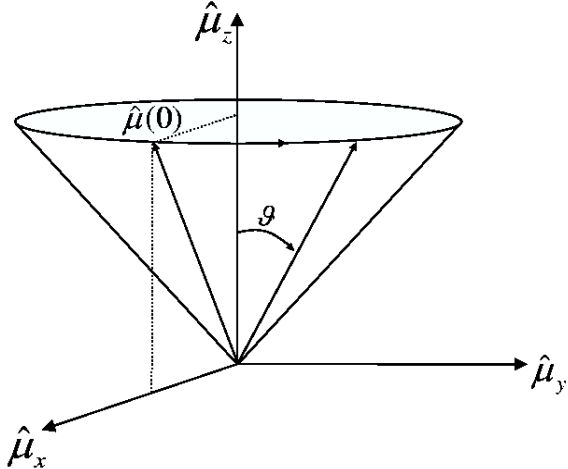


Figure 2.2: Motion of a magnetic dipole under a constant \mathbf{B}_0 field along z -axis.

The motion is described by the change of the angular momentum with time $\mathbf{D} = (d\hat{\mathbf{I}}/dt) = (1/(\hbar\gamma_n))(d\hat{\mu}/dt)$. In this case, the torque acting on a spin is also given by $\mathbf{D} = \hat{\mu} \times \mathbf{B}$. Thus the equation of motion is then given, in terms of the magnetic dipole, as:

$$\frac{d\hat{\mu}}{dt} = \gamma_n \hbar \hat{\mu} \times \mathbf{B} = \gamma_n \hbar \begin{bmatrix} \hat{\mu}_y B_z - \hat{\mu}_z B_y \\ \hat{\mu}_z B_x - \hat{\mu}_x B_z \\ \hat{\mu}_x B_y - \hat{\mu}_y B_x \end{bmatrix} \quad (2.10)$$

If a static magnetic field is applied along z -axis, i.e., for $\mathbf{B} = B_0 \mathbf{z}$, the Equation (2.10) can be simplified as:

$$\frac{d\hat{\mu}}{dt} = \gamma_n \hbar B_0 \begin{bmatrix} \hat{\mu}_y \\ -\hat{\mu}_x \\ 0 \end{bmatrix} \quad (2.11)$$

The z -component of the magnetic momentum is parallel to the field and it is constant during the motion, i.e., $\hat{\mu}_z(t) = \hat{\mu}_z(0)$.

Combining the equations of x - and y - component, we get

$$\frac{d^2}{dt^2} \hat{\mu}_x = -(\gamma_n B_0)^2 \hat{\mu}_x = \omega_0^2 \hat{\mu}_x.$$

Without loosing generality we suppose that $\hat{\mu}(0) = \mu_a (\mathbf{x} \sin \vartheta + \mathbf{z} \cos \vartheta)$ (see Figure 2.2). Hence, the solution of the differential equation of the x -component is given by $\hat{\mu}_x(t) = \mu_a \sin \vartheta \cos(\omega_0 t)$.

Substituting the already obtained $\hat{\mu}_x$ (in the last sentence) in the y -component of the Equation (2.11), we obtain that $\hat{\mu}_y(t) = \mu_a \sin \vartheta \sin(\omega_0 t)$.

Hence, the **motion of the magnetic moment** is given by

$$\hat{\mu}(t) = \mu_a \begin{bmatrix} \sin \vartheta \cos(\omega_0 t) \\ \sin \vartheta \sin(\omega_0 t) \\ \cos \vartheta \end{bmatrix} \quad (2.12)$$

The magnetic moment will precess around the direction of the magnetic field rather than settle down in the direction of the magnetic field.

2.3.2 Rotating frame

We can now introduce a new reference system rotating around z with a frequency, ω_{rf} (see **Figure 2.3**). Such a reference system is called **rotating reference system**. In that case, we have $d\hat{\mu} = d\hat{\mu}' - \vec{\omega}_{rf} dt$.

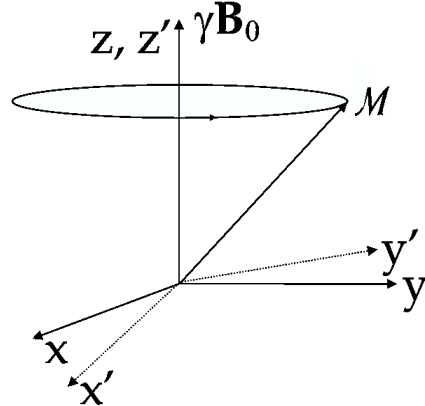


Figure 2.3: Rotating reference frame

Rewriting the equation (2.10) in terms of the magnetization in the rotating frame, we get:

$$\frac{d\hat{\mu}'}{dt} = (\gamma_n \hbar \mathbf{B}_0 - \vec{\omega}_{rf}) \times \hat{\mu}' \quad (2.13)$$

$$= \Delta \vec{\omega} \times \hat{\mu}' \quad (2.14)$$

$$= \gamma_n \mathbf{B}_{eff} \times \hat{\mu}', \quad (2.15)$$

where

$$\Delta \vec{\omega} = \gamma_n \mathbf{B}_0 - \vec{\omega}_{rf}, \quad (2.16)$$

and

$$\mathbf{B}_{eff} = \mathbf{B}_0 - \vec{\omega}_{rf}/\gamma_n. \quad (2.17)$$

When the rotating frame turns with the same angular velocity as $\hat{\mu}$, $\hat{\mu}'$ does not evolve, i.e.,

$$\frac{d\hat{\mu}'}{dt} = 0.$$

In this case, $\hat{\mu}'$ is constant and it is usually said that we are in **resonance**. This reference frame is specially useful to visualize the change in direction of the magnetization due to the application of pulses perpendicular to the stationary field \mathbf{B}_0 .

2.3.3 Ensemble of spins

For an ensemble of spins one is interested then in the expectation value of the magnetic dipolar moment. The expectation value of a given operator is the average over the ensemble of spins.

Macroscopically, **magnetization** is what one is able to detect. It is given by

$$\mathcal{M} = n \langle \hat{\mu} \rangle, \quad (2.18)$$

where n is the density of magnetic moments.

The **density operator** contains or implies the whole information of an ensemble of spins systems, but also it is the only operator accessible by measurements. It is therefore the quantity which is – explicitly or implicitly – employed [59]. In most of the cases the derived equations of motion for each spin can be applied to the ensemble of spins, represented by its expectation value \mathcal{M} not $n \langle \hat{\mu} \rangle$.

2.4 Pulse NMR

An **induced transition** will be macroscopically induced only near the so-called **resonance frequency**, which corresponds to the same frequency at which the magnetic dipoles are rotating due to the static field. Therefore one applies an extra magnetic field $\mathbf{B}_1(t)$ or pulse in resonance, which should be strong, time dependent and perpendicular to the static magnetic field (z -axis).

A pulse then will basically deflect the magnetization of the sample by a given angle ϕ . However, by combining them, one can e.g. suppress or refocus a specific part of the NMR signal. Nowadays there are probably hundreds of combinations of pulses which achieve very different results. Thanks to the pulse sequences, NMR has converted into a very powerful tool for investigation of not only diffusion, but also in structure determination of e.g. biological systems.

The precession of a spin due to e.g. the static magnetic field, or as the application of a pulse, can be expressed in a very elegant way (very general and simple) using the so-called spin system propagator, $\mathcal{P}_i(\beta)$. The propagators are derived from the rotation operators: $\hat{\mathcal{R}}_k(\beta) = \exp(-i\beta \hat{I}_k)$, where $k = x, y$, or z .

Precession of a spin due to a static magnetic field

The precession of a spin-system due to a static magnetic field, $B_0\hat{\mathbf{z}}$ can be characterized by a time-dependent angle β in the xy -plane. In the rotating frame in a period of time t at an angular velocity $\Delta\omega$, the spin-system precesses by an angle $\beta = \Delta\omega t$. In that case, the propagator of the system is given by:

$$\begin{aligned}\hat{\mathcal{P}}(\beta) &= \exp(i\beta\hat{I}_z) \\ &= \exp(i(\Delta\omega t)\hat{I}_z) \\ &= \exp(-(i/\hbar)\hat{\mathcal{H}}t),\end{aligned}$$

where $\Delta\omega$ is given as in Equation (2.16) as $\Delta\omega = \omega_0 - \omega_{rf}$. This value represents the frequency offset or detuning of the irradiation with respect to the resonance frequency ω_0 .

Therewith the precession is represented by:

$$\mathcal{M}(t) = \exp(-(i/\hbar)\hat{\mathcal{H}}t)\mathcal{M}(0)\exp((i/\hbar)\hat{\mathcal{H}}t) \quad (2.19)$$

It is intuitively clear that this last equation will be valid for any given Hamiltonian, during the evolution or during a pulse.

Pulse propagator

The rotating reference frame is especially useful to visualize the change in direction of the magnetization due to the application of the so-called “r.f. pulses”. As in resonance, $\Delta\tilde{\omega} = 0$, when a pulse is applied e.g. in the x -axis (see Figure 2.4), $\mathbf{B}_{eff} = B_1\hat{\mathbf{x}}$. The magnetization will be deflected according to Equation (2.15) to the y -axis. If there are inhomogeneities of the field (regardless of their provenance), $\Delta\omega$ is not exactly zero. However, a pulse is assumed to have an amplitude B_1 much larger than any given offset field and a duration shorter than $1/\Delta\omega$. Therefore the inhomogeneities can be neglected during the pulses [59].

Depending on how much time the extra magnetic field \mathbf{B}_1 is “turned on”, the magnetization will be deflected by a certain ϕ -angle. In similar way as in Sec. 2.4, the way in which the magnetization changes its direction (due to a given pulse) would be given by the total Hamiltonian of the system.

On resonance, when $\Delta\omega = 0$, the Hamiltonian of a pulse applied on the x -axis is reduced to

$$\hat{\mathcal{H}} = -\omega_1\hbar\hat{I}_x. \quad (2.20)$$

The operator of ϕ -pulse is therefore

$$\mathcal{P}(\phi) = \exp(-(i/\hbar)\hat{\mathcal{H}}t) = \exp(i\omega_1 t \hat{I}_x) \quad (2.21)$$

$$= \exp(i\phi\hat{I}_x), \quad (2.22)$$

where

$$\phi = \omega_1 t. \quad (2.23)$$

Hence, when a pulse ϕ is applied on resonance on the x -axis, the state of the spin is given by

$$\mathcal{M}(t_p) = \exp\left(i\phi\hat{I}_x\right)\mathcal{M}(0)\exp\left(-i\phi\hat{I}_x\right) \quad (2.24)$$

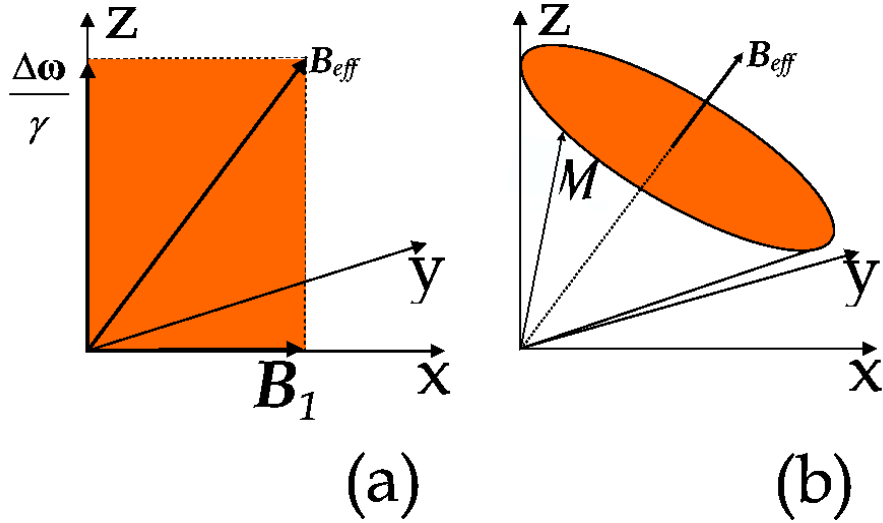


Figure 2.4: (a) Effective magnetic field B_{eff}

(b) Motion of the moment \mathcal{M} in the rotating frame

2.4.1 Single pulse

In the rotating reference frame (when $\Delta\omega = 0$), assuming that $\mathcal{M}(0) = \mathcal{M}_z$, we obtain that the magnetization will be deflected by an angle ϕ about \hat{I}_x as¹

$$\mathcal{M}'(t_p) = \mathcal{M}'_y \sin \phi + \mathcal{M}'_z \cos \phi. \quad (2.27)$$

¹For operators which cyclically commute, for example the angular momentum, $[\hat{I}_x, \hat{I}_y] = i\hat{I}_z$, a rotation of a vector can be expressed as, e.g.,

$$\exp(-i\vartheta\hat{I}_z)\hat{x}\exp(-i\vartheta\hat{I}_z) = \hat{x} \cos \vartheta + \hat{y} \sin \beta \quad (2.25)$$

$$\hat{R}_z(\vartheta)\hat{x}\hat{R}_z(-\vartheta) = \quad (2.26)$$

This is usually called **Sandwich rule** [60].

On the other hand, $\exp(-i\beta\hat{I}_i)\hat{i}\exp(i\beta\hat{I}_i)$ is nothing but a rotation of a vector around itself. Therefore

$$\hat{R}_i(\vartheta)\hat{i}\hat{R}_i(-\vartheta) = \exp(-i\vartheta\hat{I}_i)\hat{i}\exp(i\vartheta\hat{I}_i) = \hat{i}.$$

A very nice table to this transformations can be found in Ref. [59] on page 442.

Free precession after a $\frac{\pi}{2}$ -pulse

Thus, according with Equation (2.27), \mathcal{M} will be deflected, when $\phi = \frac{\pi}{2}$ as

$$\mathcal{M}'(t_{\frac{\pi}{2}}) = \mathcal{M}'_y, \quad (2.28)$$

The magnetization thus will be completely turned to the y' -axis. After the pulse, \mathcal{M}' will try to come back to its initial or equilibrium position. Graphically, the movement of the spins during a pulse will follow a circle in the $x'y'$ - plane. The movement in the laboratory would look like the spiral shown in Figure 2.5 (b). As this solution undamped, the movement of the magnetization after a pulse would last in principle “forever”. In reality, as soon as the magnetic field \mathbf{B}_1 is turned off (at $t = t_p = \frac{\pi/2}{\omega_1}$), the spin system undergoes a free precession, trying to get to the equilibrium. This precession will induce a magnetization, which is what we measure (see Section 3.1). This signal is called Free Induction Decay – FID. Later on we will take into account the relaxation processes (see section 2.8).

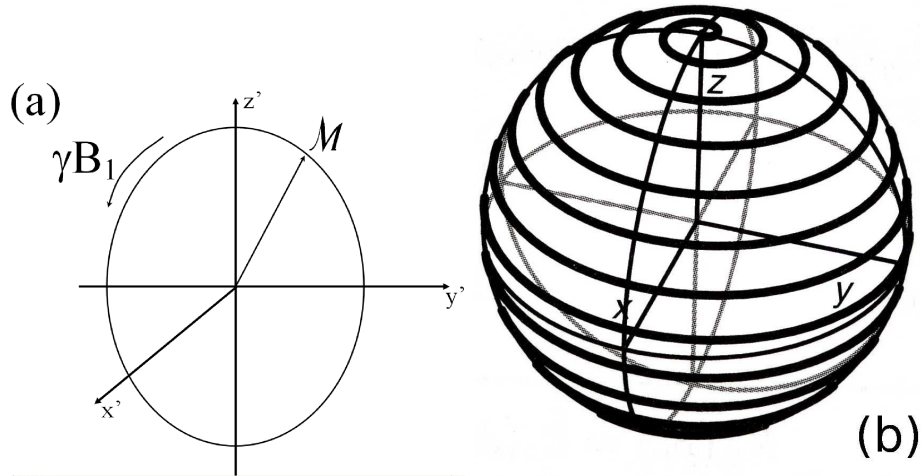


Figure 2.5: (a) Trajectory from by \mathcal{M} of the system in the rotating frame (b) Trajectory of \mathcal{M} seen from in the laboratory frame

2.5 Hahn echo

Lines in solid-state NMR spectra are often quite broad, and their corresponding FID is so short that for technical reasons, it is not possible to detect the complete FID signal. This is because immediately after a high power r.f. pulse, we have a measurement dead time. If the FID signal decays significantly during this dead time, if e.g. its amplitude decreased too much, sometimes is not even possible to compute the correct spectrum from the remaining signal by Fourier transformation². In such a situation, the FT-NMR spectra obtained with a $\pi/2$ -pulse can be very different as the original one (without dead time).

²In particular, measuring with the 67.7 MHz Spectrometer, the smallest dead time was equal to $6 \mu s$. Therewith at least one fifth of the signal has already decayed when our experimental restrictions enable us to measure

Therefore one usually applies the very useful “Hahn echo” [61]. This echo is the most famous of all possible echoes, maybe because of its simplicity. The cover page of the magazine Physics Today from 1953 shows a nice scheme of it (see **Figure 2.6**). In the picture, the evolution of the spin

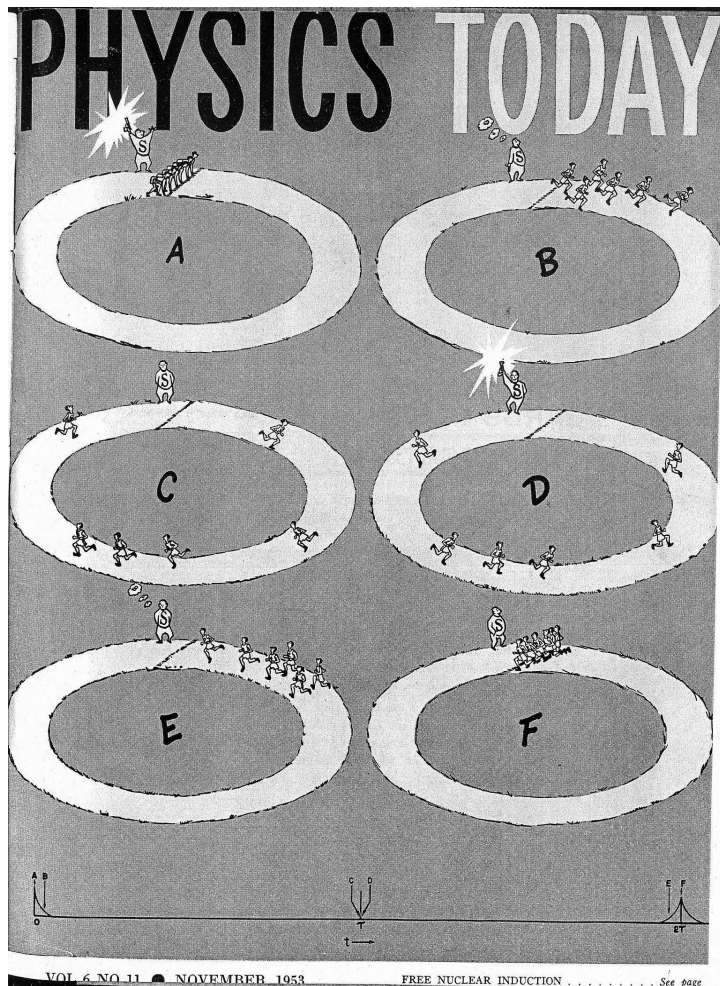


Figure 2.6: Scheme of the Hahn echo. Portrait of the magazine Physics Today [61].

system is represented as a race. The spins are represented by the runners and the shots would represent our pulses. The race begins with a shot. Almost immediately it is clear that some of the spins are faster than the others. After a while, in the scheme C, the runners are completely dephased. Suddenly in the scheme D, the judge shots again. The runners have to run now in the "opposite direction". As the runners maintain always their velocity, after a time 2τ , the runners arrive to the end in a kind of strange race where everybody wins! In real life that would be also quite boring, wouldn't it?

The reason why some runners are faster than others for 1H -NMR is mainly the heteronuclear interaction (the interaction with the spins which are not irradiated) and the inhomogeneities of the experimental set up.

The rephasing of the runners (spins) in the scheme E, as well as the expected rephasing after scheme F induces a signal (current), which is in fact what we measure. This signal is called “echo”

(see signal around $t = 2\tau$ in Fig.2.7). Comparing the schemes A and F in Figures 2.6 and 2.7, it should be nevertheless clear that the free induction decay (FID) and the **second half of the echo** are equivalent. Thus, in general to bridge the experimental dead times and measure the complete NMR signals, we use the second half of the echoes.

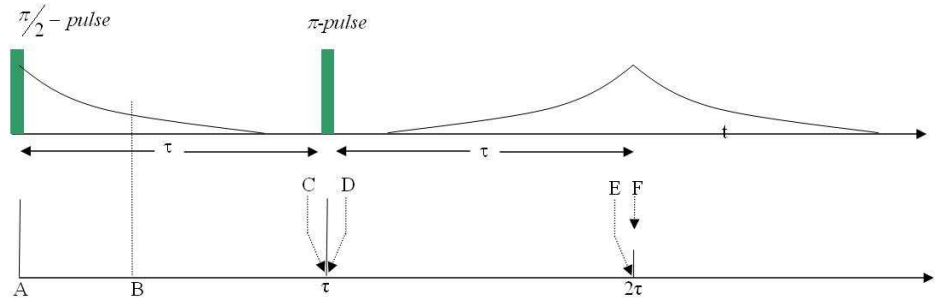


Figure 2.7: Hahn echo pulse sequence

Time reverse phenomena

Looking at the time scale shown in the bottom of the diagram in Figure 2.7, we can see that t_C is in the limit equal to t_D , i.e., $t_C = t_D$. The direction of the runners is determined by the direction of the magnetic field (see section 2.3.1). For technical reasons it is not possible to change the direction of the magnetic field. Therefore, at t_D the phase of the magnetic moments is changed by applying a π -pulse. Applying a pulse propagator to the heteronuclear Hamiltonian, $\hat{\mathcal{H}}_{IS}$, of the system, we have that

$$\hat{\mathcal{P}}_y(\pi)\hat{\mathcal{H}}_{IS}\hat{\mathcal{P}}_y^{-1}(\pi) = \exp(-i\pi\hat{I}_y)\hat{\mathcal{H}}_{IS}\exp(i\pi\hat{I}_y) = -\hat{\mathcal{H}}_{IS}. \quad (2.29)$$

After this pulse (at $t = \tau$) the spin system propagator $\exp[-(i/\hbar)(-\hat{\mathcal{H}}_{IS}) * \tau]$ would be the same as the initial propagator but at $t = -\tau$, i.e., $\exp[-(i/\hbar)\hat{\mathcal{H}}_{IS} * (-\tau)]$. That is why this kind of “phenomena” is called **time reversal phenomenon** and is the key for all kinds of echoes used in NMR.

The signal of the spin system may not be completely refocused with a Hahn Echo for strong dipolar interactions. That is because it was intrinsically supposed, that there is no interaction between any of the spins. Using again the analogy of the runners, if for example some of the runners shake their hands from time to time during the race (strong dipolar couplings), it would not be possible to refocus the whole signal.

2.6 Magic echo

Analogous to the Hahn echo, with the magic echo (ME) pulse sequences long dead times can be overcome. However, contrary to the Hahn echo, ME pulse sequences work also at systems with strong **homonuclear dipolar interactions**.

ME was first proposed by W. R. Rhim and H. Kessemeier [62], [63]. There are several versions of this pulse (see e.g. [64], [65]), however, this pulse sequence was not used so often until a simplification was achieved by K. Takegoshi and C. A. McDowell [66]. The simplification of the “ME propagator” consists of a long pulse along x followed by a pulse along \bar{x} (pulse in the opposite direction). The experiments are in this way easier to be obtained because possible differences in the critical frequency will be canceled after the pulse in the opposite direction is applied. The variation of the ME that we used, is presented schematically in the Figure 2.8. The magic echo sequence presented here consists of a $(\pi/2)_x$ -pulse plus a so-called magic sandwich: $[(\pi/2)_y - (\alpha)_x - (\alpha)_{-x} - (\pi/2)_{-y}]$.

To understand the ME one should know, what within the long pulses of the magic sandwich happen. Within so long pulses, the secular dipolar Hamiltonian has to be again averaged (see the explanation in Section 2.2). The treatment of the averaging is simplified, when it is done in a reference frame called **Tilted Rotating (TR) frame** [59]. This reference system rotates, as within the rotating frame (See Sec. 2.3.2), but also its z -axis is parallel to the effective magnetic field, \mathbf{B}_e . Assuming the pulses are on resonance, $\mathbf{B}_e = \mathbf{B}_1$, where \mathbf{B}_1 is the field given by the pulses (See upper part of the Figure 2.8).

In the tilted rotating frame system, the secular part of the **dipolar Hamiltonian**, \mathcal{H}_D , is transformed to

$$\mathcal{H}_{TR} = \frac{1}{2}(3 \cos^2 \Theta - 1)\mathcal{H}_{II} + \cos \Theta \mathcal{H}_{IS}, \quad (2.30)$$

where Θ is the polar angle of the effective field in the rotating frame. In the ideal case, during a resonant pulse, the tilt angle is $\Theta = \pm\pi/2$ and

$$\mathcal{H}_{TR} = -\frac{1}{2}\mathcal{H}_{II}. \quad (2.31)$$

A graphic representation of this equation is shown in the bottom of Figure 2.8. Due to the $-1/2$ factor of the Equation (2.31), we can say that the ME counteracts the dipolar interactions within the sample, when the evolution intervals with and without the RF irradiation are matching in a ratio of 2 : 1. For a time outside the magic sandwich of 2τ , we need a sandwich with a length of 4τ (see Figure 2.8)³. In that way, the echo would be found experimentally at

$$t = 2\tau + 4\tau \quad (2.32)$$

In analogy with Hahn-Echo, the Hamiltonian of the system is negative and the propagator of the system suffers a **time reversal phenomenon** (see Section 2.5). Therefore, we are able to obtain the echo of the homonuclear interactions. For the whole sequence, for a $\Theta = \pi/2$, the propagator

³Thus the time between the magic sandwich and the initial or final pulse do not necessary need to be equal. However, we use the same lengths as we later on also used the Magic-Hahn Echo (which do need equal times)

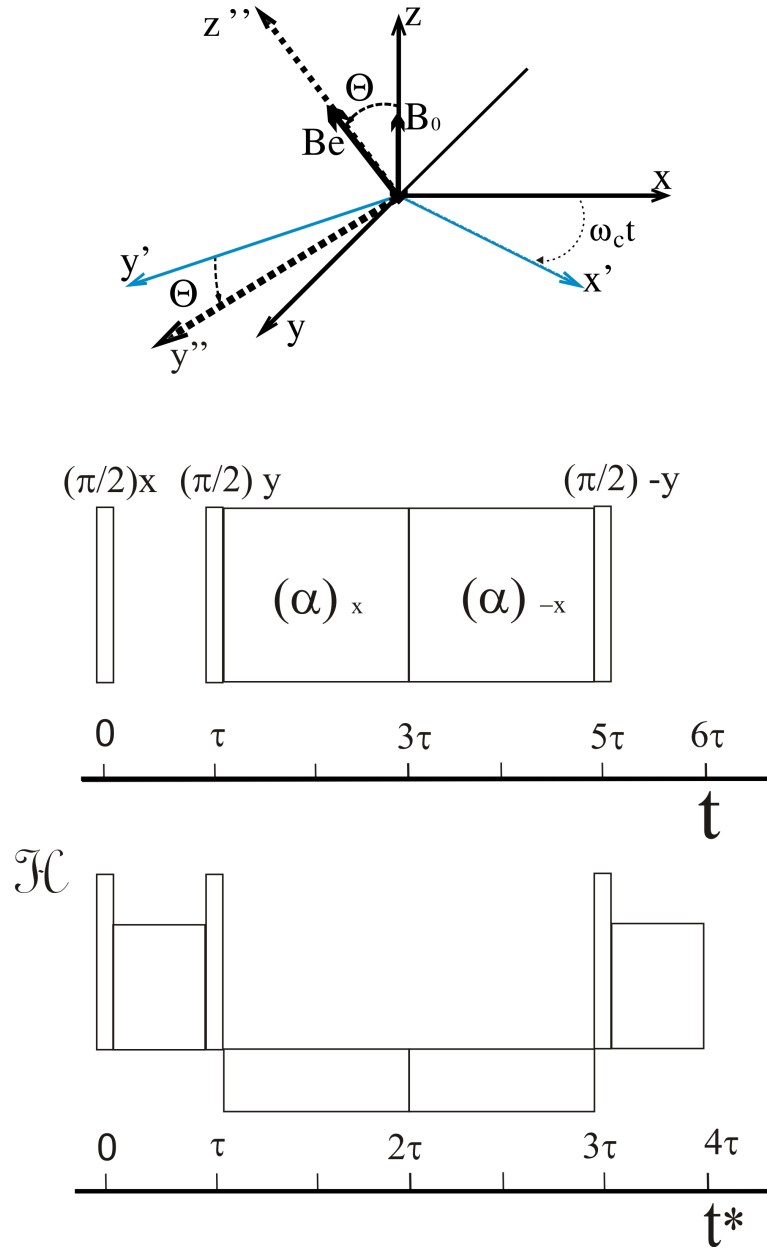


Figure 2.8: (a) Laboratory (—), rotating (---) and tilted Rotating Frame (...), (b) ME pulse sequence, (c) Schematic representation of the homonuclear Hamiltonian acting during the pulse sequence

of the pulse sequence is given as:

$$\begin{aligned}
 \mathcal{P}(6\tau) &= \exp[-i(\mathcal{H}_D\tau + \mathcal{H}_{II,TR}4\tau + \mathcal{H}_D\tau)] \\
 &= \exp[-i(\mathcal{H}_D\tau - \frac{1}{2}\mathcal{H}_{II}4\tau + \mathcal{H}_D\tau)] \\
 &= \exp[-i((\mathcal{H}_{II}\tau + \mathcal{H}_{IS}\tau) - \mathcal{H}_{II}2\tau + (\mathcal{H}_{II}\tau + \mathcal{H}_{IS}\tau))] \\
 &= \exp[-i(2\mathcal{H}_{IS}\tau)].
 \end{aligned}$$

Therefore, the magic sandwich refocuses the whole homonuclear interaction and the evolution time evolution time, is

$$t^* = 2\tau. \quad (2.33)$$

Heteronuclear dipolar interactions

Only the resonant nuclei (the protons in this case) are excited during a r. f. pulse. There thus is no direct analogy in the case of heteronuclear interactions, as only the protons are on resonance. Therefore the dipolar interaction does not follow Equation (2.31). In order to be able to transform the Hamiltonian in an analogous way, it would be necessary to irradiate the other nuclei too (double resonance experiments). However, in that case one would have to deal also with the interactions between the electrons and the nuclei, like chemical shift, Knight shift, quadrupole interactions, and indirect spin-spin interactions.

2.7 Magic-Hahn echo

The form of the Magic-Hahn echo pulse sequence is very similar to the “normal” ME. In this case the last pulse is now $(\frac{\pi}{2})_y$, i.e., it has a positive phase. This pulse together with the change in Reference frame (between the TR- and the rotating-frame) match a π -pulse⁴. As we know, within the long pulse the homonuclear dipole interactions will be counteracted, and refocused after τ . The heteronuclear interactions on the other hand, act as the stationary inhomogeneities, which are averaged to zero during the pulses. Thus, the last pulse (as it equals a π -pulse) will refocus the dephasing in the same way as in a normal Hahn echo.

2.8 Relaxation (Bloch equation)

If the thermal equilibrium of a spin-system is disturbed, e.g. by applying an r.f. pulse, the magnetization usually approaches exponentially its equilibrium state. The so-called exponential longitudinal recovery occurs along the z -axis which is parallel to the applied stationary magnetic field \mathbf{B}_0 . The transversal decay also called spin-spin relaxation takes place in the xy -plane and it is characterized by a time constant called T_2 . Whereas the relaxation in the z - axis is characterized by time constant T_1 , which is known as the longitudinal or spin-lattice relaxation.

The decay of the signal is represented by linear differential equation with T_1 and T_2 decaying constants. Therefrom the **Bloch equation** develops from the Equation (2.10) to

$$\frac{d\mathcal{M}}{dt} = \gamma \mathcal{M} \times \mathbf{B} - \begin{bmatrix} \mathcal{M}_x/T_2 \\ \mathcal{M}_y/T_2 \\ (\mathcal{M}_z - \mathcal{M}_z(\infty))/T_1 \end{bmatrix}. \quad (2.34)$$

⁴Following the pulse propagation during the whole sequence (Sec.2.4, using Eq.(2.31)), one can see that this pulse together with the change of reference frame (from the tilted rotating frame to the rotating one) act as a $(\pi)_y$ pulse.

2.8.1 Spin - lattice relaxation

The characteristic time to reach the thermal equilibrium after a pulse is given by the longitudinal or spin-lattice relaxation time. The corresponding relaxation processes require an energy exchange between the spin-system and the lattice. This decay is characterized by the spin-lattice relaxation constant usually denoted as T_1 [67].

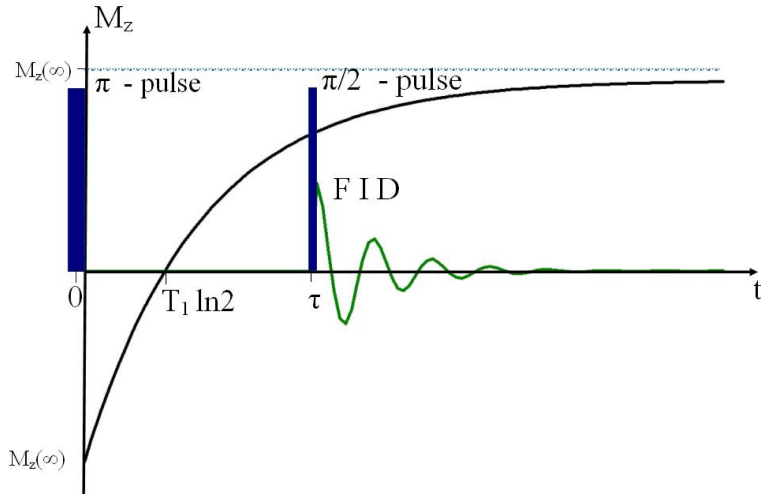


Figure 2.9: Inversion - recovery pulse sequence, the curve represents \mathcal{M}

Experimentally it is measured by the **inversion-recovery pulse sequence** (See Figure 2.9). This pulse sequence consists of a π -pulse followed by a $\pi/2$ -pulse. The first pulse inverts \mathcal{M} . In the time between the pulses, the system evolves towards equilibrium. The second pulse is applied to detect the state of \mathcal{M} . The same measurement is repeated several times with increasing time between the pulses, τ . As the magnetization is proportional to the area under the spectrum, we will get a negative magnetization for a very short time between the pulses ($\tau/T_1 \ll 1$) (See in Figure 2.10 – “1st. measurement”). The magnetization will increase for longer τ ’s until \mathcal{M} comes to the equilibrium (see in Figure 2.10 – “Last measurement”). For materials with a T_1 time that is too long to be measured within a reasonable time, we used the saturation-recovery pulse sequence. This sequence follows exactly the same principle but in this sequence, the magnetization is saturated by applying multiple $\pi/2$ r.f. pulses at relatively short repetition times. After the saturation, the magnitude of M_z tend to zero. Contrary to the inversion recovery, one does not have to wait until the sample is in equilibrium. Therefore, for T_1 values longer than 1 minutes, the measuring time is at least reduced by a factor of four.

The fitting of the recovery of the magnetization to its equilibrium value, $M_z(\infty)$, is given by

$$\mathcal{M}_z(\tau) = \mathcal{M}_z(\infty)(1 - \alpha \exp(-\tau/T_1)), \quad (2.35)$$

where $\alpha = 1$ for a saturation recovery measurement and $\alpha = 2$ for an inversion recovery measurement.

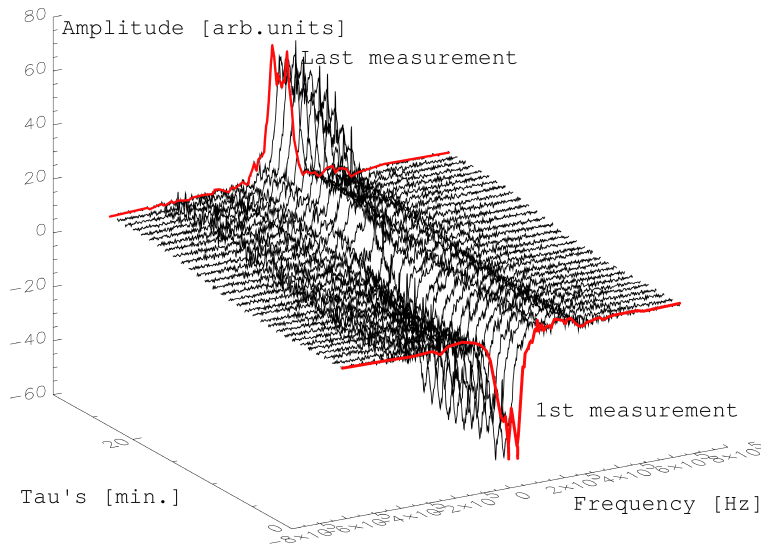


Figure 2.10: Fourier transform of the different FIDs, each measured after different waiting times, τ , between the r. f. pulses

2.8.2 Spin - spin relaxation

The relaxation mechanisms in the xy -plane do not necessarily require energy exchange with the surroundings. This decay is due to the **interactions between spins in the same ensemble (spin-spin relaxation)**. The spin-spin interaction causes losses of the phase coherence between the spins. Since the spin-lattice relaxation also causes loss of the phase coherence, the spin-spin relaxation time, T_2 , is usually shorter than the spin-lattice relaxation, T_1 [68]

The transverse magnetization is in fact what we measure after e.g. a simple $\pi/2$ -pulse. For an ideal magnet with a sample without strong dipolar couplings or mobile atoms like for example in liquids, it would be enough to fit the decay of the FID in order to get \mathcal{M} . However, the decay of the FID tends to be shorter as the inhomogeneities of the magnet or the interaction e.g. of heteronuclear spins dephase also the signal. As already mentioned in Section 2.5, this extra dephasing can usually be overcome by applying a Hahn Echo.

Therefore the “homogeneous” T_2 (depending only on the spin-spin interaction) can be directly measured with the application of pulse sequences like e.g. Hahn Echo (see Section 2.5).

Taking now the transverse relaxation into account, the magnetization will decay exponentially with T_2 . Hence combining Equation (2.12) with the relaxation we get

$$\begin{aligned}\mathcal{M}_x &= \mathcal{M}_0 \sin \vartheta \cos(\Delta\omega t) e^{-t/T_2} \\ \mathcal{M}_y &= \mathcal{M}_0 \sin \vartheta \sin(\Delta\omega t) e^{-t/T_2}\end{aligned}$$

2.9 NMR spectra

The response of the system in the xy plane, after any pulse sequence is determined at first approximation by the dipolar interaction (without taking into account the electron-nucleus interactions like chemical shift, Knight shift, quadrupole interaction, and indirect spin-spin interactions). The FID is that response in the xy -plane, and it is also called **transient response**, $G_j(t)$. The NMR spectra are obtained experimentally by the Fourier transform of the FID. In Figure 2.11 (a), we show the trajectory of the precession after a $\pi/2$ -pulse in the space. To obtain the NMR spectrum, the projection of the precession in the x - and y -axis can be Fourier transformed – taking the x -component as the real part and the y -component as the imaginary part (see Figure 2.11 (b)).

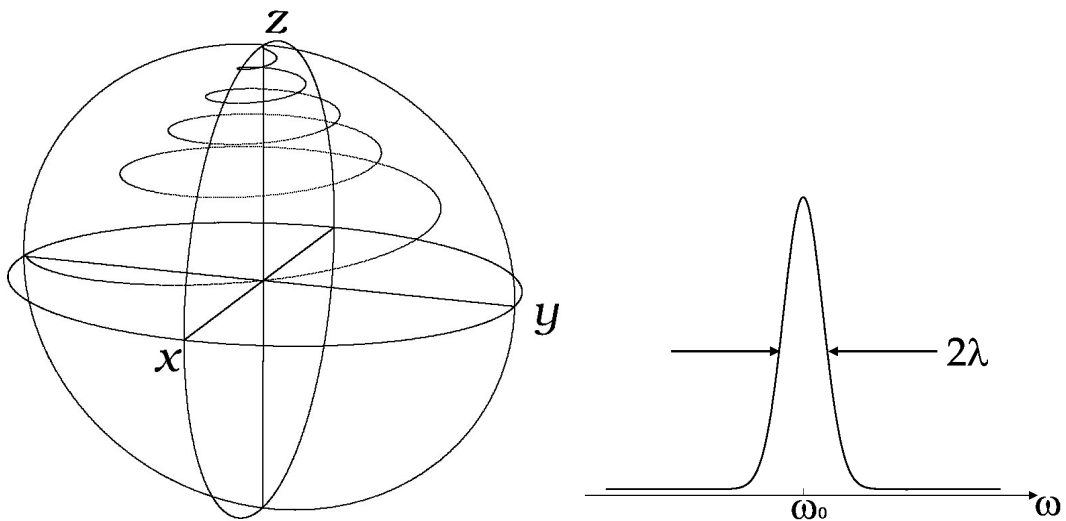


Figure 2.11: (a) Precession of \mathcal{M}

(b) NMR Spectrum with $\Delta\omega = 2\lambda$

There are already programs available (SIMPSON [69], [70], [71], [72] or Sensei, which simulate the spectra. In the input of the simulation one has to specify the atoms used, the value of the dipolar coupling constant, the Euler angle of the atoms which their line junction is e_{jk} with respect to a given reference system, the atom or atoms in which we want to detect and the used pulsed sequence. Initially it was planned to present simulations in the present work. However, it was not possible to get a real approximation to the experimental spectra because these programs are conceived for small, independent clusters of atoms. This means, cyclic conditions are not taken into account within the simulations (as expected in the crystals). Therefore, the cluster needed to generate the spectra should be very big, which is for technical reasons no possible.

2.9.1 Momenta expansion

It is in general very complex to calculate the function of the NMR spectra – $F(\omega)$ – for a given sample. Therefore one has usually to resort to approximations. Van Vleck [73] was the first to point out that a moment expansion can be performed rigorously due to the symmetry of the interaction Hamiltonian. The FID response function $G_x(t)$ can be then given by the expression [74], [75]:

$$G_x(t) = \sum_{n=0}^{\infty} \frac{(-1)^n}{(2n)!} M_{2n} t^{2n}, \quad (2.36)$$

where

$$M_{2n} \equiv \int_{-\infty}^{\infty} (\omega - \omega_0)^{2n} F(\omega) d\omega. \quad (2.37)$$

The second moment depends inversely on the distance between the interacting atoms to the sixth power [73], [74]. In international unit system the $M_{2,RL}$ (rigid lattice second moment) is given by⁵

$$M_{2,RL} = M_{2,II-RL} + M_{2,IS-RL} \quad (2.38)$$

$$= \frac{3}{4} \left(\frac{\mu_0}{4\pi} \right)^2 \gamma_I^4 \hbar^2 I(I+1) \sum_{i,j} (1 - 3 \cos^2 \theta_{ij})^2 r_{ij}^{-6} + \quad (2.39)$$

$$\frac{1}{3} \left(\frac{\mu_0}{4\pi} \right)^2 \gamma_I^2 \hbar^2 \sum_{i,k} \gamma_S^2 S(S+1) (1 - 3 \cos^2 \theta_{ik})^2 r_{ik}^{-6}, \quad (2.40)$$

where r_{ij} or r_{ik} is the distance between a given nuclei i and j or between the nuclei i and k . Also, γ_I is the gyromagnetic ratio of the proton spin with $I = 1/2$ and γ_S is the gyromagnetic ratio of the other spin S (the spins of atoms different from 1H , j) and θ_{ik} is the angle of the vector r_{ik} with the applied magnetic field B_0 .

As in a powder sample all possible orientations of θ are equiprobable, we have that

$$< (1 - 3 \cos^2 \theta)^2 > = 4/5 \quad (2.41)$$

and the second moment can be obtained for **an atom i** as

$$M_2 = M_{2,II} + M_{2,IS} \quad (2.42)$$

$$= \frac{3}{5} \left(\frac{\mu_0}{4\pi} \right)^2 \gamma_I^4 \hbar^2 I(I+1) \sum_j \frac{1}{r_{ij}^6} + \frac{4}{15} \left(\frac{\mu_0}{4\pi} \right)^2 \gamma_I^2 \gamma_S^2 \hbar^2 S(S+1) \sum_j \frac{1}{r_{ij}^6}, \quad (2.43)$$

2.9.2 Motion reduced second moment

J. Senegas *et al.* calculate how the second moment would be reduced if given entities in the crystal suffer a reorientation movement around a given axis. This reduction can be estimated by a reduction term R [49]. This term is related with the secular part of the Hamiltonian and therefore with the variation of θ which is going to average $(1 - 3 \cos^2 \theta)^2$. Thus R is defined as

$$R = \frac{M_{2,reorient}}{M_{2,RL}},$$

where $M_{2,reorient}$ is the reduced second moment due to the reorientation.

⁵It is usual that M_2 is given in *gauss*². In those cases what it is really meant is $M_2^* = M_2 / \gamma_H^2$

According to the addition law of the spherical harmonics $\langle (1 - 3 \cos^2 \theta) \rangle$ can be rewritten as

$$\langle (1 - 3 \cos^2 \theta) \rangle = \frac{1}{2}(1 - 3 \cos^2 \theta')(3 \cos^2 \phi_{ij} - 1)^2,$$

where θ' are the angle between the reorientation axis Δ ⁶ and B_0 , and ϕ is the angle between Δ and the vector form by the union of the nuclei i and j .

In this case the possible values of θ' is also equiprobable as in Equation (2.41), whereby

$$\langle (1 - 3 \cos^2 \theta)^2 \rangle = \frac{1}{5}(3 \cos^2 \phi_{ij} - 1)^2$$

and $M_{2,reorient}$ is given as

$$M_{2,reorient} = \frac{3}{20} \left(\frac{\mu_0}{4\pi} \right)^2 \gamma_I^4 \hbar^2 I(I+1) N_i^{-1} \sum_{i,j} (3 \cos^2 \phi_{ij} - 1)^2 \frac{1}{r_{ij}^6} + \quad (2.44)$$

$$\frac{1}{15} \left(\frac{\mu_0}{4\pi} \right)^2 \gamma_I^2 \hbar^2 N_i^{-1} \sum_{i,k} \gamma_S^2 S(S+1) (3 \cos^2 \phi_{ik} - 1)^2 \frac{1}{r_{ik}^6}, \quad (2.45)$$

where N_i is the number of protons under which the summation is done.

2.9.3 The Gaussian approximation

Experimentally, if the spins are static and evenly distributed (as it is the case of abundant spins in solids) a Gaussian line shape is usually observed (See Figure 2.12). In resonance, the FID response function is expressed as:

$$G_x(t) = \exp \left(-\frac{1}{2} M_2 t^2 \right) \quad (2.46)$$

Starting from Equation (2.46), the corresponding Gaussian line shape can be calculated, leading to the expression

$$F(\omega) = \sqrt{\frac{\pi}{2M_2}} \exp(-\omega^2/2M_2) \quad (2.47)$$

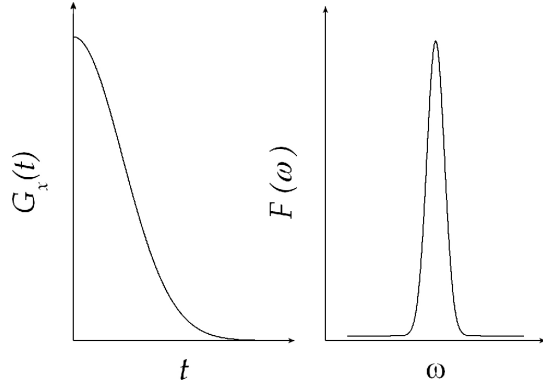


Figure 2.12: Form of the FID transient response ($G_x(t)$) and resonance spectrum ($F(\omega)$) using the Gauss approximation at resonance.

⁶The reorientation axis, Δ , is expected to be given by the the symmetry axis of the rotating object.

The exact spectrum is very difficult to be obtained or simulated. Therefore, the second moment of the sample becomes very important. The second moment (M_2) can be related to the linewidth of a sample for a spectrum with a Gaussian like form [75] as

$$\Delta\nu = \frac{\sqrt{M_2 2 \ln(2)}}{\pi}. \quad (2.48)$$

and vice versa, using the terms in Equation (2.43), the linewidth can be estimated taking the first neighbors of a given atom. This is valid on the rigid lattice approximation.

As we will explain in the section 2.11, sometimes a much narrower linewidth of the spectrum is observed experimentally. In this cases and for spectra with Lorentzian like lines, the linewidth of our spectrum can be related to the Spin-spin relaxation time (T_2) as:

$$\Delta\nu = \frac{1}{\pi T_2} \quad (2.49)$$

2.10 Distance determination by NMR in solids

In solids, where the atoms are static and evenly distributed, it can be assumed that the dipolar decay constant is proportional to M_2 or (as explained in Section 2.9.1) inversely proportional to the sixth power of the distance between the atoms .

As explained in Section 2.6, the refocusing of the NMR signal (when very strong dipolar interactions are present) can be achieved by the Magic Echos (ME and MHE). Similar to the experiment done to obtain T_2 , we obtain the M_2 with the ME (see Eq. (2.46)): The experiment has to be repeated for the different τ values (see Figure 2.8), in order to obtain the homo- and heteronuclear contributions of M_2 values. After that, one has to plot the amplitudes *vs* the square of the different evolution times, t^{*2} .

The evolution time is the one during which each interaction is active. In the sandwich of the ME the homonuclear interaction is refocused, and the heteronuclear interactions is averaged to zero. Therewith only the homonuclear interaction is active and different of zero outside the pulse. Therefore its evolution time is 2τ . The decay of the echo for each different experimental τ used is given by G_{ME} like

$$G_{ME} = G_1 \exp \left(-\frac{M_{2,IS} + 9 \cdot \epsilon_0}{2} t^{*2} \right) = G_1 \exp \left(-\frac{M_{2,ME}}{2} t^{*2} \right), \quad (2.50)$$

where ϵ_0 is an extra term which does not depend on the dipolar interactions but on experimental imperfections like incomplete canceling of the irradiation along the x and $-x$ direction in the rotating frame. As the imperfections are active during the whole pulse sequence, its evolution time should be 6τ and not 2τ . In the experiment, we study the decay of the signal as a function of $t^{*2} = (2\tau)^2$, that is why we use the factor 9 before ϵ_0 .

With the MHE we expect to refocus not only the homonuclear but also the heteronuclear interactions. From its propagator (in analogy with Eq. (2.33)) one would expect an horizontal line. In the reality though, one has a decay which will be given by ϵ_0 , i.e., by the already mentioned

experimental imperfections. Therefore the MHE signal will be given as:

$$G_{MHE} = G_1 \exp\left(-\frac{\epsilon_0}{2} t^{*2}\right) = G_1 \exp\left(-\frac{M_{2,MHE}}{2} t^{*2}\right), \quad (2.51)$$

where its evolution time is again 6τ .

Thus the $M_{2,IS}$ can be obtained by the decay of the magic echo ($M_{2,ME}$) minus 9 times the decay of the $M_{2,MHE}$ or ϵ_0 .

Finally the free induction decay is given by

$$G_{FID} = G_1 \exp\left(-\frac{M_{2,II} + M_{2,IS} + \epsilon_0}{2} t^{*2}\right),$$

here the evolution time is the same as the laboratory time (the “normal” one). The homonuclear second moment can be then obtained by subtracting from the exponent of the free induction decay, the already obtained value of $M_{2,IS}$ and ϵ_0 .

2.11 Motional effects

One of the most important and useful features of NMR is its ability to probe molecular motion. The nature and way of studying each motional effect depends on its timescale.

The motional process detectable by NMR run from picoseconds to several seconds and have different effects in our NMR measurements. The different motional timescale and their effects are represented in Figure 2.13 [60].

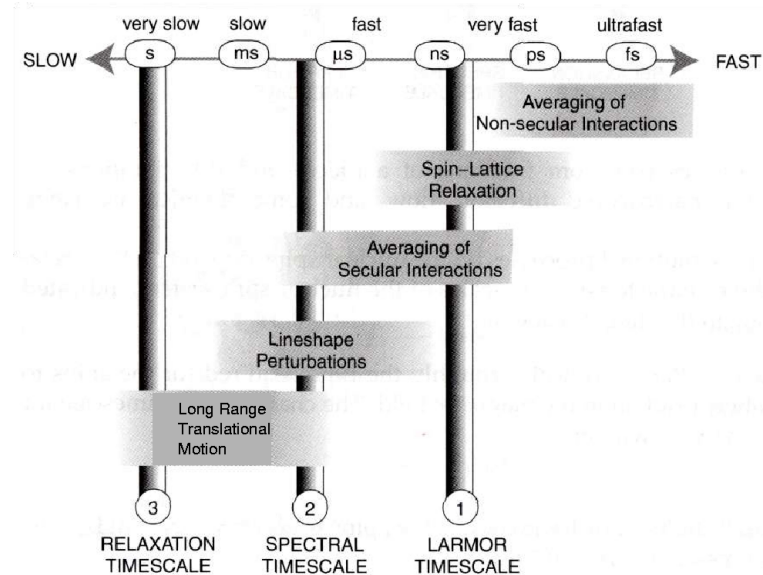


Figure 2.13: Motional effects associated with the different NMR timescales [60]

1. The *Larmor timescale* is given by the time required for the spins to make one full precession in the stationary magnetic field. For example, if the Larmor frequency of the spins is given by $\omega_0/2\pi = -67.7\text{MHz}$, as for protons in our NMR magnet, then $\tau_0 \sim 2.35\text{ ns}$, where $\tau_0 = 1/\omega_0$. For a 300 MHz spectrometer, $\tau_0 \sim 0.53\text{ ns}$.
2. The *spectral timescale* is given by the inverse width of the NMR line, i.e., $\tau_{spe} \sim 1/(2\lambda) \text{ s}$, where 2λ is the linewidth (see Figure 2.11).
3. Finally, the *relaxation timescale* is given by the T_1 value (see section 2.8.1).

Processes which are faster than the Larmor timescale can not be directly measured. These terms average the Hamiltonian before the secular approximation is made (see section 2.2.1) and are usually not important for us⁷.

For processes that are slower than the *Larmor timescale* an averaging of the secular spin Hamiltonian terms takes place, in addition to the non-secular averaging. The way in which the different motional effects average of the secular interactions can be studied by NMR. They are specifically important as a cause of spin-lattice relaxation and the line shape perturbations. 2.13 The principal effects of motion on the nuclear spin dynamics are written at different timescales in the Figure 2.13:

1. Spin-lattice relaxation

In section 2.8.1 was already explained how the spin-lattice relaxation rate, $\Gamma_1 = 1/T_1$, can be measured. Several interactions can contribute to Γ_1 . The dipolar contribution to Γ_1 (which dominates in our case) provides information of the dynamical processes in our sample. The magnetization will re-establish itself along the z direction as given by the Equation (2.35). The relaxation is mediated by the motional processes like molecular rotations, diffusion of particles or lattice vibrations.

The easiest way of visualizing the behavior of the particle is using the classical model of diffusion of light particles in a host lattice. It is supposed that each particle is located in a potential well and stays there for a given dwell time, τ_d .

The nuclear spin-lattice relaxation rate, Γ_1 , can be described according to the BPP-model equation [76] by

$$\Gamma_1 = \frac{1}{T_1} = \frac{2}{3} M_2 \left[\frac{\tau_c}{1 + \omega_0^2 \tau_c^2} + \frac{4\tau_c}{1 + 4\omega_0^2 \tau_c^2} \right],$$

where the 'NMR correlation time', τ_c , is the mean time after which the dipolar interaction has changed. It differs in general from the dwell time, τ_d , of the mobile nuclei. In the case of the interaction of two identical spins, being both mobile, $\tau_c = \tau_d/2$.

The diffusion of the particles depends on the probability that a particle has enough thermal energy to overcome the energy barrier between neighboring sites. Having a thermally activated process, the jump frequency of the particles (ν^*) obeys in many cases the Arrhenius law, i.e.,

$$\nu^* = \nu_p e^{-H_a/k_B T}, \quad (2.52)$$

⁷Occasionally these motional effects can be the reason of discrepancies in the values of the spin interaction parameters like the dipolar coupling due to rapid vibrational motions. In those cases, the parameters should be corrected.

where H_a is the activation enthalpy, which gives the height of the potential and ν_p is typically related to a vibrational frequency of the ion at its equilibrium position.

In Figure 2.14, we show the spin-lattice relaxation rate *vs* temperature under the assumption of a single thermally activated process of motion for two different measuring frequencies. The slopes of those curves give H_a/k_B in the high T limit and $-H_a/k_B$ in the low temperature limit. Thus Γ_1 can be written in the limit of high and low temperature as

$$\Gamma_1 \propto e^{H_a/k_B T} \propto \tau_c \text{ for } \omega_0 \tau_c \ll 1 \text{ ("high temperature limit")} \quad (2.53)$$

and

$$\Gamma_1 \propto e^{-H_a/k_B T} \propto 1/(\tau_c \omega_0^2) \text{ for } \omega_0 \tau_c \gg 1 \text{ ("low temperature limit").} \quad (2.54)$$

When $\omega \tau_c \simeq 1$ the correlation time can be estimated.

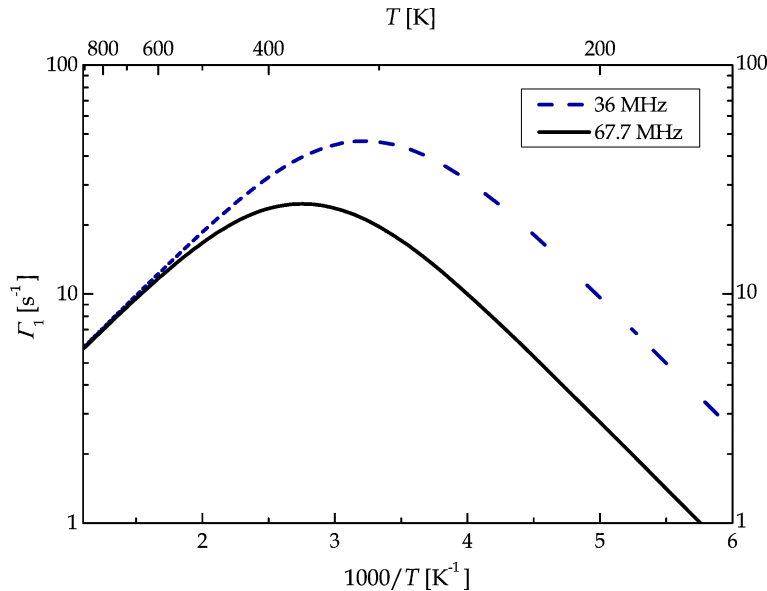


Figure 2.14: Spin-lattice relaxation rate *vs* the inverse of temperature ($1000/T$) for two different measuring frequencies, under the assumption of a single thermally activated process of motion.

The diffusion coefficient, D , can then be estimated, by assuming that the ion undergoes uncorrelated jumps of length l (usually $l \approx 0.3 \text{ nm}$) at a rate $\nu_d = 1/\tau_d$, as

$$D = l^2 \nu_d / 2d, \quad (2.55)$$

where d is the dimensionality of the system ($d = 1, 2, 3$).

2. Spectral line shape perturbations- Motional narrowing

Process around the spectral time scale ($\tau_{spe} \sim 1/\Delta\nu$, where $\Delta\nu = 1/(2\lambda)$) affect the line shape strongly. A real sample is composed of atoms with different certain vicinities and their different local magnetic fields. There is, therefore, a certain distribution of resonance frequencies within the sample. This results in a broadened NMR line. Provided that the

temperature is sufficiently high, the spins can jump between the different vicinities. The change in the precession frequencies causes a dephasing of the transverse magnetization. At low temperatures (when the rigid lattice condition is accomplished), the jump probability is very remote. The spins make no move on the spectral timescale. Therefore it plays only a negligible role [77]. The FID of the sample is given then by the distributions of the resonance frequencies. We have therefore broad lines in the rigid lattice case.

The only important change of the line shape for our investigations is the so-called **motional narrowing**. It occurs when the temperature is increased and the jump probability gets bigger. We begin to have now self diffusion of the spins. This overshadows the equilibrium that we had in the rigid lattice. The spins begin to 'feel' a space average of the accessible vicinities. This leads to a longer transverse magnetization decay signal, i.e., to longer FIDs or narrower NMR line. Around this time scale, $\Delta\nu$ can be well fitted to an Arrhenius like equation of the form

$$\Delta\nu = \nu_0 \exp(H_a/kT). \quad (2.56)$$

3. Long range translational motion

In our samples, hydrogen atoms undergo translations (motions in space), when the temperature of the sample is increased to the release temperature. We expect to have then a flow (a concerted and directed motion) or diffusion (random and uncoordinated motion) of the hydrogen atoms.

Detection of macroscopic diffusion or flow by NMR is possible by Pulsed Field Gradient - NMR (PFG-NMR) measurements. Within a magnetic field gradient, the spin Hamiltonian changes as the molecules move into a different region of space (Figure 2.15). The motion of the molecules in the direction of the gradient changes their Larmor frequency. The effect of the PFG is usually measured in combination with a Hahn echo pulse sequence. Therefore mentioned two types of motion have different effects on the echo. While diffusion changes the amplitude of the echo, flow changes the phase. However, in order to be able to measure experimentally with our experimental set-up, the value of T_2 should be bigger than 1 ms. That is the minimum time needed to apply the field gradient, i.e., to turn it on and off.

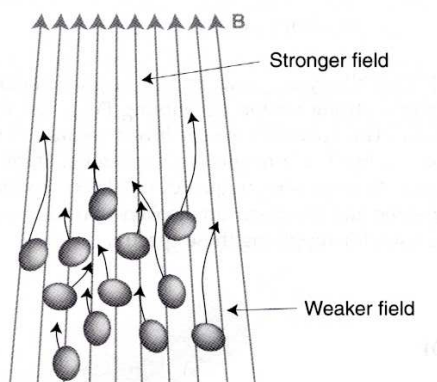


Figure 2.15: The flow of molecules in a magnetic field gradient [60]

3 Experimental set up

Most of this work was done with a non-commercial spectrometer. Our home-built spectrometer was developed for diffusion studies in solid and liquid systems. It is a very flexible apparatus, completely computer controlled but unfortunately a bit outdated, too. This implied that it needed a lot of maintenance. Due to the fact that my thesis is the last one realized in our Lab and even though I was always supported by my boss and the technicians of MPI, most of the reparations were mainly done by myself. Beyond any doubt I spent, adding all reparation time, more than one and a half years of my PhD. In this chapter the most important parts of our pulse NMR spectrometer are in detail described, as well as the improvements and the most important reparations performed are listed.

Our NMR spectrometer

Figure 3.1 shows a diagram with the parts of our NMR spectrometer. It was a fully computer controlled spectrometer, which consists of five main parts: the superconducting magnet, signal generation (r.f. pulse), signal detection, the probe and the temperature control. All these parts are controlled by a principal computer. The parts drawn inside the magnet in Fig. 3.1 represent the “Probe” (See Section 3.1).

Superconducting magnet

The superconducting magnet used to generate the static magnetic field has had a magnetic field of about 1.6 T. This field corresponds to a proton resonance frequency of about $\omega/2\pi = 67.7$ MHz.

The NMR magnet has a so-called “room temperature” bore in its center, which is isolated from the superconducting coil. This bore is used to introduce the probe (see Section 3.1) into the magnet.

3.1 Parts of the measurement process

Likewise, the entire measurement process can be divided in 2 sections, each of them achieved by the listed apparatuses:

- Signal Generation (r.f. pulse)

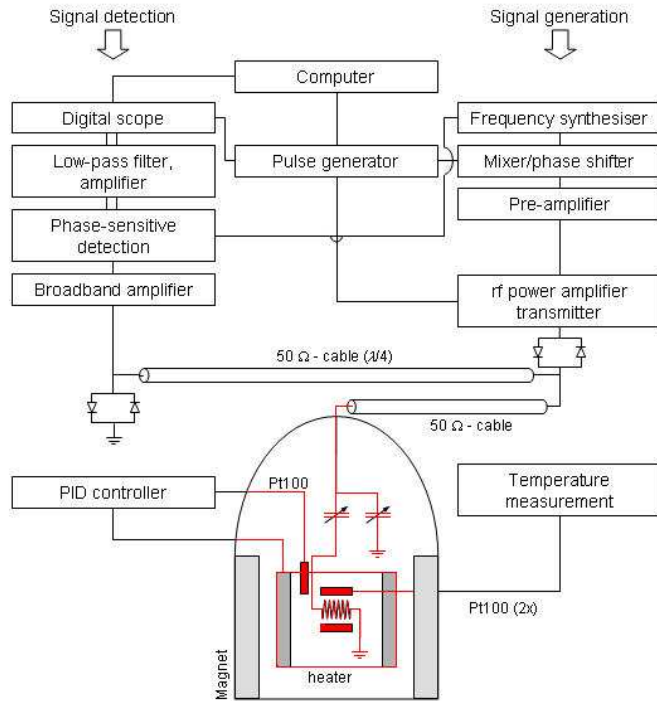


Figure 3.1: Parts of our NMR Spectrometer. The spectrometer is fully controlled by a principal computer. It consists of five main parts: the superconducting magnet, transmitting section or signal generation (frequency synthesizer, mixer/phaser shifter, pre-amplifier), signal detection (digital scope, low-pass filter, phase sensitive detection, broadband amplifier), analysis of the data and the probe[8]. (see Section 3.1)

- Frequency synthesizer
- Mixer
- Phase shifter
- Pre-amplifier
- Signal Detection
 - Broadband amplifier
 - Phase sensitive detection
 - Low-pass filter
 - Digital scope
 - Power amplifier

Signal generation

This part is in charge of the generation of the r.f. pulses. The stages followed by r.f. signal (see Figure 3.2) are explained below:

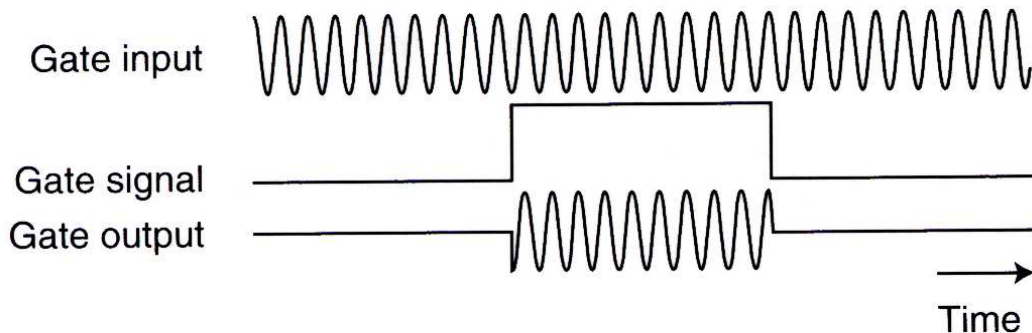


Figure 3.2: A scheme of the formation of the transmitted signal[60]

1. A **radiofrequency (r.f.) synthesizer** produces an oscillating voltage with a frequency around the Larmor Frequency ω_0 . This is the precession frequency of the spins in the static magnetic field, also called the carrier frequency of the NMR experiment.
2. The **pulse programmer** generates a sequence of digital TTL pulses which correspond to the pulse sequence required for a particular NMR experiment (“Gate signal” in Fig. 3.2). We use a computer-controlled pulse programmer which is freely programmable for any kind of pulse sequences.
3. The r.f. pulses are obtained by **mixing the digital pulses** with the carrier frequency from the r.f. synthesizer and a reference phase (“Gate output” in Fig. 3.2). This reference phase is important as the phase - alternating pulse schemes is used to detect the signal (see Section **Signal detection**). The pulse is strongly **amplified** by sending it to the r.f. amplifier. This has an output power of up to 1 kW. The amplifier is controlled (turned on or off) by using a gating pulse sequence which requires a TTL pulse (it should have 5 V amplitude).
4. Finally, between the r.f. power amplifier and the probe there is a pair of crossed diodes. These diodes have a very large differential resistance, i.e., they only allow signals with high amplitudes to go through. Therefore only r.f. pulses with high amplitudes will reach the probe whereas noise coming from the amplifier can not pass through (this noise would spoil the signal-to-noise ratio).

After the generated r.f. pulse passed the before mentioned crossed diodes, the signal could follow two branches (see Figure 3.1). One of the branches goes to the r.f. circuit in the magnet while the other is directed to the signal detection section. The r.f. pulse must not go to the detection branch because the power of that pulse would damage our detection system. To avoid that, we used a **$\lambda/4$ -cable** (a cable with the length of a quarter of the r.f. wavelength) in combination with a grounded pair of crossed diodes. This setup results in a very high impedance for a large r.f. pulse (coming from the signal generation branch) and oppositely in a very low impedance for a very small NMR-signal (coming from the sample).

These impedances assure respectively that the whole r.f power will be sent in the probe and that the NMR-signal coming from the sample will be sent to the signal detection branch.

Signal detection

After the pulse is applied to the sample, the precession of the spins generates an induction signal in the coil surrounding the sample. This signal is the so-called NMR signal. The data acquisition is then triggered. It can, however, only be recorded after the spectrometer dead time. This time is in our spectrometer typically of the order of $10 \mu\text{s}$ ¹.

The path of the signal detection takes the following stages:

1. **Broadband amplifier.** The signal of the spin in the sample must be first amplified.
2. **Phase sensitive detection and low-pass filter.** The signal is splitted in two parts. This is done by multiplying the signal by the sine and cosine of the reference angular frequency ω_0 . The combination of both signals can be mathematically seen as the sine and cosine of the sum of $\omega + \omega_0$ and the difference of $\omega - \omega_0$. When this signal pass through a low-pass filter, the contributions of the sum frequency ($\omega + \omega_0$) are eliminated. The frequency window is reduced thus to that one which represents our experimental range. This signal represents the one of the rotational reference system.
3. **Digital scope.** The NMR signal is digitalized in a two-channel transient recorder with a maximum frequency of 20 MHz and 8 bit resolution. Since the NMR signal was very small, it was necessary to amplify the signal considerably. A form to increase the signal-to-noise ratio is by repeating the experiment many times. The signal is added in the digital scope up to 1000 times, and averaged at the end.

Data analysis

Finally, the obtained NMR data are sent to the principal computer. The spectrum of the sample is found by applying a Fourier Transformation (FT) to the signal. The spectrum corresponds to the representation of the FID in the frequency domain.

Probe

The probe (See Figure 3.1 - the parts drawn inside the magnet) is introduced into the “room-temperature bore” of the magnet . The sample is placed in the probe, inside of a small r.f. coil. This probe is suitable for CW-NMR and pulse-NMR.

The r.f. pulses are applied to the sample by using the already mentioned coil shown in the Figure 3.1. We also used the same coil to detect the NMR signal.

¹This time is reduced up to $3 \mu\text{s}$ in e.g. a standard Bruker CXP 300 Spectrometer like the one used for the last experiments. Those were done by Prof. Müller Group in the Uni-Stuttgart.

Temperature changes were determined by measuring the resistance of two platinum resistors (Pt100), which were located around the sample.

Temperature control

The temperature was maintained with an uncertainty of about 1 K. This is done by using a digital PID controller combined with an ohmic heating system. Temperature was monitored using two platinum resistors placed around the sample (see Section 3.1). Temperatures below room temperature were achieved by flowing liquid nitrogen and helium in a separated cryostat. The cryostat is enclosed to the “room-temperature bore” of the superconducting magnet. For temperatures above room temperature the sample can be heated by a heating coil ($30\ \Omega$) surrounding r.f. coil with the sample.

Improvements and reparations

1. The most difficult reparation was performed on the interface of the pulse programmer. This programmer is in charge of the gating sequence which generates the r.f. pulses, controls the amplifier and triggers data acquisition. This interface should give a pulse of about 5 V. The problem arose because the amplitude of the pulse was sometimes too low to be recognized as a TTL pulse. The experiments failed in an almost random way (the measurements were mostly working but sometimes were interrupted without any apparent reason). This often ruined not only the measurements, but the sample, and my sense of humour. It took us quite a long time to discover this problem.
2. The magnet has quenched twice. The first malfunctioning was due to a failure of the isolation, and the second time because of a failure of the helium level measuring device. The failure of the isolation was repaired by changing the O-rings of the magnet for O-rings with a quadratic profile. For the second malfunctioning, we recalibrated the helium level measuring device. In both cases, the reinstallation of the magnet after the quench was very time consuming. The whole system needed to warm up in order to get rid of condensed water inside the magnet and to obtain a reasonable vacuum in the isolation cavity. In addition, we needed to cool down the system, turn on the magnetic field, and finally homogenize it by a shimming procedure. This is performed using an Oxford “intelligent- superconducting-magnet” power supply.

4 Experimental and numerical details

4.1 Sample preparation

We got the samples through a cooperation with Dr. Maximilian Fichtner of the *Karlsruhe Research Centre*. Therefore, the preparation of the samples is here just briefly depicted.

NaAlH_4 was purchased as powder (Chemetall, Frankfurt). It was purified by a so-called Soxhlet extraction with 500 ml distilled tetrahydrofuran as described in Ref. [36]. About 400 ml were then drawn off under vacuum. Large colorless crystals (about 0.5 mm) of NaAlH_4 were obtained from that extract. The crystals were then washed with dry diethylether and dried at ambient temperature under vacuum, until a residual pressure of 1×10^{-3} mbar was reached. After that the purified NaAlH_4 contained 7.7 ± 0.1 wt. % H_2 and 0.2 ± 0.1 wt. % C.

The Na_3AlH_6 sample was prepared by mechanical alloying (ball milling) appropriate amounts of NaAlH_4 and NaH [36].

Finally, the NaH sample was obtained by ball milling purified NaAlH_4 followed by thermal desorption under vacuum at 443 K.

Sample milling and doping

The milling of the samples was done with a milling vial (Figure 4.2(a)). Both the milling-vial and the balls were made of silicon nitride¹. This material was chosen to avoid magnetic impurities in the sample as much as possible (this could affect our measurements).

Milling was also used to disperse the catalyst uniformly into the sample. For this reason, the catalyst was introduced together with the material into the vial. This was done under inert gas conditions (Ar -filled glovebox) because NaAlH_4 is quite reactive with oxygen and air humidity [78]. The ball milling vial was then sealed and introduced to a Fritsch P6 planetary mill (Figure 4.2(b)). All treated samples have been milled at 600 rotations per minute. The milling times, with exception of the sample with only 5 minutes ball-milling, were divided into intervals of 15 minutes with pauses of 10 minutes in between.

¹For 2 grams of sample, we used 8 balls: 6 with a diameter of 0.5 cm and 2 of 1.0 cm.



Figure 4.1: (a) Ball milling vial.

Figure 4.2: (b) Fritsch P6 planetary mill.

NMR Samples

In this work, we report mainly about two kinds of samples. The first kind was milled 30 minutes with $Ti_{13} \cdot 6THF$ catalyst. The samples doped with 1, 2 or 5 mole % catalyst are called for simplicity 1, 2 or 5 mole % samples, respectively. The second kind of samples was also milled but without catalyst. A list of all samples used, their characteristics and the measurements done on them are presented in the Tables 4.1, 4.2, 4.3, and 4.4.

The first sample with 2 mole $Ti_{13} \cdot 6THF$ catalyst was ball-milled and stored for months in liquid nitrogen. The temperature of the sample was increased from the liquid nitrogen temperature to room temperature using nitrogen gas. During removal of the sample from the liquid nitrogen tank, air humidity could have affected the sample.

We prepared a second sample with 2 mole % catalyst for the measurements done with the 300 MHz spectrometer. The sample was ball-milled half a day before we started the measurements (to determine the structure).

The samples with 1 and 5 mole % $Ti_{13} \cdot 6THF$ catalyst were prepared in the same way – the evening before the first measurements as a function of temperature were done (measurements of the spectra and of the Γ_1 rates).

The samples without catalyst were prepared half a day before measurements of the spectra and of the Γ_1 rate as a function of temperature were performed. These samples were milled for 5 and 30 minutes, and for 12 hours.

Sample filling

For the NMR measurements the material was filled into teflon tubes under inert conditions (inside the *Ar*-filled glove box). The tubes had an inner diameter of 7 mm and a length of 10 mm for the measurements done with the 67.7 MHz spectrometer, and 3 mm times 15 mm for those done with the 300 MHz spectrometer. Each tube was then sealed with Teflon screw caps. The tubes for the

67.7 MHz spectrometer had a capacity of about 200 mg of Ti-doped $NaAlH_4$. For the 300 MHz, the quantity of material was about 50 mg.

4.2 NMR measurements

An overview of all samples and measurements done are presented at the end of this section in Table 4.1, 4.2, 4.3, and 4.4.

Properties of the spectrometers

The NMR measurements were performed with two different spectrometers. The first measurements were done in our spectrometer, which is a home-made one, with a 1H -NMR resonance frequency of 67.7 MHz. Its $\pi/2$ -pulse length is about 2.1 μs . The minimum experimental dead time is 6 μs . All details of this spectrometer are given in Chapter 3.

The second series of measurements were performed with a Bruker CXP 300 Spectrometer operating at a proton resonance frequency of around 301.7 MHz, with a Tecmag control unit. The various experiments were done using a 5 mm Bruker double-resonance wide-line probe. The $\pi/2$ -pulse length was 2.7 μs and the minimum dead time was 3 μs .

All measurements done with both spectrometers were performed under static conditions (without using MAS). Like in the milling process, the measurements were performed under inert conditions. In order to do that, the bore of the superconducting magnet (where the probe is inserted) was evacuated and subsequently flooded with purified nitrogen gas.

NMR Spectra

The NMR Spectra were in all cases (at 67.7 MHz and 300 MHz) obtained by Fourier transformation of the free-induction decay (FID) following a single pulse or the second half of an echo (MHE or ME). To improve the signal-to-noise ratio, a total of 32 shots were accumulated to obtain each final spectrum with the 67.7 MHz spectrometer. The signal-to-noise ratio (S/N) depends on the gyromagnetic ratio (γ_n), and the static magnetic field (\mathbf{B}_0) as [60]:

$$S/N \propto |\gamma_n|^{5/2} |\mathbf{B}_0|^{3/2}. \quad (4.1)$$

At 300 MHz one has a S/N ratio which is about 10 times better than for the 67.7 MHz. Therefore only 4 shots were needed to be accumulated at 300 MHz to get a very good signal-to-noise ratio.

4.2.1 Measurements of the spectra and the Γ_1 rates as a function of temperature

Measurements at 67.7 MHz

In order to study the hydrogen dynamics in $NaAlH_4$, we measured the NMR spectra and the Γ_1 rates as a function of temperature on several $NaAlH_4$ samples. Already during the measurements these samples may undergo structural and/or compositional changes with temperature. Therefore

some effort was necessary to separate the effect (on the NMR spectra and on the Γ_1 rates) of the structural changes from those resulting from hydrogen motion (in a sample with a given structure and a given composition). The experiments were carried out therefore in a way that structure and/or composition of the used samples changed as little as possible, during the measurements.

The experimental protocol used in most studies was influenced by the experience gained during the first measurements on a sample with 2 mole % $Ti_{13} \cdot 6THF$ catalyst. On that sample, we measured down to low temperatures (down to 142 K). At those temperatures, it was difficult to maintain the temperature stable. As a consequence, the sample was exposed to several cycles within the temperature interval between 142 K and room temperature, for a period of more than three days. On the other hand, it was found that the NMR spectra and the Γ_1 rates did essentially not change within the above mentioned temperature interval. Thus, for our studies it was of more interest to look at higher temperatures. However, this sample was only heated up to 363 K as we were still afraid that the sample could burst during the measurements. After these measurements, however, it became clear that it did not seem to be a problem for the hydrogen to escape from the container of the sample. Therefore, on the other samples investigated, the measurements were mainly done at higher temperatures.

To avoid changes of the structure of the sample at higher temperatures, the measurements had to be performed as fast as possible. Admittedly, at higher temperatures structural and compositional transformation become faster, but the measurement times are also reduced (since the Γ_1 rates became higher²⁾. With which there is a better chance to prevent a decomposition in the sample, specially since the measuring time at temperatures above room temperature for each of the samples was less than 24 hours.

To check whether the samples did suffer structural changes, the reversibility of the room temperature measurements was tested. This means, that after the highest temperature was reached, the temperature was lowered to room temperature and subsequently the spectra and the Γ_1 rates were measured again. In order to determine the degree of decomposition into Na_3AlH_6 it was important to keep the amplification of the NMR spectrometer constant throughout all measurements. In this way, the amplitude of the NMR signal is a quantitative measure of the hydrogen content in the sample, and thus can be used to estimate how much hydrogen has been desorbed.

The temperature at which the measurements were performed was incremented stepwise by about 10 K in each step, starting from the lowest temperature. To be sure that the whole sample was homogeneously warmed (or cooled), at each temperature we waited at least 30 minutes before the measurement was started. Once the temperature was homogeneous, we first obtained the spectra followed by a Γ_1 measurement.

The data of the sample with 1 mole % catalyst were taken in the temperature range from 297 to 380 K, and on the sample with 2 mole % catalyst from 142 to 363 K. The sample with 5 mole % catalyst was measured from 268 to 361 K. (The final room temperature measurement was unfortunately not done for this sample.)

² T_1 ($T_1 = 1/\Gamma_1$) is important as it determines the waiting time between measurements.

The samples which were ball-milled without catalyst were studied in the temperature range from 278 K to 361 K in case of the sample milled for 5 minutes, from 309 K to 372 K in case of the sample milled for 30 minutes, and finally in case of the sample milled for 12 hours from 296 K to 369 K.

The sequence used to measure Γ_1 was inversion recovery for the samples with 12 hour ball-milled without catalyst. For the rest of the samples, to measure Γ_1 , a saturation recovery pulse sequence was used.

All details of the $NaAlH_4$ samples used as well as the NMR measurements are summarized on the Tables 4.2 and 4.3.

Measurements at 300 MHz

Γ_1 rates were also measured as a function of temperature at 300 MHz but on another sample (second sample) with 2 mole % catalyst. The sample used for this measurement was ball-milled one and a half day before these measurements were done. In this case we measured from 215 K to 365 K. With this NMR spectrometer it was not possible to maintain the amplification constant during the whole measurement.

4.2.2 Measurements of the spectra and the Γ_1 rates at a given temperature as a function of time

The focus of the studies described in the previous section was on the investigation of hydrogen motion as a function of temperature while the structure and composition of the sample changes as little as possible. By contrast, in this section experiments are described which are carried out in order to follow and to study structural and compositional changes, which occur due to the decomposition of $NaAlH_4$ into Na_3AlH_6 as a function of time. The temperature was kept constant³ in these experiments in order to study just temporal changes.

The samples with 1, 2, and 5 mole % $Ti_{13} \cdot 6THF$ catalyst were heated at once from room temperature to 336 K, 338 K, and 329 K, respectively (i.e., at around 335 K). Those temperatures were chosen because e.g. at around 335 K, hydrogen certainly desorbs but not too fast to prevent detection of this process.

Similar as in the measurements done as a function of temperature, we waited for 30 minutes till the temperature became homogeneous. The origin of the time axis was chosen after those 30 minutes passed.

The amplification of the NMR spectrometer was kept constant throughout all measurements, in order to determine the degree of decomposition into Na_3AlH_6 from the amplitude of the NMR signal. Only for the last measurements in the sample with 5 mole % catalyst, the amplification of the NMR signal was adjusted.

³As the temperature controller operated independently from the rest of the spectrometer, the temperature is guaranteed constant the whole time (even during the time in which we were not measuring).

The measurements described above were the last ones done in this work. For them, we used the non-used part of the batches of catalyzed samples that we produce for the measurements as a function of temperature. Catalyzed samples and specially those catalyzed with $Ti_{13} \cdot 6THF$ lose hydrogen already at room temperature [36], [8]. Therefore, the samples contain a certain fraction of Na_3AlH_6 , if stored for some time at room temperature. The sample with 1 mole % catalyst, e.g., was prepared 4 months before being measured and the sample with 5 mole % 5 days before. The sample with 2.0 mole % $Ti_{13} \cdot 6THF$ catalyst was maintained at room temperature for 15 days before the measurements were done.

An overview of all details of the $NaAlH_4$ samples used as well as the NMR measurements of this section are summarized on the Table 4.4 at the end of this chapter.

4.2.3 Structure determination measurements

For the structure determination measurements, we took a sample with 2 mole % $Ti_{13} \cdot 6THF$ catalyst prepared one day before the measurements were done. This sample was chosen because of its short spin-lattice relaxation time, which is in the range of a few minutes⁴.

The length of the so-called burst pulses in the ME pulse sequence varied between 1.25 and 25 μs . The FID used to determine the complete dipolar decay was the second half of the MHE, which was obtained with a $\tau=5 \mu s$.

All structure determination measurements were performed at room temperature and as usual under inert gas conditions.

The amplitudes of the ME and the MHE were obtained by integrating over the spectra (see e.g. the graph shown in Figure 5.42). As shown in Figure 5.7 on page 62, the experimental spectra at room temperature are composed of a narrow and a wide line, i.e., of two components. We separate both components by fitting two lines and then integrating the wide line one obtains the amplitude of the ME and the MHE. The whole process was done using the program matNMR [79].

Second moment calculations

To calculate the second moments, we first used the lattice parameters given by V. Ozolins *et al.* [26] ($I4_1/a$ space group, with $a=5.0119(1) \text{ \AA}$, $c=11.3147(4) \text{ \AA}$ at room temperature).

The second moment was calculated over all atoms (hydrogen, aluminum and sodium atoms) up to a distance of 8.0 \AA from a given proton. The contributions of nuclei at a larger distance were estimated to be less than 1 % of the calculated values. The distances were obtained from Dr. Ivan Halasz and they were obtained using the program Diamond version 3.1f, Crystal Impact, 2008.

⁴The T_1 rate for an untreated sample was of about 1 hour. Thus, one has to wait up to 5 hours between measurements

4.2.4 Overview

A summary of all measurement, as well as the characteristics of the samples measured are presented in Tables 4.1, 4.2, and 4.3.

Table 4.1: Summary of the samples used and the measured spectra at room temperature (RT) and low temperatures. On the bottom are given the details of the sample used for the structure refinement of $NaAlH_4$. The figures (in which the corresponding results are presented) are also given.

Measurement						
Sample	Catalyst proport.	Milling time [%]	Meas. temp. [K]	Dead time [μs]	Details of the sample/measurement	Shown in Figure
Spectra						
$NaAlH_4$	—	—	RT	10		Fig. 5.1, Fig. 5.4
	—	—	RT	3		Fig. 5.2
				10	Diff. purification quality	Fig. 5.3
			130	10		Fig. 5.4
			RT	—	2nd half of the MHE Gaussian approx.	Fig. 5.5 Fig. 5.8
	2	30	215	—	2nd half of the MHE Gaussian approx.	Fig. 5.6 Fig. 5.8
	2	30	RT	—	2nd half of the MHE Gaussian approx.	Fig. 5.7 Fig. 5.8
Na_3AlH_6	—	—	RT	10		Fig. 5.1
NaH	—	—	RT	20		Fig. 5.1
Structural analysis of $NaAlH_4$						
$NaAlH_4$	—	5	278 to 361	6	FIDs (after a $\pi/2$ -pulse) as a function of t^2 , freshly prepared.	Fig. 5.39
$NaAlH_4$	1	30	297 to 380	6	FIDs (after a $\pi/2$ -pulse) as a function of t^2 , freshly prepared.	Fig. 5.16, Fig. 5.40
Experimental determination of the homo- and heteronuclear M_2						
2nd half of the MHE, MHE decay, ME decay						
$NaAlH_4$	—	30	RT	—	Freshly prepared	Fig. 5.41
$NaAlH_4$	2	30	RT	—	Freshly prepared	Fig. 5.42

Table 4.2: Summary of the samples used on the measurements of the spectra as a function of $1000/T$ (where T is the temperature). The temperature intervals, at which the measurements were done, are given. All these measurements were done at 67.7 MHz, with a dead time of $6 \mu\text{s}$. The figures (in which the results are plotted) are listed. The variables (the normalized amplitudes ($A_N = A/A_T$) or the linewidths ($\Delta\nu$)) that were plotted as a function of $1000/T$ in the figures are indicated.

Measurement						
Sample	Catalyst prop [%]	Milling time [min]	Measuring temp. [K]	At RT for [days]	Shown in Figure	Variable plotted vs $1000/T$
Spectra as a function of temperature						
$NaAlH_4$	—	5 5	278 to 361 Room temp.	—	Fig. 5.10 Fig. 5.11	
	—	30	309 to 372.	—	—	
	—	12 hrs 12 hrs	296 to 369. Room temp.	—	Fig. 5.12 Fig. 5.13	
$NaAlH_4$	1	30	297 to 380 Room temp.	—	Fig. 5.14 Fig. 5.15	
			297 to 380	—	Fig. 5.16 Fig. 5.17	A_N^* , 2 comp.
				—	Fig. 5.18	$\Delta\nu$, 2 comp.
				—	Fig. 5.19	$\Delta\nu$, 3 comp.
$NaAlH_4\text{-I}^\dagger$	2	30	142 to 363	—	Fig. 5.16 Fig. 5.17 Fig. 5.18 Fig. 5.19	A_N , 2 comp.
	5	30	268 to 361	1	Fig. 5.16 Fig. 5.17 Fig. 5.18 Fig. 5.19	$\Delta\nu$, 2 comp. $\Delta\nu$, 3 comp. A_N , 3 comp.

Table 4.3: Summary of the samples used on the spin-lattice relaxation rates (Γ_1) measurements done as a function of $1000/T$ (where T is the temperature). The temperature intervals, at which the measurements were done, are given. All these measurements (except for those on the $NaAlH_4$ -II[†] sample) were done at 67.7 MHz, with a dead time of 6 μs . At 300 MHz the $NaAlH_4$ -II[†] sample was measured. This measurements (at 300 MHz) had no dead time as the magnetization was detected by a MHE pulse sequence. The figures (in which the results are plotted) are listed. The variables that were plotted as a function of time in the Figures (Γ_{1i} rates, the total amplitude (A_T), the amplitudes of the components (A_i) and the normalized amplitude (A_N)) are indicated.

Measurement						
Sample	Catalyst prop [%]	Milling time [min]	Measuring temp. [K]	At RT for [days]	Shown in Figure	Variable plotted vs $1000/T$
Γ_1 as a function of $1000/T$						
$NaAlH_4$	—	5	278 to 361	0.5	Fig. 5.21 Fig. 5.22	Γ_1 meas. $A_T * T$
	—	30	309 to 372.	0.5	Fig. 5.21 Fig. 5.22	Γ_1 $A_T * T$
	—	12 hrs	296 to 380.	0.5	Fig. 5.21 Fig. 5.22	Γ_1 $A_T * T$
	1	30	297 to 380	0.5	Fig. 5.25 Fig. 5.28	$\Gamma_{1i}, i=1,2$ A_i
$NaAlH_4$ -I [†]	2	30	142 to 363	0.5	Fig. 5.30 Fig. 5.26 Fig. 5.28 Fig. 5.30	A_N Γ_{1i} A_i A_N
$NaAlH_4$ -II [‡]	2	30		1.0	Fig. 5.26	Γ_{1i}
	5	30	268 to 361	0.5	Fig. 5.27 Fig. 5.28 Fig. 5.30	$\Gamma_{1i}, i=1,2$ A_i A_N

[†] The $NaAlH_4$ -I sample stored several months in liquid nitrogen.

Table 4.4: Summary of the samples used for measurements as a function of time of the spectra ($F(\nu)$) and spin-lattice relaxation rates (Γ_1) at 67.7 MHz. The corresponding Figures (in which the results are plotted) are tabulated. The variables that were plotted as a function of time in the corresponding Figures (like the amplitudes of the each variable (A_i) or the total amplitudes (A_T)) are listed.

Measurement						
Sample	Catalyst prop [%]	Milling time [min]	Measuring temp. [K]	At RT for [days]	Shown in Figure	Variable plotted <i>vs</i> time
Spectra as a function of time						
$NaAlH_4$	1	30	336	120	Fig. 5.14	$F(\nu)$
$NaAlH_4$ -I [†]	2	30	338	15	—	
	5	30	329	5	—	
T_1 as a function of time						
$NaAlH_4$	1	30	336	120	Fig. 5.33 Fig. 5.36 Fig. 5.36	$\Gamma_{1i}, i=1,2$ A_i A_T
$NaAlH_4$ -I [†]	2	30	338	15	Fig. 5.34 Fig. 5.37 Fig. 5.37	Γ_{1i} A_i A_T
	5	30	329	5	Fig. 5.35 Fig. 5.38 Fig. 5.38	Γ_{1i} A_i A_T

[†] The $NaAlH_4$ -I sample was stored several months in liquid nitrogen.

5 Results

In this thesis, we have studied the structural and dynamical properties of hydrogen in sodium alanates by applying different NMR techniques. The experimental results are presented below, and they are discussed together with published data.

Section 5.1 presents proton NMR spectra of $NaAlH_4$, Na_3AlH_6 , and NaH at room temperature. The products Na_3AlH_6 and NaH are formed as a result of decomposition reactions of $NaAlH_4$. The spectra were obtained by Fourier transform of the free induction decay (FID) followed after a single $\pi/2$ r.f.-pulse, excluding signals prior to a given dead time. The spectra of $NaAlH_4$, Na_3AlH_6 , and NaH are clearly distinct at room-temperature. The NMR spectra were obtained by Fourier transform of the second half of the Magic Hahn Echo (MHE) without having any distortions due to an experimental dead time. At room temperature, samples of $NaAlH_4$ ball-milled with catalyst ($Ti_{13}\cdot 6THF$ catalyst) have qualitatively similar spectra – as the samples without catalyst – with exception of an extra central peak. The extra central peak has been caused by a small sample proportion decomposed into Na_3AlH_6 during the ball-milling process.

Section 5.2 presents NMR studies of hydrogen dynamics in $NaAlH_4$ by using spectra and spin lattice relaxation rate (Γ_1) as a function of temperature. We studied samples which were ball-milled for 30 minutes together with catalyst, but also samples without catalyst, which were ball-milled for 5 and 30 minutes as well as 12 hours. Ball-milled samples without catalyst showed no remarkable change as a function of temperature in the spectra (in their dominant part), nor in their Γ_1 -values. Samples ball-milled together with catalyst exhibited changes in both spectra and the Γ_1 -values as a function of temperature. A quantitative analysis of hydrogen dynamics in $NaAlH_4$ itself could be hampered by the fact that the sample decomposes into Na_3AlH_6 (see Eq. 1.1). The changes in the spectra as a function of temperature of catalyzed samples were up to a well defined and limited grade reversible. Therefore, it was proved that the observed narrowing of the lines of catalyzed samples can be ascribed to the motion of the protons within the sample. In order to further determine the dynamical process occurring in $NaAlH_4$, the spin-lattice relaxation rates as a function of temperature were also measured. The high-temperature region of the samples with catalyst is characterized by a process of high activation energy which could be ascribed to the same phenomena causing the observed narrowing of the line. The low-temperature region, as well as the whole measured temperature region of the sample without catalyst exhibit a coupling of the whole spin system via spin diffusion.

Section 5.4 deals with the structure of $NaAlH_4$ ball-milled with $Ti_{13}\cdot 6THF$ catalyst. The dipolar second moment (M_2) of the measured proton NMR spectrum of $NaAlH_4$ is compared with the

M_2 values calculated on the basis of structural information reported in the literature as in Ref. [26]. Furthermore, we determined experimentally the hetero- and homonuclear contributions to M_2 separately. These two contributions were obtained by studying, in addition to the FID, the ME amplitude as a function of the spin evolution time.

5.1 NMR spectra

The proton NMR spectra were obtained by applying the Fourier transform to the time domain signal, i.e., the FID or the second half of the MHE¹.

5.1.1 Spectra of $NaAlH_4$, Na_3AlH_6 , and NaH at room temperature

At room temperature a clear difference exists between the spectra obtained on $NaAlH_4$, on Na_3AlH_6 , and NaH (the products formed after the H-desorption). This difference can be seen in Figure 5.1.

Spectrum of NaH .

The bottom part of Figure 5.1 presents the room temperature spectrum of NaH . This spectrum was taken after a dead time of 20 μs , and consists of a very narrow central line superimposed on a wide line with a half-width of about 35 kHz.

Spectrum of Na_3AlH_6

The central part of Figure 5.1 presents the spectrum of Na_3AlH_6 . This spectrum was taken with an experimental dead time of 10 μs , and consists of a broad single line with a half-width of 20 kHz.

Spectrum of $NaAlH_4$

Finally, the upper part of Figure 5.1 shows the spectrum of $NaAlH_4$. This spectrum, measured with a dead time of 10 μs , consists of a doublet structure with a splitting of about 50 kHz. The minimal dead time of our set-up (the 67.7 MHz spectrometer) was 6 μs , but for most of the first measurements we chose a dead time of 10 μs . This was done to ensure that our NMR-signal was not affected by dead time effects. Unfortunately, the FID of $NaAlH_4$ decays only after about 23 μs , i.e., we were cutting in these first measurements almost a half of the NMR signal.

In order to explain the doublet found in the spectra of $NaAlH_4$, we measured the spectrum using a 300 MHz spectrometer. The NMR spectra are not influenced by the measuring frequency with the exception of the S/N ratio, which should be better for a 300 MHz spectrometer than for a 67.7 MHz one (according to Eq. 4.1). The shortest experimental dead time which could be achieved using the 300 MHz spectrometer was 3 μs . With that dead time, the spectra did not present any doublet (see Figure 5.2). Thus, too long dead

¹As we know from Section 2.5, the second half of an echo can be considered as a “FID” recorded without dead time.

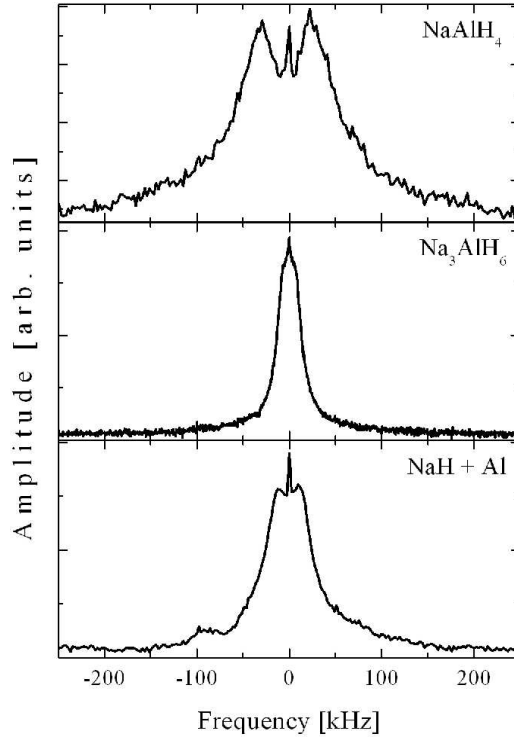


Figure 5.1: Room temperature ^1H -NMR spectra of NaAlH_4 (with $10 \mu\text{s}$ dead time), Na_3AlH_6 (with $10 \mu\text{s}$ dead time), and $\text{NaH} + \text{Al}$ (with $20 \mu\text{s}$ dead time [50], [8]).

times generated the doublet found in the spectra which were measured before. The same effect had been previously found on YH_3 [80], [81], [82].

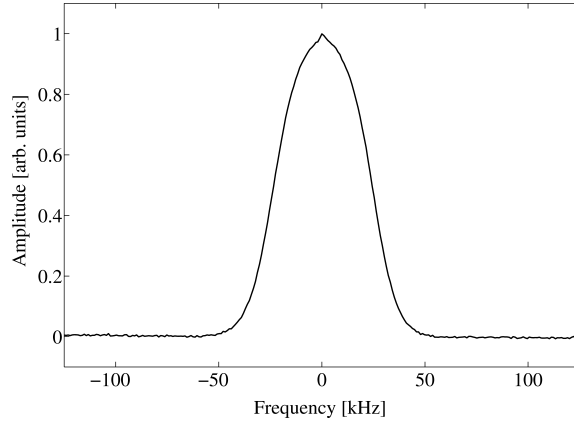


Figure 5.2: Room temperature spectrum of an untreated sample of NaAlH_4 obtained after a $\pi/2$ -pulse, with a dead time of $3 \mu\text{s}$.

The spectra obtained with longer dead times proved to be very useful to distinguish between the room temperature spectra of NaAlH_4 and Na_3AlH_6 as the differences between both spectra became even more evident (see again Figure 5.1).

In the case of Na_3AlH_6 , the length of the FID (about $80 \mu\text{s}$) was significantly larger than typical values of the dead time (about $6 \mu\text{s}$). Therefore, no significant differences in the

spectra of Na_3AlH_6 with and without dead time were expected.

The absence of the spike-like central line in the $NaAlH_4$ spectrum measured at 300 MHz can be explained by the used experimental resolution. In the measurements at 300 MHz we used a resolution of 1 μ s per point, whereas in the measurements done at 67.7 MHz (including those made in Ref. [8]), we used resolutions of 0.4 or even 0.2 μ s per point.

Effect of impurities The common feature of the spectra of $NaAlH_4$ is the existence of a narrow central line, which accounts for only a small percentage of the total intensity of each spectrum.

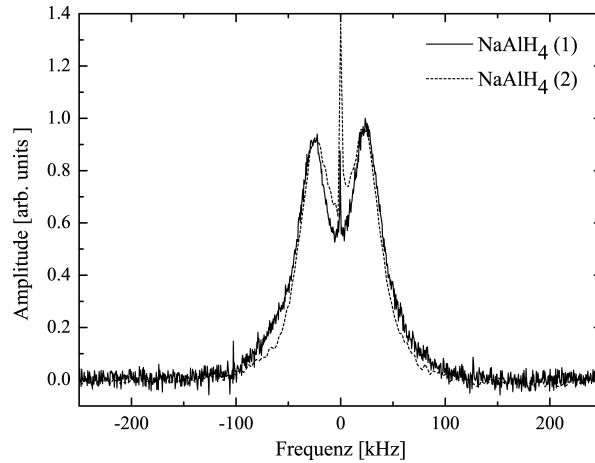


Figure 5.3: Spectra of two samples of $NaAlH_4$. The spectrum of $NaAlH_4(1)$ has the smallest central peak and a better purification quality [8].

In Figure 5.3, we compare the spectra obtained on two different samples of $NaAlH_4$, with different purification quality [8]. The spectrum with the smallest central peak was measured on the most carefully purified sample ($NaAlH_4(1)$ in Figure 5.3). Hence, the central line can be attributed to impurities or remaining solvent from the purification process (see Section 4.1).

On the next sections we will see that when the sample contains a catalyst, a central peak is also found. However, this peak is wider than the one obtained due to impurities and it is presumably related to the small part of the sample, which had already decomposed into Na_3AlH_6 [36], [83].

5.1.2 Rigid lattice NMR spectra of $NaAlH_4$

At low temperatures the movement of the atoms is frozen on the spectral NMR timescale (explained on Sect. 2.11) and effects like motional narrowing can be neglected. The observed spectrum is the so-called “rigid lattice spectrum”.

Untreated samples of $NaAlH_4$

An untreated sample is understood as a sample obtained without being ball-milled afterwards or without any kind of catalyst added (see Section 4.1).

The spectra measured at 130 K and at room temperature, both with 10 μ s dead time (using the 67.7 MHz Spectrometer) on an untreated $NaAlH_4$ sample are shown in Figure 5.4. Both spectra have a very similar structure: a doublet with a splitting of about 50 kHz. The only difference is that the central line disappears at 130 K. The disappearance of the central line can be explained by a strong broadening of it, as the temperature drops from room temperature to 130 K. In the spectrum found at room temperature, the central line has already been attributed to residual solvent or to impurities within the sample. Hence, the reason for the broadening of the line could be a freezing of the hydrogen motion in the remaining solvent or in the vicinity of impurities.

Disregarding the central peak, there is no difference between the spectra obtained at room temperature and at 130 K (see Figure 5.4). Therefore, for this part of the spectrum the rigid lattice condition is fulfilled already at room temperature.

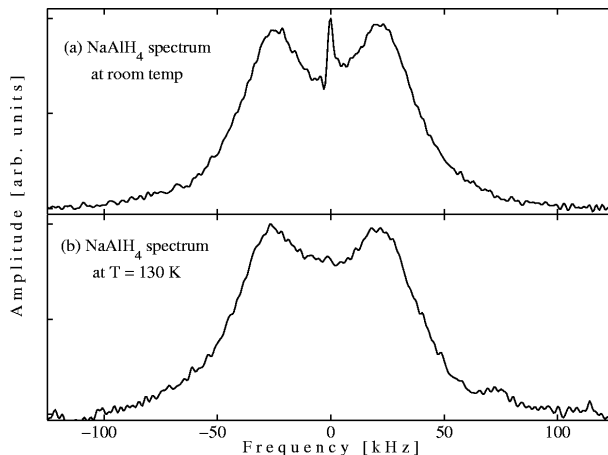


Figure 5.4: NMR spectra of untreated $NaAlH_4$, measured with a dead time of 10 μ s, at room temperature (a) and at 130 K (b).

The upper part of Figure 5.5 presents the time signal of the MHE. This signal (the second half of the MHE) can be considered as a “FID” recorded without dead time. The graph shows that the magnetization does not simply decay to zero with time but oscillates slightly (even though the measurement was on resonance). This oscillation is known as Lowe-like beat, as it was first reported by I. J. Lowe [84] and it has also been observed in the case of YH_3 [80]. This beat was found in the rigid lattice regime by direct quantum calculation of the FID using the dipolar interactions [74]. Typically, the Gaussian approximation (explained on Section 2.9.3) assumes that the dipolar interactions between the nuclei in a solid will produce a Gaussian distribution of magnetic fields and thus gives rise to a Gaussian decay of the FID.

The middle part of Figure 5.5 presents the experimental spectrum without dead time, obtained by Fourier transform of the second half of the MHE taken with the 300 MHz spectrometer. The spectrum consists of a single peak, which deviates from a pure Gaussian form, with a FWHM of 48 ± 1 kHz.

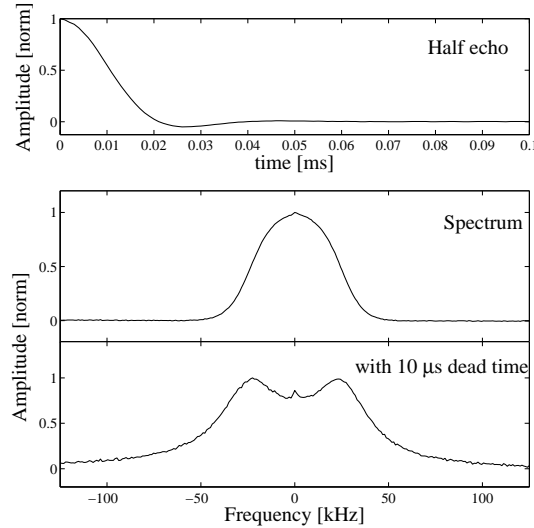


Figure 5.5: Measurements performed at room temperature on an untreated sample of NaAlH_4 .
 (Top) Half of the MHE. (Down) Corresponding spectra without and with $10 \mu\text{s}$ dead time.

In order to determine whether the rigid lattice condition has been fulfilled, it is necessary to verify whether the same spectrum is obtained at lower temperatures. The measurements with the 67.7 MHz spectrometer, as discussed above, already indicate that the rigid lattice condition is valid at room temperature. The measurements at 300 MHz give further support to this conclusion because the room temperature spectrum shown at the bottom of Figure 5.5 (obtained emulating an artificial dead time before doing the Fourier transform of the FID) is very similar to the spectrum obtained at 130 K with the 67.7 MHz spectrometer (shown in Figure 5.4). The only real difference is the absence of the spike-like central peak. This can also be explained from the used experimental resolution. In the measurements at 300 MHz we used a resolution of $1 \mu\text{s}$ per point, whereas at 67.7 MHz, we used resolutions of 0.4 or even $0.2 \mu\text{s}$ per point.

Samples of NaAlH_4 ball-milled together with catalyst

Milling the NaAlH_4 powder together with catalyst, reduces the temperature at which the hydrogen atoms desorb (see Sect. 1.4.1). In catalyzed samples the T_1 -values (where $T_1 = 1/\Gamma_1$) are much shorter than in untreated samples, reducing the measuring times to few minutes. Therefore it is faster to measure on catalyzed samples at low temperatures than in samples without catalyst. The sample ball-milled for 30 minutes with 2 mole % $\text{Ti}_{13} \cdot 6\text{THF}$ catalyst will be referred to as 2 mole % sample.

Figure 5.6 shows the second half of the MHE, and the spectra obtained from the echo without and with an artificial dead time obtained on the first 2 mole % sample. Similar to the untreated sample, the echo shows a Lowe beat. The spectrum has a FWHM of $49 \pm 1 \text{ kHz}$ and it is not purely Gaussian.

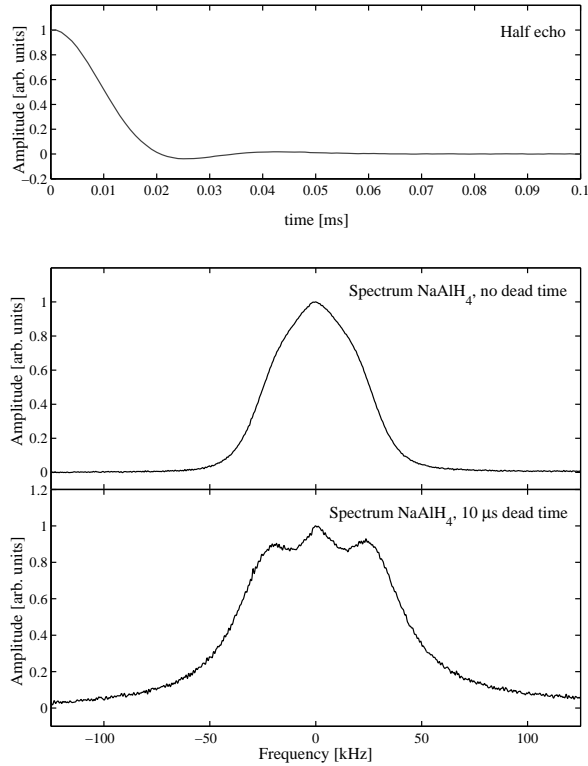


Figure 5.6: NMR-Measurement done at 215 K in the 2 mole % sample. (Top) Second half of the MHE. (Down) Corresponding spectrum without and with a dead time of $10 \mu\text{s}$.

The bottom part of Figure 5.6 presents the doublet found when an artificial dead time of $10 \mu\text{s}$ is cut from the second half of the MHE. The central peak in that spectrum could be due to the peak resulting from impurities, which is wider at 215 K than the one observed at 300 K as shown in Figure 5.3. However, the peak due to impurities contributes at most with 5 % to the spectra shown in Figure 5.3, whereas the central peak in Figure 5.6 represents about 25 % of the spectra. Due to the use of catalyst, on the other hand, it is known that a small part of the sample has already decomposed during the milling process into its secondary product Na_3AlH_6 [36], [83]. As hydrogen in that material has a much higher mobility [8], the linewidth is reduced in comparison to NaAlH_4 . The spectrum of pure Na_3AlH_6 at 225 K with a dead time of $10 \mu\text{s}$ is shown in Ref. [8]. That spectrum consists of a central peak with a width of about 10 kHz possessing two shoulders plus a small spike-like line. Although no such spike-like line has been observed in the spectrum at the bottom of Figure 5.6, the central peak is attributed to Na_3AlH_6 because of its coincident width of about 10 kHz (which agrees with the found in Na_3AlH_6). The absence of the spike-like line may be explained by the resolution of the measurements. While in the present measurements we used a resolution of $1 \mu\text{s}$ per point, in Ref. [8] 0.4 or even $0.2 \mu\text{s}$ per point was used. The wide part of the spectrum with a width of about 50 kHz observed in our measurements is attributed to NaAlH_4 .

In Figure 5.7 the just discussed spectrum obtained at 215 K is shown, together with the one obtained at room temperature. Both spectra were generated by Fourier transforming the second

half of a MHE corresponding to a FID without dead time. The two spectra are similar except for an extra central peak observed for the room temperature spectrum. As in the Figure 5.6, the extra peak at room temperature should be related to the part of the sample which has already decomposed into Na_3AlH_6 . The spectrum at room temperature shown in Figure 5.7 consists of a narrow line and a broad main line. The central line is composed of a spike like line and a wider line with a width about 20 kHz. The spectrum of Na_3AlH_6 at room temperature is composed of a line with a FWHM of 19 kHz plus a spike-like line [8], too. Therefore, the narrow central peak is attributed to Na_3AlH_6 .

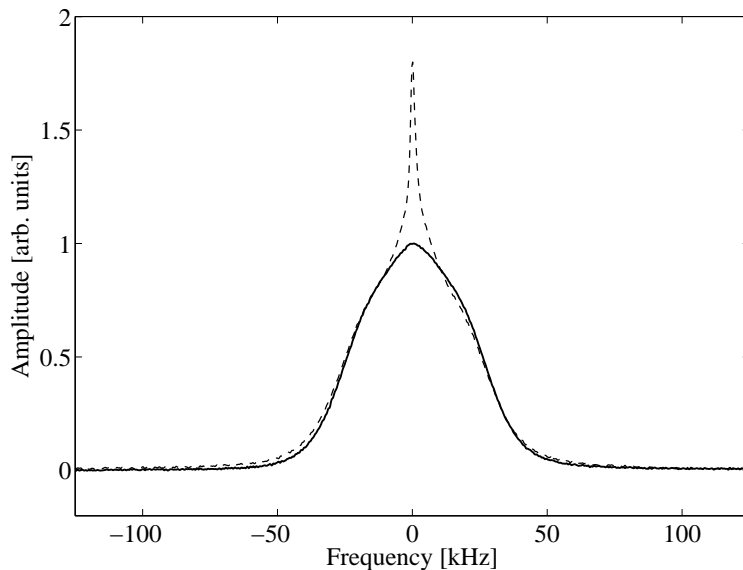


Figure 5.7: Spectra of the 2 mole % sample at 215 K (solid line) and at room temperature (dashed line). Both spectra were obtained from the second half of a Magic-Hahn echo, i.e. they have no dead time.

Gaussian approximation

After the first $23 \mu s$ most of the magnetization has already decayed to zero in the FID and only the Lowe beat can be clearly seen. Truncating the FID signal after the first $23 \mu s$, one neglects the Lowe beat. Furthermore, in case of the samples ball-milled together with catalyst one effectively neglects the traces of Na_3AlH_6 by truncating the FID².

The spectra obtained from the truncated time signal measured on the untreated $NaAlH_4$ sample at room temperature, as well as on the treated sample (the 2 mole % sample) at 215 K and at room temperature are shown in Figure 5.8. The spectra overlap each other and become an almost perfect Gaussian with a linewidth of 44.5 kHz. Therewith we can conclude that

- the deviation from the purely Gaussian form is due to the Lowe-beat;
- even for catalyzed samples, the rigid lattice condition is already fulfilled at room temperature;

²As we already said, the FID of Na_3AlH_6 decays slower, i.e., its FID has a long tail.

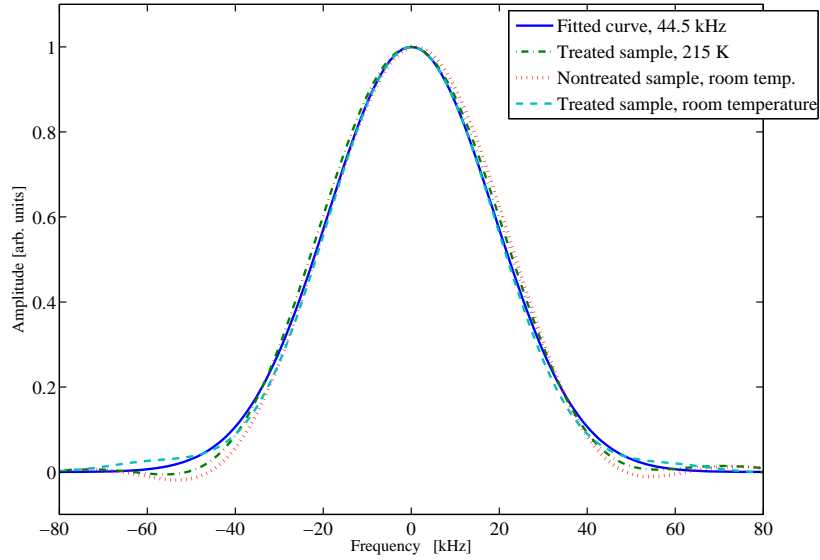


Figure 5.8: Spectra of NaAlH_4 after truncating the FID after the first $23 \mu\text{s}$. All spectra were obtained from the second half of a Magic-Hahn echo, i.e. without dead time.

- catalyzing the sample does not influence the spectra in the rigid lattice limit.

We are unfortunately not sure to have measured exactly in the center of the echoes. The linewidth of the spectra is influenced by the dead time, also if it is negative (if one record the FID-like signal not in the center of the echo but before). Such a dead time of $-1 \mu\text{s}$ reduced the obtained linewidth to 42 kHz. We therefore cannot conclude anything about the obtained linewidths and its corresponding second moment. A method to avoid this problem is by using the decay of the echo signal itself to obtain the corresponding decay. This method will be used in section 5.4 to obtain the second moment of the samples ball-milled with and without catalyst.

The correlation coefficients³ of the fittings were quite good, i.e., $R^2 = 0.9977$, 0.9988 , and 0.9986 for the untreated, the one treated at room temperature and at 215 K, respectively. However in the spectra in Figure 5.8 small side-lobes can be observed. These can be explained by the abrupt truncation of the FID. In order to remove the side lobes, one could multiply the FID with a function that decreases with the time (apodization). However, we do not do it because first the side-lobes are so small and second, because thereby one could introduce an extra undesired broadening in the spectra [86], [87]. It is undesired because then we cannot compare this linewidth with theoretical values obtained using the van Vleck formulae (the Gaussian approximation).

³The correlation coefficient is a statistical measure which gives the goodness of a fit or how well a regression approximates the real data points. An R^2 equal to 1 indicates a perfect fit regression [85].

5.2 NMR studies of hydrogen dynamics in $NaAlH_4$

In order to accelerate the ab- and desorption process, one usually treats the sample by ball-milling and/or using catalyst. By ball milling, one expects that the grain size decreases and the surface area increases. In addition, more defects are introduced into the samples. All these treatments speed up the hydrogen desorption [9]. In $NaAlH_4$ besides milling we use catalyst, which accelerates the hydrogen desorption process even more and makes it also reversible. The present NMR studies are performed to get a better understanding of the microscopic mechanisms involved in the hydrogen desorption process. Furthermore, we search for hints of why in samples milled with catalyst one has reversibility in the hydrogen desorption process but not in samples which are just ball-milled.

Details of the sample preparation as well as of the measurements are given in Chapter 4. The details of all samples and measurements done in this section are summarized in the tables 4.2 and 4.3.

5.2.1 Hydrogen dynamics and the NMR spectra

Ball-milled samples without catalyst

In this section we present NMR-spectra measured at various temperatures on $NaAlH_4$ samples which do not contain catalyst but are milled for 5 minutes and 12 hours, respectively. Additional measurements were performed on a sample ball-milled for 30 minutes. The results obtained for the last mentioned sample are identical to those obtained on the sample ball-milled for 5 minutes only. For that reason they are not presented explicitly.

In Figure 5.9 the spectrum obtained on an untreated sample is shown together with the one measured on a sample ball-milled for 5 minutes. Both spectra were taken with a dead time of $6 \mu s$. Only a small difference is observed between both spectra. The signal-to-noise ratio (S/N) is better for the untreated sample, as this spectrum was measured at 300 MHz (see Eq. 4.1). The similarity of the two spectra indicates that no big changes in the structure of the material are induced by the ball milling treatment.

In Figure 5.10 the spectra of the $NaAlH_4$ sample milled for 5 minutes are shown at various temperatures. A small and narrow central peak observed at 299 K becomes more and more pronounced as the temperature is increased up to 384 K. The dominant wide part of the spectra remains practically the same at all investigated temperatures. One can assume

that these two contributions to the spectra are attributed to different regions of the sample with e.g., different structures and compositions. From the temperature dependence of the broad and dominant contribution, one can conclude that on the spectral NMR timescale (explained on Sect. 2.11) no hydrogen motion occurs in most parts of the $NaAlH_4$ sample.

The initial and the final spectra obtained at about 298 K before and after a complete temperature cycle are shown Figure 5.11. The spectral weight of the final spectrum decreased by about 10 % in comparison to that of the initial spectrum. This implies that the hydrogen content decreased by about 10 %. Remembering that $3NaAlH_4 \leftrightarrow Na_3AlH_6 + 2Al + 3H_2 \uparrow$, thus 20 % of the

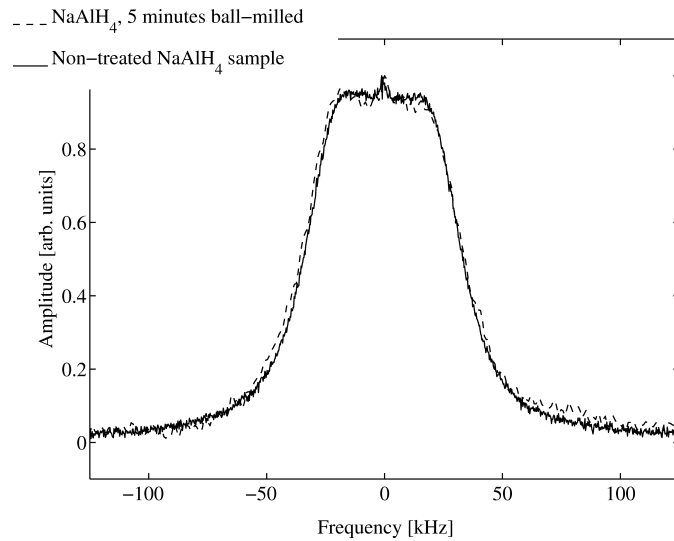


Figure 5.9: ^1H -NMR spectra with $6 \mu\text{s}$ dead time on a $NaAlH_4$ sample ball-milled for 5 minutes and on an untreated sample.

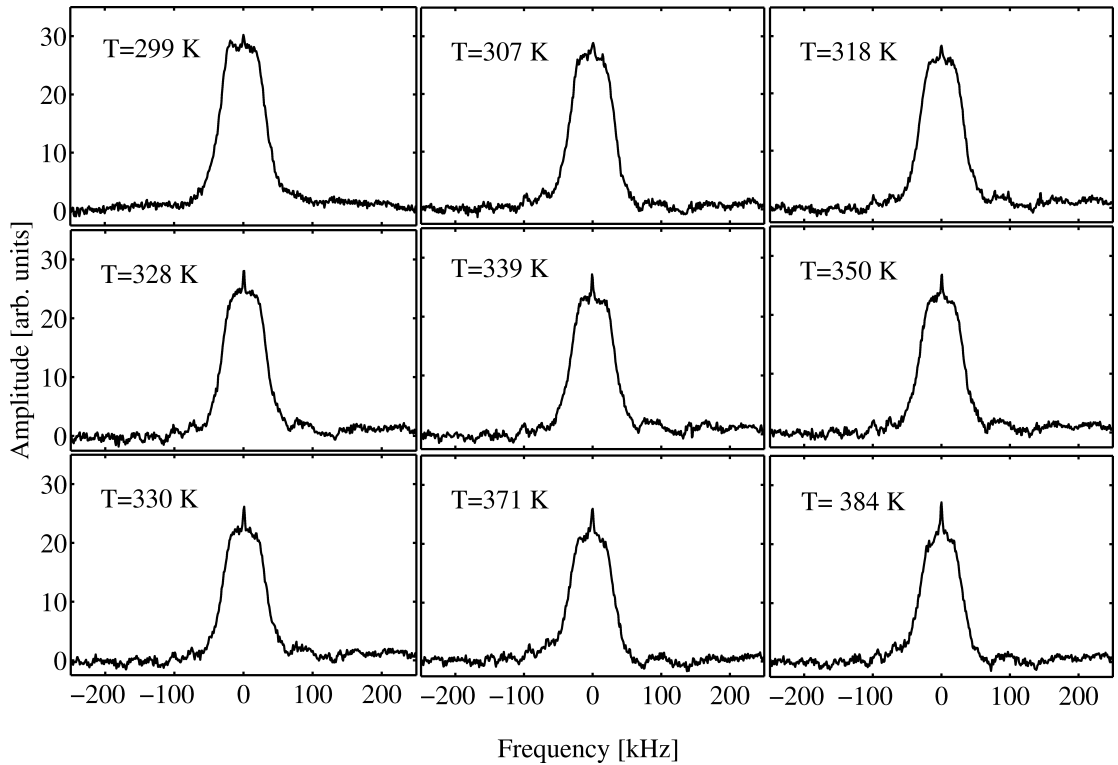


Figure 5.10: ^1H -NMR spectra obtained at different temperatures with $6 \mu\text{s}$ dead time in a $NaAlH_4$ sample ball-milled for 5 minutes.

sample $NaAlH_4$ decomposed into Na_3AlH_6 . In the final spectrum then only 10 % of the signal is representative of Na_3AlH_6 .

The worsening of the signal-to-noise ratio after the temperature cycle (see Figure 5.11) may be due to a detuning of the probe (r.f. circuit). A poorly tuned probe does not affect the resolution,

however the signal-to-noise will be worse. This was often caused by an abrupt temperature change (from 384 K to room temperature).

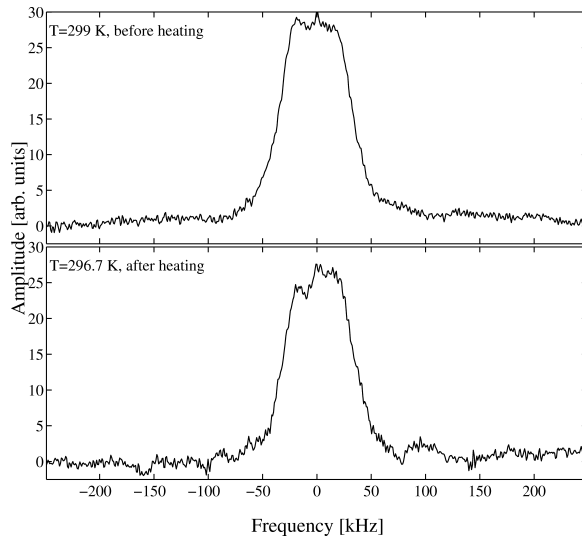


Figure 5.11: ^1H -NMR spectra obtained at room temperatures before and after the measurements in the NaAlH_4 sample ball-milled for 5 minutes.

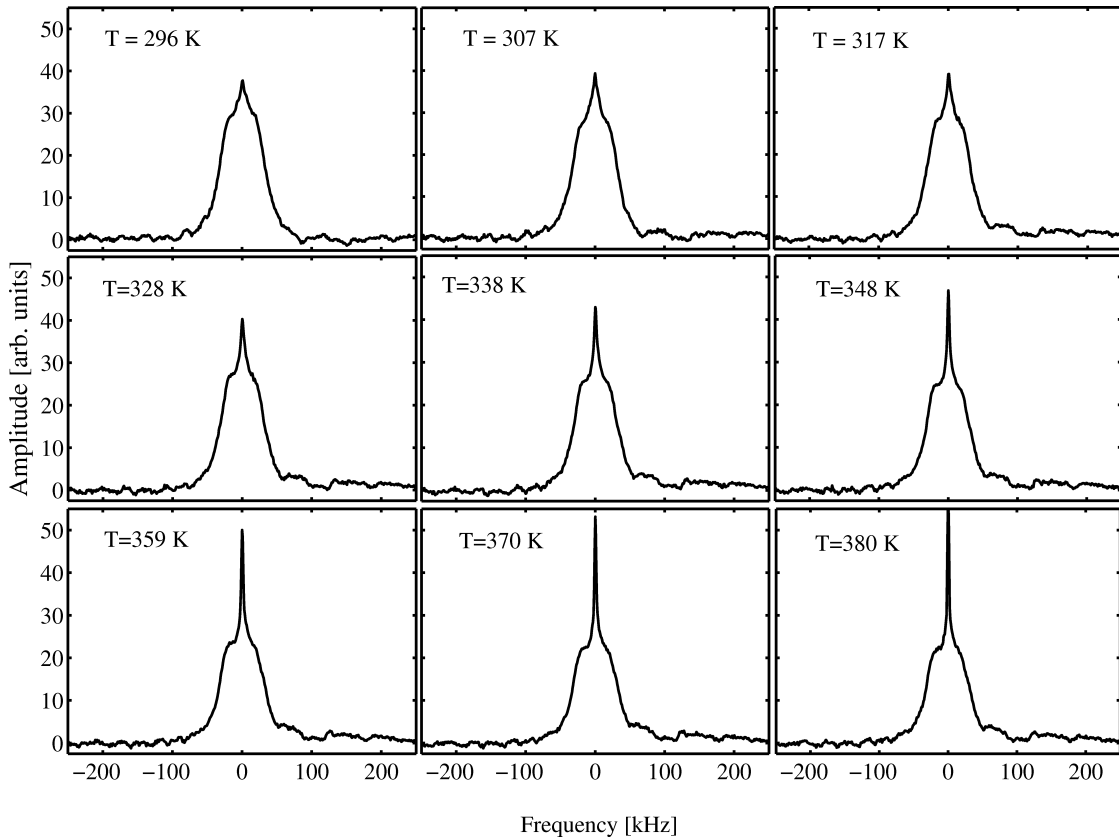


Figure 5.12: ^1H -NMR spectra measured at different temperatures with $6 \mu\text{s}$ dead time in a ball-milled for 12 hours NaAlH_4 sample.

The spectra measured on the $NaAlH_4$ samples milled for 12 hours are shown in Figure 5.12 at diverse temperatures. As in the case of the sample ball-milled for 5 minutes, the temperature was increased step by step from measurement to measurement from room temperature up to 380 K until finally in a single step the temperature was reduced to room temperature. The linewidth of the wider peak remains constant, as in the samples milled for 5 and 30 minutes. Like in the sample ball-milled for only 5 minutes a narrow central peak is observed, however, this peak is more pronounced and above 317 K suffers a decrease of its linewidth. The spectral weight of the central peak (in the spectra of the sample ball-milled for 12 hours) is of about 10 %. Therefore, 20 % of the sample has decomposed into Na_3AlH_6 during the 12 hours that the milling process took.

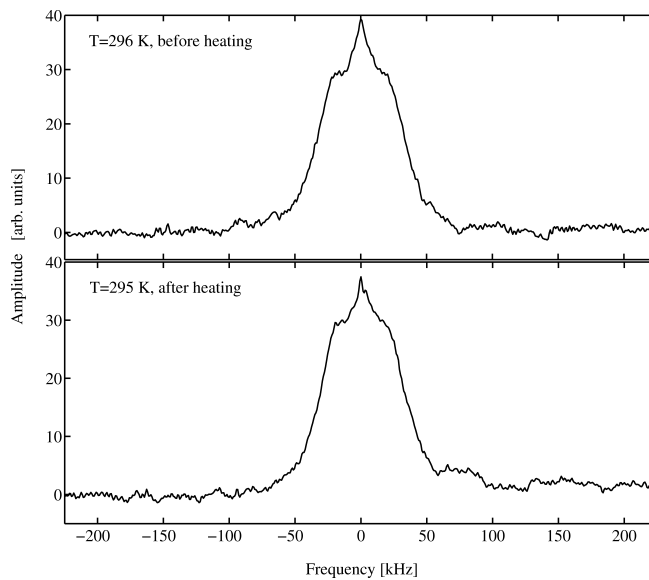


Figure 5.13: Reversibility of the spectra: Initial and final spectra of sample milled for 12 hours.

In Figure 5.13 the initial and final spectra of the cycles of measurements (both at room temperature) are shown. The linewidths of the spectra at room temperature observed on the sample before and after heating are identical. Although altogether the measurements done on the sample ball-milled for 12 hours took about 24 hours, one finds that the difference in the spectral weight of the spectra is minimal. The comparison of the spectra measured before and after the completion of a temperature cycle (shown in Figure 5.13) indicates that less than 5 % of hydrogen content gets lost during the measurements.

Similar to the sample with 5 minutes ball-milled, the signal-to-noise ratio of the spectra decreased. This again speaks for a detuning of the NMR-probe.

Interpretation

In the course of ball-milling one cannot avoid that in addition to the mechanical effects of the milling process, a warming up of the sample takes place. Specially the $NaAlH_4$ sample milled for 12 hours may therefore have already partially decomposed into Na_3AlH_6 during the ball milling. In order to see which of the features in the spectra discussed above are related to $NaAlH_4$ and which to Na_3AlH_6 , we describe shortly the essential features of 1H -NMR spectra measured on Na_3AlH_6 .

powder samples reported in Ref. [8]. At room temperature the spectrum of Na_3AlH_6 is composed of a dominant line with a width of about 19 kHz. On top of that line in its center a small crest is superimposed [8]. The dominant line remains essentially the same between room temperature and 390 K. The crest on the other hand becomes higher as the temperature is increased and eventually develops into a spike-like line (at 380 K the spike-like line can clearly be seen). The behavior of the central peak in Figs. 5.10 and 5.12 resembles very much these changes with temperature found on Na_3AlH_6 . Therefore, the central peak observed on our $NaAlH_4$ samples is attributed to a fraction of Na_3AlH_6 present in the sample. Specifically, the spectral weight of the central peak is of about 10 %, so 20 % of the sample has decomposed into Na_3AlH_6 during the 12 hours that the milling process took.

The comparison of the spectra measured before and after the completion of a temperature cycle show that only 10 % or 5 % of hydrogen content gets lost during the measurements in the sample ball-milled for 5 minutes or 12 hours, respectively. This implies that most of the Na_3AlH_6 observed was produced prior to the first measurement, i.e., during the ball-milling process itself. This holds in particular in the sample ball-milled for 12 hours. The linewidth of the spectra at room temperature observed on the samples before and after completion of a heating cycle are identical. Thus, the observed changes in the spectra with temperature (Figs. 5.10 and 5.12) are mainly reversible.

Samples ball-milled together with catalyst

Similar measurements were done on $NaAlH_4$ samples ball-milled for 30 minutes together with 1, 2, and 5 mole % $Ti_{13} \cdot 6THF$ catalyst. For simplicity we call these samples in the following 1, 2, or 5 mole % sample. The sequences of spectra obtained with 6 μs dead time, measured as a function of temperature on the 1 and 5 mole % samples are shown in Figure 5.14.

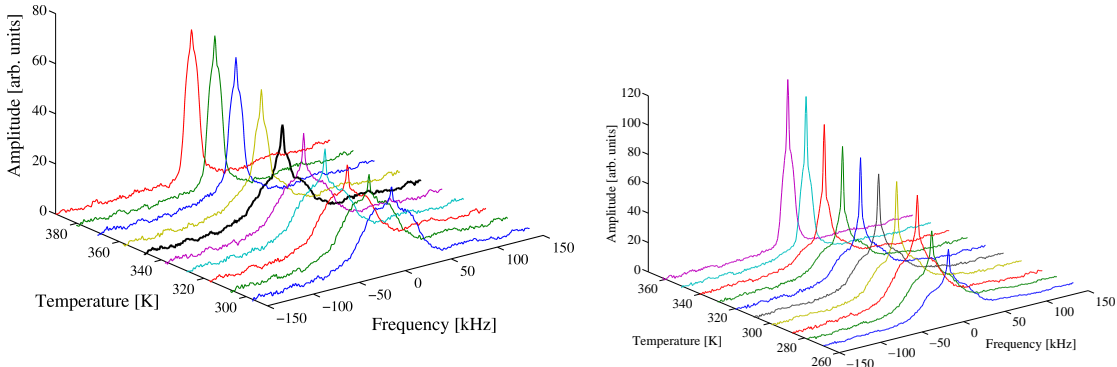


Figure 5.14: Sequence of spectra with 6 μs dead time of 1 (on the left) and 5 mole % sample (on the right) as a function temperature.

Each spectrum in Figure 5.14 is composed of a wider dominant line (wider than 17 kHz) plus a spike-like central line with small spectral weight. In samples ball-milled together with catalyst it is known that a small part of the sample may have already decomposed during the milling process

into its secondary product Na_3AlH_6 [36], [83]. The spectrum of Na_3AlH_6 powder samples at room temperature is composed of a main line with a linewidth of 19 kHz, on which a small spike-like line is superimposed. The wide line (with about 60 kHz linewidth at room temperature) must be therefore attributed to $NaAlH_4$. The spike-line line is attributed to Na_3AlH_6 . The broad component of the Na_3AlH_6 spectrum is presumably hidden below the dominant $NaAlH_4$ contribution. The spike-like lines found in Figure 5.14 are more pronounced than those of the samples without catalyst (see Figure 5.10 and Figure 5.7). This finding may be explained assuming that a larger part of the catalyzed sample already decomposed into Na_3AlH_6 than in samples not containing catalyst.

The linewidth of the dominant line in the spectra decreases with increasing temperature. The spike-like line, specially in the spectra measured on the 5 mole % sample (see Figure 5.14), becomes higher as the temperature is increased. From Ref. [8], we know that the linewidths of the main line of the Na_3AlH_6 spectra decreases from 19 kHz to about 17 kHz by increasing the temperature to 380 K. The change of the spike-like central line as a function of temperature is much more pronounced [8]. Its intensity increases by increasing the temperature similar to the central spike-like line of the spectrum shown in Figure 5.14. This is in accordance with the interpretation given above that the spike-like central peak is due to those parts of the sample which have already decomposed into Na_3AlH_6 . The question is only if the apparent narrowing of the wide line (seen in Figure 5.14) is due to the decomposition of $NaAlH_4$ into Na_3AlH_6 during the measurement, or due to a motional induced narrowing of a line always representing $NaAlH_4$. To answer this question requires special care because the width of the wide line at higher temperature is almost identical to the linewidth of Na_3AlH_6 at these temperatures.

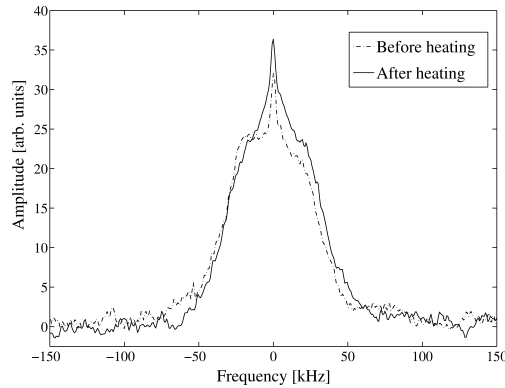


Figure 5.15: Spectra before and after heating the 1 mole % sample.

In order to check whether a decomposition of the sample occurred during the measurements, a control measurement was performed at room temperature after finishing all the measurements on the 1 mole % sample. Even though the measurement lasted about two measure days, the only real change between the spectra before and after heating (shown in Figure 5.15) is that the central line gets wider in the spectra after the cycle. These central narrow peaks are the signature of Na_3AlH_6 . The spectral weight of the central peak increased from about 5 % to 15 %. Therefore, about 10 % of the sample decomposed into Na_3AlH_6 presumably during the sample preparation and 20 % during the measurements. The observed changes of the linewidths with temperature were nevertheless mainly reversible, as not more than 10 % of $NaAlH_4$ present in the sample at the

beginning of the measurements transformed into Na_3AlH_6 . Therefore, the narrowing of the lines with increasing temperature in Figure 5.14, can be ascribed to a motion of the protons within the sample. The motional narrowing of the wide line in the spectra has to be attributed to the motion of protons within $NaAlH_4$. Motion of protons in Na_3AlH_6 cannot contribute to the change of the width of this line because in the spectra of Na_3AlH_6 only the spike-like line is strongly affected by temperature changes in the relevant temperature regime whereas the linewidth of the broader component remains nearly constant between 19 (at room temperature) and 17 kHz (at 380 K).

Quantitative analysis of the spectra

In order to obtain quantitative information the spectra were fitted to a superposition of two or three lines. Each line in these fits is described by a weighted sum of a Gaussian (G_ω), plus a Lorentzian curve (L_ω) as

$$F_\omega = \varsigma L_\omega + (1 - \varsigma) G_\omega \quad (5.1)$$

$$= A \left(\varsigma / \left(1 + \left(\frac{\nu - \nu_0}{1/2 \Delta\nu} \right)^2 \right) + (1 - \varsigma) \exp \left(- \left(\frac{\nu - \nu_0}{1/(2 * \sqrt{\ln 2}) \Delta\nu} \right)^2 \right) \right) \quad (5.2)$$

where both curves have a common amplitude (A), the same origin (ν_0) and the same linewidth ($\Delta\nu$). The Lorentzian fraction is described by ς . For $\varsigma = 0$, one obtains a purely Gaussian, while for $\varsigma = 1$, we obtain a pure Lorentzian curve. For a combination of a Gaussian and Lorentzian in Eqs. (5.1) and (5.2), ς is a fraction of one and we use the linewidth of both curves (without any kind of recalculation of the full fitted line). The fittings were done with the help of the program matNMR [79].

Two-component fits

In these fits we use a superposition of 2 lines, one representing the narrow spike-like line and the other one representing the dominant broader line. The narrow spike-like line was supposed to be a Lorentzian with constant linewidth of 3 kHz for all temperatures. The broad line, on the other hand, did fit well to a Gaussian in most of the measured temperature range. At intermediate temperatures combinations of a Gaussian and Lorentzian generate better fittings.

Relative spectral weight of the two components

The spectral weight is defined as the normalized area under the lines, which are fitted to the experimental spectra. The normalization was done dividing by the sum of both areas. The spectral weights of each fitted line are plotted in Figure 5.16 as function of $1000/T$.

In Figure 5.16 the narrow central line observed on the 1 and 2 mole % sample represent for all temperatures less than 10 % of the spectra. In the 5 mole % sample, the narrow line represents up to 15 % at the highest temperatures. This probably implies that in the 5 mole % sample a bigger fraction decomposed into Na_3AlH_6 during the sample preparation than in the sample with low content of catalyst.

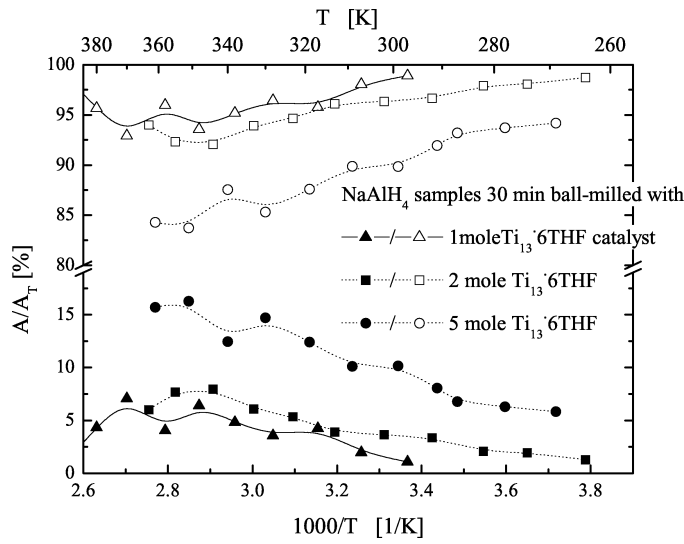


Figure 5.16: Percentaged spectral weights as a function of $1000/T$. The empty and full symbols represent the wide and the narrow component, respectively.

The decomposition of the spectra into a spike-like line (with a width of 3 kHz) and a broad line does not correspond to a separation into contributions from regions of the sample consisting of Na_3AlH_6 and NaAlH_4 . The spectra of Na_3AlH_6 has a wide component, whose linewidth varies between 19 kHz at room temperature and 17 kHz at 380 K. This component is subsumed in the broad line.

Linewidth of the wide component as a function of temperature

We use the linewidth of the wide curves to obtain more information on the hydrogen motion in NaAlH_4 as a function of temperature. This part of the spectra mainly represents catalyzed NaAlH_4 , even though a small contribution is expected to come also from Na_3AlH_6 .

In Figure 5.17 the linewidths of the fitted wide peaks as a function of temperature of the 1, 2, and 5 mole % sample are presented. In all samples one can see a plateau at low temperatures with large linewidths, a second plateau at high temperatures with small linewidths (with exception of the 2 mole % sample) and a region in between both. These regions are in detail explained next:

Plateau at low temperature.

The spectra in this temperature interval could be well fitted to an almost perfect Gaussian, with linewidths of about 60 kHz. These linewidths are identical with those of the spectra of the untreated sample, both with 6 μs dead time (see Fig 5.10). In the plateau region at low temperature in Figure 5.17 the rigid lattice condition for the spectra is fulfilled.

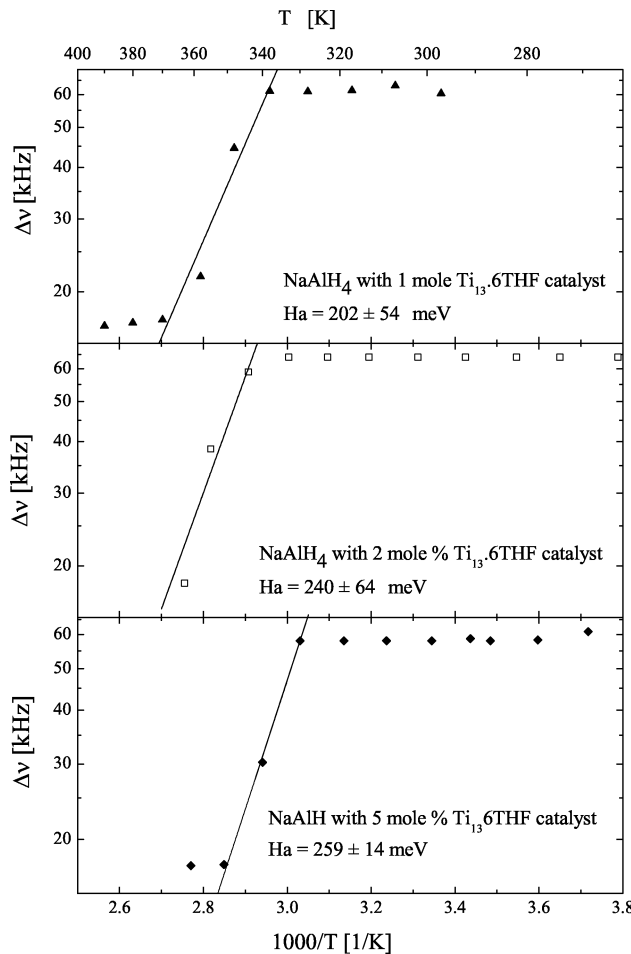


Figure 5.17: Linewidth of the main part of the spectra (wide line) as function of $1000/T$ in the 1, 2, and 5 mole % sample.

Plateaus at high temperature.

For the 1 and 5 mole % samples, the graphs for the linewidth $\Delta\nu$ as a function of $1000/T$ (see Figure 5.17) show another plateau at higher temperatures⁴. In the temperature regime corresponding to this plateau the broad line can be fitted to a Gaussian, with a linewidth of about 17 kHz. A similar high temperature plateau in the linewidth was found in Ref. [49] for Na_3AlH_6 . This incomplete motional narrowing was in that case ascribed to the thermally activated rotation of the AlH_6 octahedra in Na_3AlH_6 about their C_4 symmetry axis. Those rotations of the $[\text{AlH}_6]$ -octahedra cause a partial averaging and thus lead to a reduced width of the field distribution felt by a proton [74].

In order to investigate whether these ideas may be transferable to NaAlH_4 calculations of second moments partially averaged due to the rotation of the $[\text{AlH}_4]$ -tetrahedra about certain axes were performed, as explained in Section 2.9.2. In table 5.1 these calculated reduced second moments of NaAlH_4 are presented.

⁴In the 2 mole % sample shown, the second plateau cannot be seen as we did not measure at so high temperatures (the highest temperature was 363 K).

$NaAlH_4$		
Rotating around:	C_2	C_3
$M_2 [G^2]$	0.38	3.04
Linewidth [kHz]	6.2	17.5

Table 5.1: $M_{2,R}$ of $NaAlH_4$ due to fast rotation of the AlH_4 tetrahedra around the C_2 and C_3 axis.

According to Table 5.1, the linewidth of the 1H -NMR spectra would decrease to 6.2 and 17.5 kHz if the **tetrahedra** rotate around their twofold symmetry axis (C_2) and around their threefold symmetry axis (C_3), respectively. As Figure 5.17 shows, the fitted linewidth is about 17 kHz in the regime of the plateau at high temperatures. This value could be explained assuming rapid rotations of the $[AlH_4]$ -tetrahedra around their C_3 symmetry axis in the corresponding temperature range.

Interval in between the plateaus.

In the interval in between the plateaus a two-component fit turned out to be difficult. The broad component in the spectra was in fact a superposition of two lines with linewidths close to the plateaus values, i.e. 17 kHz and 60 kHz (see e.g. in Figure 5.14 the spectrum at 350 K). One can nevertheless obtain a relative good fit to one averaged line which is mainly Gaussian (in Eq. (5.2), $\varsigma = 0.35$) and with a correlation coefficient of about $R^2 = 0.98$.

The apparent activation enthalpies determined from the linewidths of the averaged fit to the broad component between the plateaus in Figure 5.17 (according to Eq. (2.56)) are similar in all samples, i.e., about 235 meV. The main difference between samples containing different amount of catalyst is that the lines start to narrow at lower temperatures when the amount of catalyst is increased.

Three-component fits

As already pointed out in the previous section, a two-component fit is not sufficient in particular in the temperature range between the plateaus. Therefore we use here a three-component fit. One component represents the spike-like line and the other two components are used to capture the dependence of the shape of the dominant broad component in the spectra. The width of the spike-like line was fixed to 3 kHz. The widths of the other two lines were freely adjustable.

In Figure 5.18 the linewidths ($\Delta\nu$) as a function of $1000/T$ are presented for three different samples with different catalyst content. The linewidths essentially do not vary with temperature. Their values are about 3, 17, and 62 kHz. Above approximately 350 K a narrow component with a width of 17 kHz is found in all samples. In the spectra of the 5 mole % sample a line with 17 kHz linewidth is found in the whole temperature range (even though its amplitude is very small at low temperatures). Remembering that the linewidth of Na_3AlH_6 between room temperature and 380 K varies (between about 19 and 17 kHz), one conclude that the always present 17 kHz line in the spectra of this sample indicates that a

bigger part of the sample already decomposed into Na_3AlH_6 during the ball-milling process. We can unfortunately not be sure of how much the changes were reversible in this sample, because we did not measure again the spectra at room temperature after completion of all measurements.

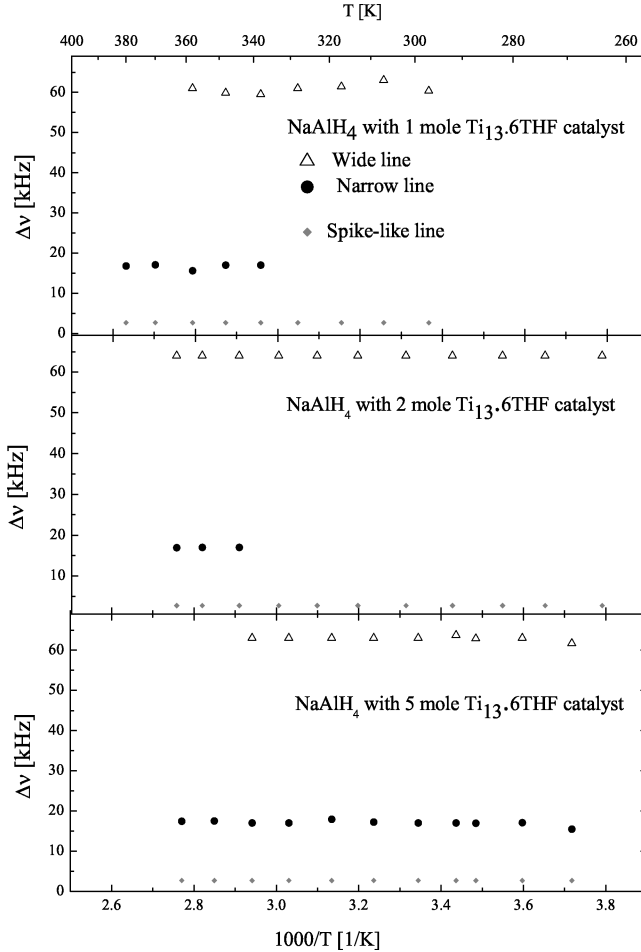


Figure 5.18: Linewidth ($\Delta\nu$) as a function of $1000/T$ of the 1, 2, and 5 mole % samples, assuming that the spectra is composed of 3 components.

In Figure 5.19 the normalized areas under each of the three lines, i.e., spectral weight are shown as function of temperature for the samples containing different amounts of catalyst. The areas under the fitted curves were normalized dividing them by the sum of the three areas. One should note that the spectral weight of the narrow component increases with temperature at the expense of the *slow component*.

Although we obtained a better correlation coefficients for all fittings (all were higher than $R^2 = 0.99$), one should not forget that the obtained values are not very accurate. Their accuracy depends on the noise and the form of the spectra. In some cases the choice of the initial parameters influences the values obtained. From Figure 5.19 one can see that the spectral weight of the wide and narrow line components cross at about 354, 356, and 339 K in the 1, 2, and 5 mole % sample, respectively. The percentage spectral weight of the spike-like line have a similar behavior as found in a two-component fit (see Figure 5.16). Even more, it

can be seen that hydrogen atoms start to desorb at slightly different temperatures, i.e., at approximately **340 K, 330 K and 320 K** for the 1-, 2- and 5-mole % samples, respectively.

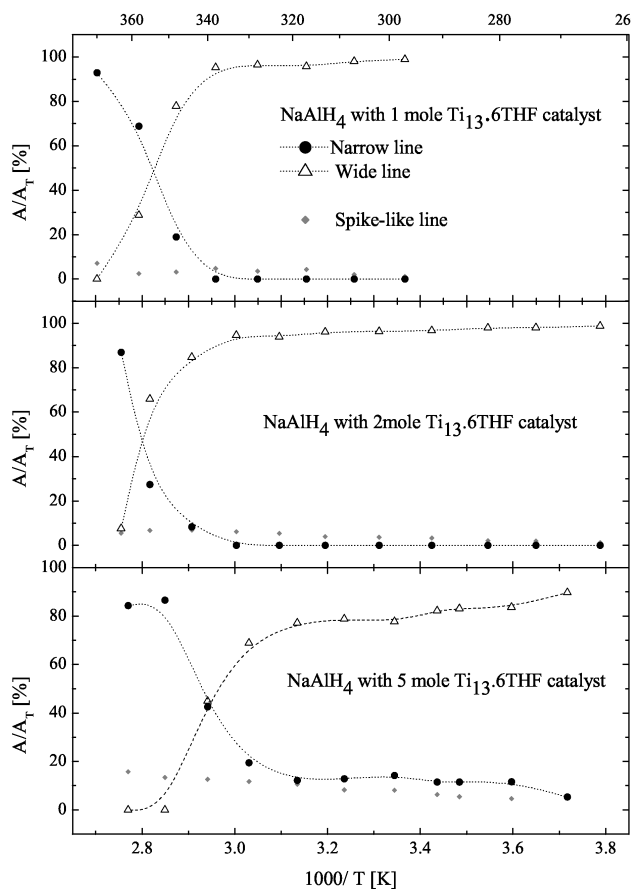


Figure 5.19: Spectral weight for the different components of $\Delta\nu$ as a function of $1000/T$ of the 1, 2, and 5 mole % samples, assuming that the spectra is composed of 3 components.

The coexistence of both components, typical of the before mentioned plateaus, implies the coexistence in the sample of environments in which hydrogen motion at a given temperature is already sufficiently rapid to give rise to incomplete motional narrowing (induced by rapid rotations of the $[\text{AlH}_4]$ -tetrahedra around their C_3) and other parts in which hydrogen motion is still slow such that the rigid lattice condition holds.

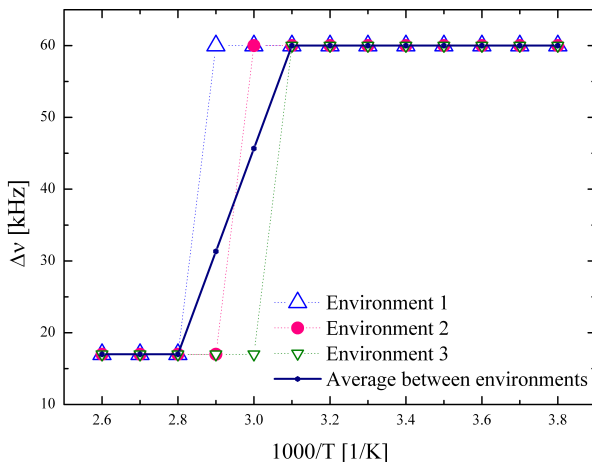


Figure 5.20: Sketch of the assumed temperature change of the ^1H -NMR linewidth for hydrogen atoms in three different environments as well as the effect on a linewidth of a line describing the superposition of all environments (as obtained in the two-component fit). The environment 1 has the smallest distance to the catalyst and the average distance to the catalyst is followed by the environments 2 then by the number 3, respectively.

The temperatures, at which this transitions from the rigid lattice regime to the regime of incomplete motional narrowing occur, are characterized by a certain distribution function. As the temperature rises, the transition has already taken place in larger and larger parts of the sample or in more and more different environments. This explains the increase of the amplitude of the component with a linewidth of about 17 kHz, and the simultaneous decrease of the amplitude of the wide line with a width of about 60 kHz (as the temperature is increased). The transition from the rigid lattice regime to those regimes of incomplete motional narrowing is presumably quite abrupt in each individual part or environment of the sample. Otherwise one would have expected to observe also some gradual change of the linewidths of several of the fitted lines. The typical activation energies – characterizing the hydrogen motion leading to incomplete motional narrowing in different sample parts or in different environments – are expected to be higher than the apparent activation enthalpy obtained from the temperature variation of the linewidth of the broad component (see Figure 5.17) in a two component fit. A diagram of the above ideas is shown in Figure 5.20.

In samples which do not contain catalyst no sign of motional narrowing is observed in the temperature range studied. This suggests that the influence of catalyst might be responsible for a distribution of the temperatures at which the incomplete motional narrowing sets in; the distance of H to the catalyst should be the relevant parameter defining the distinct environments. In the 5 mole % sample the increase of the amplitudes of the line with a width of 17 kHz sets in already at lower temperatures than in the 1 or 2 mole % sample. In samples containing more catalyst, the average distance between hydrogen and the catalyst becomes smaller. This might reduce the temperature at which incomplete motional narrowing sets in and could thus explain the above differences.

5.2.2 Hydrogen mobility and spin-lattice relaxation

The spin-lattice relaxation rates (Γ_1) are usually mediated by motional processes like molecular rotations, diffusion of particles or lattice vibrations. Thus, in order to know more about the dynamics of the system, we measured Γ_1 rates for several samples as a function of temperature. Therefrom, we expect to obtain information on the influence that different treatments may have on the motional processes on the sample. Plotting $\log(\Gamma_1)$ vs $1000/T$, one can find activation enthalpies if the processes are thermally activated and follow an Arrhenius behavior.

The apparent activation enthalpies of hydrogen in the NaAlH_4 samples ball-milled without and with added catalyst ($\text{Ti}_{13} \cdot 6\text{THF}$ catalyst), as well as in Na_3AlH_6 (obtained in Ref. [8]) were deduced from the Γ_1 data measured at 67.7 MHz. These enthalpies are presented in Table 5.30. To study the frequency dependence of Γ_1 , relaxation measurements were performed at a second frequency (at $\omega_0/2\pi = 300$ MHz) on the 2 mole % sample. The corresponding activation enthalpies are also included in Table 5.30.

Ball-milled samples

This section reports the Γ_1 measurements done as a function of temperature on samples without catalyst but ball-milled for 5 and 30 minutes, and for 12 hours. In all three samples the recovery of the proton nuclear magnetization can be described by a single exponential function, characterized by a relaxation rate Γ_1 . A single activated process is somehow surprising as e.g. from the spectra (see section 5.2.1) all ball-milled samples are expected to be very heterogeneous, i.e., the magnetization recovery is expected to be characterized by more than one relaxation rate.

Relaxation rates

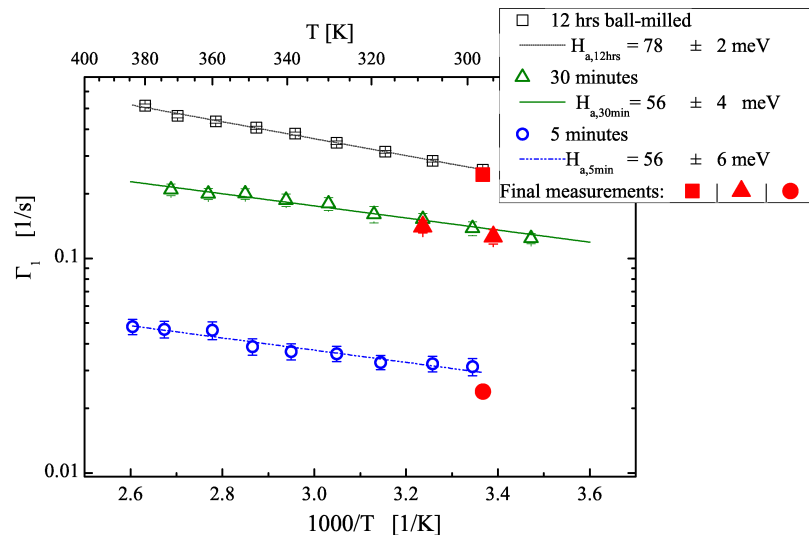


Figure 5.21: Γ_1 rates as a function of $1000/T$ of the samples ball-milled for 5 and 30 minutes as well as 12 hours, with $\omega_0/2\pi = 67.7$ MHz. The full symbols represent the measurements done at about 300 K after completing the heating cycle.

In Figure 5.21, the nuclear spin-lattice relaxation rates (Γ_1) of all milled samples are plotted as a function of $1000/T$. It can be seen that the Γ_1 rates are the higher the longer the milling times were. By ball milling, the Γ_1 rate is enhanced by at least two orders of magnitude in comparison to the untreated samples. Whereas untreated $NaAlH_4$ samples of very high purity have $\Gamma_1^{nont} \sim 3 \times 10^{-4} \text{ s}^{-1}$ at room temperature [8], the Γ_1 rates observed on all milled samples are higher than $\Gamma_1 \sim 3 \times 10^{-2} \text{ s}^{-1}$, i.e.,

$$\Gamma_1^{nont} \ll \Gamma_1 \quad (5.3)$$

For each of the investigated samples the temperature dependence of Γ_1 can be fitted to a single Arrhenius law as can be seen in Figure 5.21. The activation enthalpies obtained for the samples ball-milled for 5 and 30 minutes are identical within the accuracy of our measurements: the activation enthalpies are in $H_{a,5min} = 56 \pm 6 \text{ meV}$ and $H_{a,30min} = 56 \pm 4 \text{ meV}$ for the samples ball-milled for 5 and 30 minutes, respectively. The activation enthalpy determined on the sample milled for 12 hours is somewhat higher, $H_{a,12hrs} = 78 \pm 2 \text{ meV}$.

Slight compositional and structural changes of the samples in the course of the measurements might occur while the samples are at elevated temperatures. In order to test whether Γ_1 is affected by those changes, one or two control measurements have been performed at about room temperature for each sample after completion of each series of measurements. No significant change is observed on the final Γ_1 rates.

Amplitudes

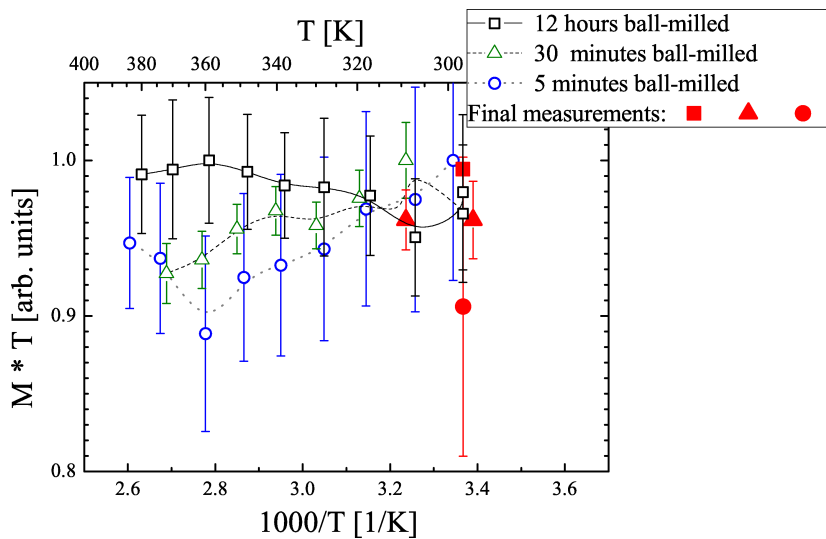


Figure 5.22: Change of hydrogen content versus $1000/T$ of the samples ball-milled for 5 minutes, 30 minutes and 12 hours. The full symbols at about 300 K represent the measurements done after completing the heating cycle.

A measure of the total hydrogen content is obtained by multiplying the amplitude (M) of the magnetization recovery by the absolute temperature (T). The multiplication by T corrects the magnetization decrease expected from the Curie law. Thus $M \cdot T$ is proportional to the hydrogen content in the sample.

The normalized hydrogen content (obtained on the three investigated samples for all the measurements performed at different temperatures) is plotted as a function of $1000/T$ in Figure 5.22. The normalization is such that the biggest $M \cdot T$ values obtained for each particular sample is set to 1.

Within the experimental accuracy no change of $M \cdot T$ and thus of the hydrogen content is observed for the sample milled for 12 hours. This means no significant desorption takes place in the course of the measurements upon heating the sample in steps to the various measurement temperatures. The control measurement at about room temperature carried out at the very end of the whole series of measurements corroborates these findings.

For the samples milled for 5 and 30 minutes indications of some hydrogen desorption during the measurements are found. The hydrogen loss is, however, below about 10 %. This can be seen from the $M \cdot T$ data obtained at elevated temperatures as well as from the control measurements carried out at about room temperature.

The conclusion concerning hydrogen desorption drawn from the relaxation measurements are in line with those drawn from the analyses of the spectra which have been discussed in section 5.2.1. Furthermore, Γ_1 obviously is not influenced by the small compositional and the concomitant structural changes.

Interpretation

The Γ_1 rates of the ball milled NaAlH_4 samples show remarkable increments in comparison to the untreated samples. To discard that those increments are due to contamination with magnetic impurities of the samples, there are at least two reasons. The first reason is that we have used (nominally) nonmagnetic ball milling vial and balls (made of silicon nitride, see Sect. 4.1). The second reason is that on the one hand, only a moderate increase of the contamination with magnetic impurities is expected if the milling time is changed from 5 to 30 minutes. The degree of contamination on the other hand, should rise to a much higher level if the milling time is increased to a value as high as 12 hours. These expected relations between possible degrees of contamination, however, are not reflected in the observed variations of the Γ_1 rates with milling time.

The noticeable increments of the Γ_1 rates are therefore attributed to the creation of either new surfaces by ball milling (associated with a reduction of the average grain size in the powders) or defects (like dislocations or interfaces in the interior of the grains). The created surfaces and/or defects will be now on denoted as “surfaces” of the sample.

It might be expected that hydrogen located near the “surfaces” of the sample is more mobile than in the bulk. A higher mobility implies a higher spin-lattice relaxation rate on the low temperature side of a relaxation maximum (see Figure 2.14). Thus, according with the experimental data (see Figure 5.21), the spin-lattice relaxation rates must be locally enhanced for hydrogen atoms in the vicinity of the “surfaces” of the sample.

Ball-milled samples are composed by atoms in the regions around the surface and those in the bulk, i.e., the samples are heterogeneous. The magnetization recovery of ball milled samples is thus expected to be characterized by two extreme relaxation-rates: A high relaxation rate –

Γ_1^S (characterizing the hydrogen atoms in the vicinity of the “*surfaces*”), and a low relaxation rate – Γ_1^B (the hydrogen atoms in the bulk).

Despite of the heterogeneity of the sample, the experimental rates fitted surprisingly well to a single exponential. This can though be explained if there is a transport of the magnetization between the bulk and the “*surfaces*” of the sample, which is faster than the time that the inversion recovery of the bulk takes to occur. Furthermore, the relaxation rate of the ball-milled samples should then be equal or lower than Γ_1^S

$$\Gamma_1 \leq \Gamma_1^S. \quad (5.4)$$

Assuming that the Γ_1 measurements of the untreated samples of very high purity on Ref. [8] are comparable with the Γ_1^B rate ($\Gamma_1^B \sim \Gamma_1^{non}$) and according to Eq. (5.3) and Eq. (5.4), one can presume that

$$\Gamma_1^B \ll \Gamma_1^S \quad (5.5)$$

The transport mechanism of the magnetization between the bulk and the surface can be given by spin diffusion or/and hydrogen diffusion. Hydrogen diffusion is presumably not relevant in the present case except maybe at the highest temperatures investigated⁵. However, since the tendency of the data does not change in the whole measured temperature interval, one can assume that the magnetization will be averaged out due to spin diffusion.

In Figure 5.23 a diagram is shown explaining the relaxation mechanisms in the ball milled samples. The time that spin diffusion takes to transport the magnetization to the surface is called t_{DS} , where $t_{DS} = L^2/D_S$. D_S denotes the spin diffusion coefficient and L represents a typical distance between hydrogen atoms in the bulk and at internal interfaces or surfaces, i.e., the average length of spin diffusion. The magnetization on the bulk will be transported through spin diffusion if the intrinsic inversion recovery time of the bulk ($T_1^B = 1/\Gamma_1^B$) is longer than t_{DS} [88], i.e., $t_{DS} < T_1^B$ or

$$D_S/L^2 > \Gamma_1^B. \quad (5.6)$$

If the magnetization of the atoms in the bulk is completely transported through spin diffusion D_S to the “*surfaces*” of the sample, no relaxation rate of the bulk (Γ_1^B) will be detected⁶.

Following the same line of argument one can explain the results of the magnetization recovery of the sample milled for 12 hours. According to the analysis of the spectra of that sample (shown in Figure 5.12) about 20 % had decomposed into Na_3AlH_6 during the milling process. However, the magnetization recovery of the sample milled for 12 hours had also a single exponential behavior, i.e., no decay was detected with the relaxation rate specific of Na_3AlH_6 . Thus, spin diffusion should be also involved in the magnetization recovery of this sample.

⁵At those temperatures the diffusion length of hydrogen (within the relevant time scales) could possibly reach the value of typical distances between internal interfaces.

⁶The “*surfaces*” of the sample are the normally called “relaxation centers” on the spin diffusion jargon.

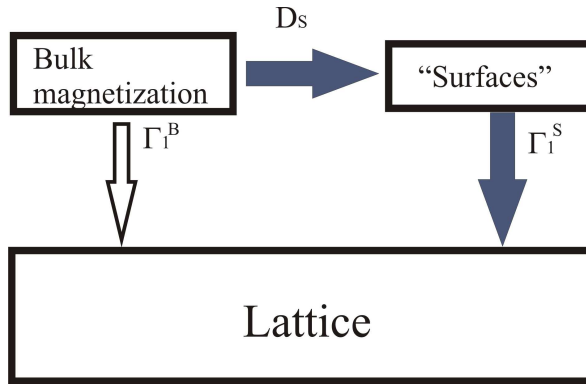


Figure 5.23: Relaxation mechanisms in the ball-milled samples. If the magnetization on the bulk will be completely transported through spin diffusion D_S to the surface, no relaxation rate of the bulk (Γ_1^B) will be detected.

A final question to be answered is whether the activation enthalpies (determined from the Γ_1 measurements) can be related to those activation enthalpies of hydrogen motion near to the “surfaces” of the sample. In order to answer that question, the limits of the spin diffusion have to be analyzed a little more in detail. According to Eq. (5.5) and Eq. (5.6), the limits of D_S will be given by Γ_1^S and Γ_1^B , i.e., either $D_S/L^2 \geq \Gamma_1^S \gg \Gamma_1^B$, or $\Gamma_1^S \gg D_S/L^2 \gg \Gamma_1^B$.

Limit 1: For $t_{D_S} \leq T_1^S \ll T_1^B$, the transport of the magnetization from the atoms in the bulk to the “surfaces” (given by t_{D_S}) is very rapid (more rapid than T_1^S). Thus, the temperature dependence of the relaxation of the whole system Γ_1 must be linearly related to the relaxation rates of the surface of the sample.

Limit 2: In contrast, for $T_1^S \ll t_{D_S} \ll T_1^B$, the temperature dependence of the Γ_1 rate of the whole system must be dominated by that of the spin diffusion rate (D_S/L^2) which is mainly not temperature dependent [88]. Thus, the Γ_1 rate of the whole system will not be temperature dependent, either.

In between: In cases between these limits ($\Gamma_1^S > D_S/L^2 > \Gamma_1^B$), Γ_1 will depend on Γ_1^S more weakly than linearly.

In view of the very small determined activation enthalpies, we conclude that a case between the limits of Γ_1^S is relevant for the Γ_1 measurements discussed here. Therefore, the effective activation enthalpies determined from the Γ_1 data are only some fractions of the activation enthalpies of hydrogen motion in the vicinity of surfaces or interfaces. Empirically, it is indeed not expected to find activation enthalpies for hydrogen motion as low as 55 meV in the temperature range here investigated.

Typical distances between hydrogen atoms in the bulk and those at internal interfaces or surfaces (average length of spin diffusion) are presumably the shorter the longer the milling times. The reduction of the average length of spin diffusion L results in a corresponding smaller t_{D_S} . As a consequence, the spin-lattice relaxation rates are expected to be the higher the longer a sample was ball-milled, as it has been observed experimentally (see Figure 5.21).

Furthermore, D_S/L^2 of the sample ball-milled for 12 hours should be nearer to Γ_1^S than the other two samples. Such a situation would result in a stronger temperature dependence of

the spin-lattice relaxation rate Γ_1 with Γ_1^S . Even though the temperature dependence of Γ_1 may not be completely linear with Γ_1^S (as in the Limit 1), the temperature dependence of Γ_1 yields an effective activation enthalpy of 78 meV. Such enthalpy is already bigger than in the sample ball-milled for 5 and 30 minutes only (around 55 meV).

Samples ball-milled together with catalyst

In this section we consider spin-lattice relaxation rate measurements performed on $NaAlH_4$ samples which have been doped with catalyst. The samples have been prepared by ball-milling the starting material for 30 minutes with 1, 2, or 5 mole % $Ti_{13} \cdot 6THF$ catalyst. Once more, we refer to these samples as 1, 2, or 5 mole % sample.

As an example, the result of a Γ_1 measurement at 338 K on the 1 mole % sample is shown in Figure 5.24. It is evident from this figure that the recovery of the nuclear magnetization cannot be described by a single Γ_1 rate. Instead, a double-exponential recovery function has to be fitted. According to Equation (2.35), that function will be given (for a saturation recovery measurement) as:

$$M(t) = M_{10}(1 - \exp(-\Gamma_{11}t)) + M_{20}(1 - \exp(-\Gamma_{12}t)),$$

i.e., it will be described by two Γ_{1i} values (with $i = 1, 2$) and two equilibrium values M_{i0} .

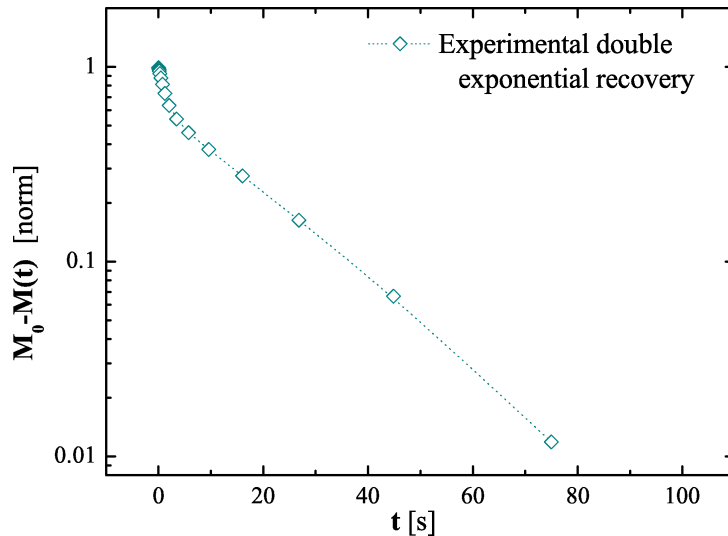


Figure 5.24: Saturation recovery data of the 1 mole % sample at 338 K.

As it can be seen in the figure, one of the two relaxation rates is much higher than the other one. The magnetization component relaxing with the highest rate (Γ_{11}) is called *fast component* and vice versa, the magnetization component relaxing with the lowest component rate (Γ_{12}) *slow component*. The relaxation rate of the *fast component* (Γ_{11}) is typically at least one order of magnitude higher than the *slow component* (Γ_{12}).

The double exponential recovery of the nuclear magnetization shows a striking difference to the behavior of the samples without catalyst, which are well represented by a single exponential recovery function (see initial part of this Section).

Relaxation rates

The temperature dependence of the relaxation rates Γ_{11} and Γ_{12} of the 1, 2, and 5 mole % samples are shown in Figures 5.25, 5.26 and 5.27, respectively.

Relaxation data measured at 67.7 MHz

In a first step, we compare the relaxation data measured on the 1, 2, and 5 mole % samples at a resonance frequency of 67.7 MHz.

A common feature of the *slow components* Γ_{12} is their weak temperature dependence over the entire temperature range. The solid lines fitted to the Arrhenius plots of Γ_{12} correspond to the effective activation enthalpies of 69 ± 26 meV for the 1 mole % sample (Figure 5.25(b)), 58 ± 5 meV for the 2 mole % sample (Figure 5.26(b)) and 23 ± 8 meV for the 5 mole % sample (Figure 5.27(b)). These values are comparable to those observed in the ball-milled samples without catalyst. In the case of the 2 mole % sample, a temperature independent offset in Γ_{12} has been observed below about 190 K. This temperature range has not been covered by the relaxation measurements on the other two samples.

At temperatures below 340 K, the behavior of the *fast component* (Γ_{11}) is similar to the one observed for the *slow component* (Γ_{12}), i.e., it is not strongly temperature dependent. In fact, no temperature dependence at all was found for the line fitted below 340 K of Γ_{11} of the sample with 1 mole % sample (Figure 5.25(a)), as well as for the line fitted below 200 K of the 2 mole % sample (Figure 5.26(a)). The slashed line fitted to the Arrhenius plot of Γ_{11} between 200 and 340 K for the 2 mole % sample (Figure 5.26(a)) gives rise to an activation enthalpy of 59 ± 12 meV, whereas for the 5 mole % sample below 340 K an activation enthalpy of 18 ± 4 meV was found (Figure 5.27(a)).

Approximately above 340 K, a very pronounced increase in Γ_{11} with increasing temperature has been observed in all three samples. This seems to indicate a change in the mechanism responsible for Γ_{11} at about 340 K. In particular, the 1 mole % sample shows an effective activation enthalpy of $E_a = 769 \pm 65$ meV above 328 K (see Figure 5.25(a)), the 2 mole % sample $E_a = 410 \pm 65$ meV above 330 K (see Figure 5.26(a)) and finally the 5 % mole sample 371 ± 3 meV above 340 K (see Figure 5.27(a)).

Control measurements

In order to investigate whether Γ_1 (of both components: Γ_{11} and Γ_{12}) was affected by possible hydrogen desorption, control measurements were carried out after the whole sequence of measurements on the 1 and 2 mole % samples. Both control measurements are also shown in the Figures 5.25, 5.26, respectively.

The control measurements of the 1 mole % sample do not show any significant changes in the Γ_1 rates. Therefore the measurement of this sample was mainly reversible as expected from the section 5.2.1.

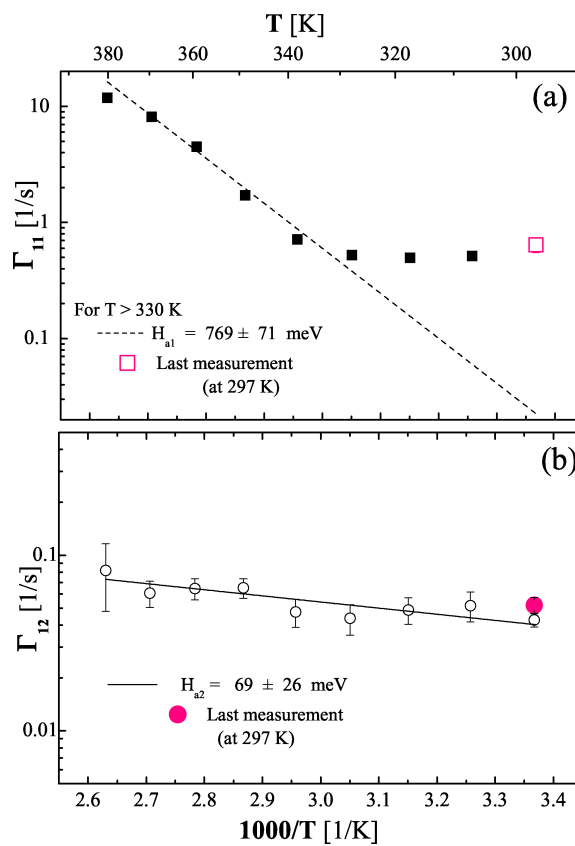


Figure 5.25: 1 mole % sample measured at 67.7 MHz: (a) *Fast component* (Γ_{11}) *vs* $1000/T$, (b) *Slow component* (Γ_{12}) *vs* $1000/T$.

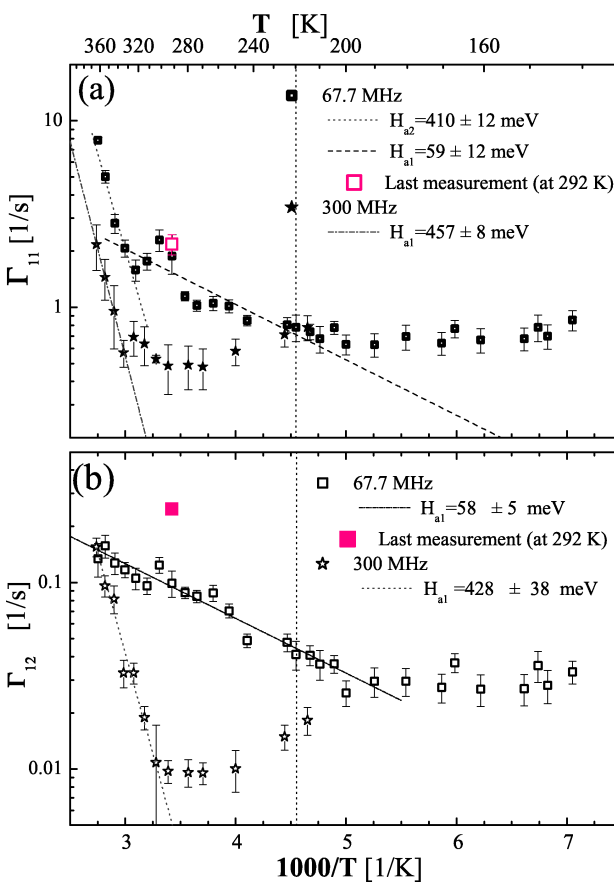


Figure 5.26: 2 mole % sample measured at 67.7 and 300 MHz: (a) *Fast component* (Γ_{11}) *vs* $1000/T$, (b) *Slow component* (Γ_{12}) *vs* $1000/T$.

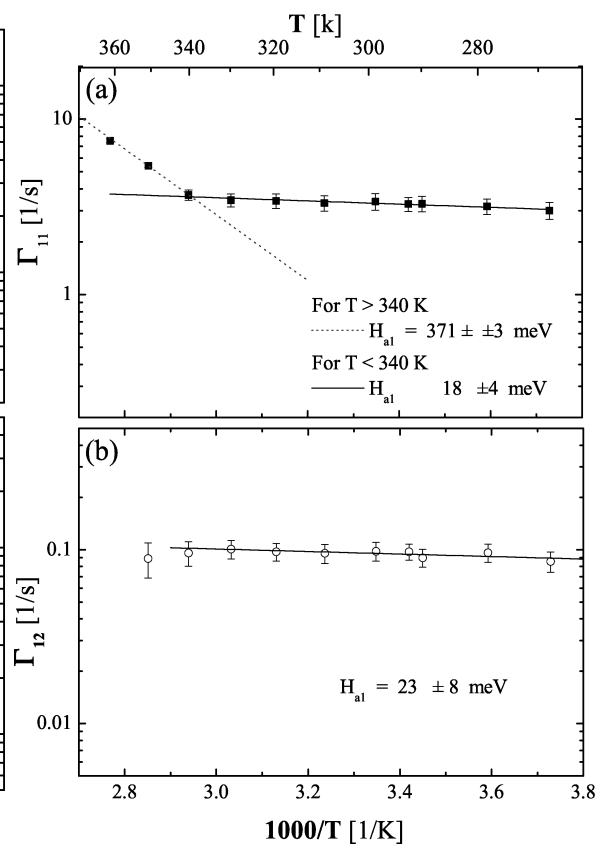


Figure 5.27: 5 mole % sample measured at 67.7 MHz: (a) *Fast component* (Γ_{11}) *vs* $1000/T$, (b) *Slow component* (Γ_{12}) *vs* $1000/T$.

The control measurement at 67.7 MHz done in the 2 mole % sample (Figure 5.26) shows a difference in the Γ_1 values, especially in the *slow component*.

Frequency dependence of Γ_1

The frequency dependence of the spin-lattice relaxation rates has only been investigated for both samples with 2 mole % catalyst (see details of the samples in Chap. 4.2.1 or in Table 4.3). In the second 2 mole % sample measurements have been performed at 300 MHz. At this frequency, the recovery of the nuclear magnetization shows again a double exponential behavior. The *fast component* Γ_{11} shows a temperature dependence which is similar to that observed at 67.7 MHz. Between 250 and 340 K the variation of Γ_{11} with temperature is rather small. Above 340 K the *fast component* increases strongly with temperature. The dash-dotted line in Figure 5.26(a) corresponds to an activation enthalpy of $E_a = 457 \pm 8$ meV, which is very close to the value of $E_a = 410 \pm 65$ meV obtained at 67.7 MHz. The measurement at 300 MHz revealed lower absolute values for Γ_{11} compared to the values measured at 67.7 MHz. For $T > 340$ K the difference, however, is only about a factor of three. For a pure motion-induced dipolar relaxation with a single activation enthalpy, the relaxation rate on the low-temperature side of the relaxation maximum is expected to scale with ω_1^{-2} , if ω_1 is the NMR frequency. This simple model predicts a relaxation rate at 300 MHz which is reduced by a factor of 19.6 compared to the relaxation rate at 67.7 MHz. The experimentally observed frequency dependence, however, is much lower. The data shown in Figure 5.26(a) indicate Γ_{11} values at 300 MHz, which are smaller by a factor of three only compared to the values measured at 67.7 MHz.

In the case of the *slow component* (Γ_{12}), the values were measured at 300 MHz (see Figure 5.26(b)). The temperature dependence of the Γ_{12} data at 300 MHz is much stronger, and the corresponding effective activation enthalpy of 428 ± 38 meV. This value is close to those obtained from the temperature dependence of the Γ_{11} data above 340 K. Due to the higher activation enthalpy at 300 MHz, the Γ_{12} rates at about 365 K are almost identical (those measured at 300 and 67.7 MHz) (see Figure 5.26(b)).

Amplitudes

The normalized amplitudes of both components for the 1, 2, or 5 mole % sample (measured at 67.7 MHz) are plotted in Figure 5.28 as a function of $1000/T$. In these graphs it can be seen that at the lowest measured temperatures, the amplitude of the *fast components* are normally smaller than that of the *slow ones*. However, in all samples measured at 67.7 MHz, the amplitude of the *fast component* becomes more important as the temperature increases. At a certain temperature the amplitude of the *fast component* becomes bigger than that of the *slow one*. We call that temperature at which both amplitudes are identical *cross-point*. For the 1, 2, and 5 mole % samples the *cross-points* were at 359, 344, and 329 K, respectively. The temperature of the *cross-points* decreases with increasing amount of catalyst.

As soon as the *cross-point* is reached and the temperature keeps increasing, the amplitude of the *slow component* gets smaller until finally the *slow component* becomes almost zero (at

least with the 1 and 5 mole % samples). For the shown 2 mole % sample, it is not possible to see very clearly how the amplitude of the *slow component* goes to zero because we only measure until 363 K.

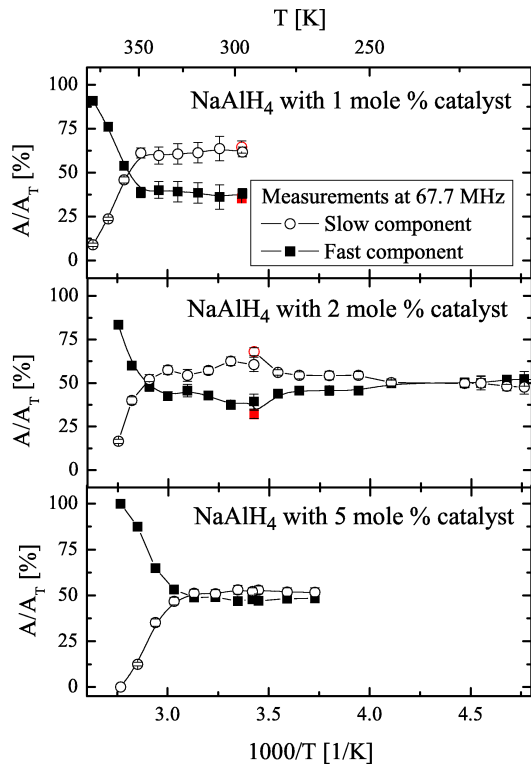


Figure 5.28: Normalized amplitudes of the Γ_1 -components as a function of $1000/T$ of the 1, 2, and 5 mole % samples (all measured at 67.7 MHz).

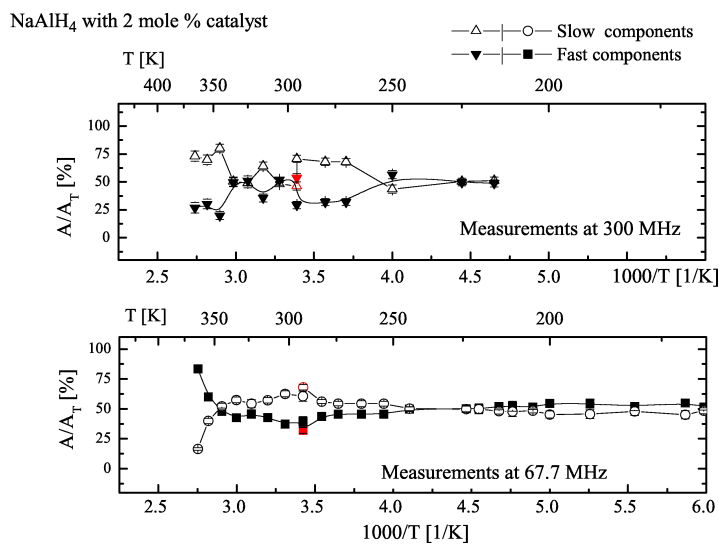


Figure 5.29: Normalized amplitudes of the Γ_1 -components as a function of $1000/T$ of both 2 mole % samples measured at 67.7 and 300 MHz.

In Figure 5.29 one can see the normalized amplitudes of the Γ_1 -components as a function of $1000/T$ of the two 2 mole % samples, i.e., measured at 67.7 and 300 MHz. Contrary to what we found in the amplitudes of the ball-milled samples with catalyst at 67.7 MHz (that the amplitude of the *fast component* grows as the temperature is increased), at 300 MHz the amplitude of both components remains constant the last three points. Even in the last point at 365 K the value of the *fast component* was 25 %.

In table 5.30 the obtained E_a values of all catalyzed samples obtained at 67.7 MHz, as well as those measured on the second 2 mole % sample (measured at 300 MHz) are summarized. The initial and final amplitudes, as well as the *cross-points* of each sample are also tabulated.

Hydrogen losses during the measurements

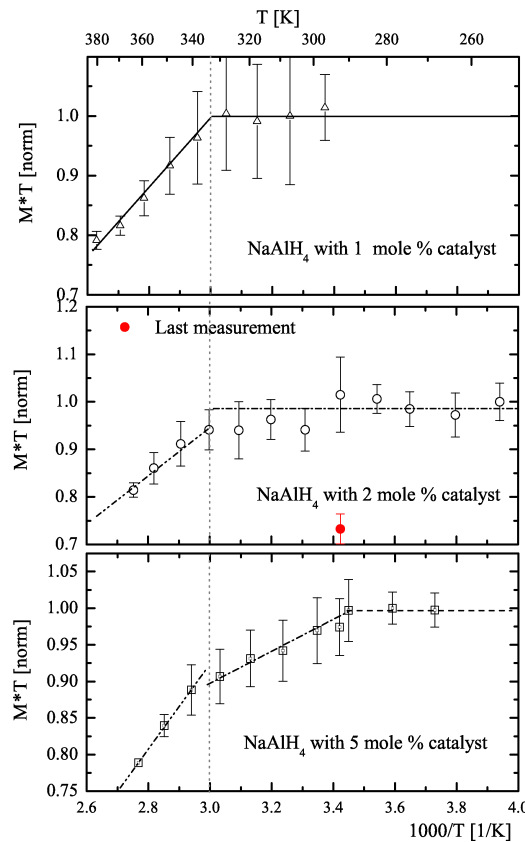


Figure 5.30: Hydrogen content versus $1000/T$ in the 1, 2, and 5 mole % samples. The solid symbol (in the 2 mole % sample) is the only measurement done after the heating cycle, where the measuring parameters were maintained constant (after the first series of measurements).

The normalized total magnetization is the sum of the amplitude of the *slow* and the *fast component* normalized to the highest value. In each of the graphs in Figure 5.30 the normalized total magnetization is plotted as a function of $1000/T$. At the lowest temperatures in the graphs, there is almost no change in the hydrogen content in all samples with catalyst. The 1 mole % sample started to loose hydrogen above approximately 330 K and up to 380 K lost 21 % of its hydrogen content. The 2 mole % sample started to loose hydrogen also

above 330 K and up to 363 K lost 19 % of its hydrogen content. Finally, the 5 mole % sample started to loose hydrogen at about 290 K. The loss in hydrogen content is nevertheless more pronounced above 330 K. This sample lost up to 360 K 20 % of its hydrogen content.

In order to compare the hydrogen content losses of all sample, one uses the fitted lines. From those fittings, one can estimate that from low temperatures up to 370 K the 1, 2, and 5 mole % samples would desorb 19, 21 and 25 % of the hydrogen content, respectively. The change on hydrogen content in the samples with catalyst was at least twice as high as in the ball-milled samples not containing catalyst (hydrogen loss of max. 10 %).

In the center of Figure 5.30 the measurements done in the 2 mole % samples are plotted. Unfortunately, only in the case of the 2 mole % sample, a measurement was performed with the same measuring parameters at room temperature, after the cycle was completed. The result of this measurement is the solid symbol shown in Figure 5.30. Thus only in this case the amount of released hydrogen could be determined precisely. This control measurement resulted in a remaining hydrogen content of 73 ± 3 %, which disagrees a bit with what we expect from the measurements at higher temperatures (81 ± 2 %). That disagreement can be understood by the fact that the room temperature measurement was performed four days after the measurement at 360 K, i.e., some hydrogen may be lost at room temperature during that period of time.

Sample	Catalyst mole . %	Milling time [min]	Activation enthalpies Fast comp. [meV]	Slow comp. [meV]	Cross-point* [K]
Measurement done with 300 MHz spectrometer					
<i>NaAlH</i> ₄	2	30	457 ± 8	428 ± 38	—
Measurements done with 67.7 MHz spectrometer					
<i>NaAlH</i> ₄	1	30	769 ± 65	69 ± 17	359
	2	30	410 ± 65	58 ± 5	344
	5	30	371 ± 3	23 ± 8	329
<i>NaAlH</i> ₄	0	5		56 ± 6	
	0	30		56 ± 4	
	0	12 hrs.		78 ± 2	
Untreated <i>Na</i> ₃ <i>AlH</i> ₆ sample		230			

Table 5.2: Compendium of the activation enthalpies found at 67.7 MHz for the 1, 2, and 5 mole % samples, as well as *NaAlH*₄ samples without catalyst but milled for 5 and 30 minutes, and for 12 hours. Also tabulated are the activation enthalpies of *Na*₃*AlH*₆ measured also at 67.7 MHz [8] and of the second 2 mole % sample measured at 300 MHz.

Interpretation

The double exponential recoveries found in the catalyzed samples (the 1, 2, and 5 mole % sample) imply that there are two main regions in the sample, each region relaxes following a different relaxation mechanism.

In the catalyzed samples, the relaxation rates of the *slow component* (Γ_{12}) behave identically to the samples ball-milled without catalyst, i.e., the Γ_1 -values as well as the activation energies are very similar. In the first part of this section, the relaxation mechanism of the ball-milled samples (without catalyst) was established to be due to spin diffusion between the “surface”⁷ and the bulk.⁸

From the similitude of the Γ_1 of the sample without catalyst and the *slow component* of the samples with catalyst (Γ_{12}), one can conclude that the relaxation mechanism of the *slow component* should be mainly related to the spin diffusion phenomena between the “surface” and the bulk.

Similar to the samples ball-milled, the determined activation enthalpies were very small. This implies that these enthalpies were only fractions of those in the vicinity the “surfaces” (not loaded with catalyst). Even more, it should be noted that the component loses importance (its amplitude decreased) as the temperature increases above 340 K (see Figure 5.28).

By simple exclusion, the *fast component* should be thus related to the influence of the catalyst in the sample.

In Figure 5.31, a diagram summarizing all possible relaxation mechanisms in catalyzed samples is presented. The relaxation of the total magnetization depends on the relaxation rates in each of the surfaces with and without catalyst and on the main part of the sample, i.e., atoms in the bulk. In the case of having spin diffusion in the sample, the relaxation centers of the *fast component* will be defined by the surfaces and internal interfaces loaded with catalyst. The double exponential behavior will thus indicate that the spatial averaging by spin diffusion is not complete [88], [89]. Furthermore, the relaxation mechanism will be then chosen by the nearest relaxation center.

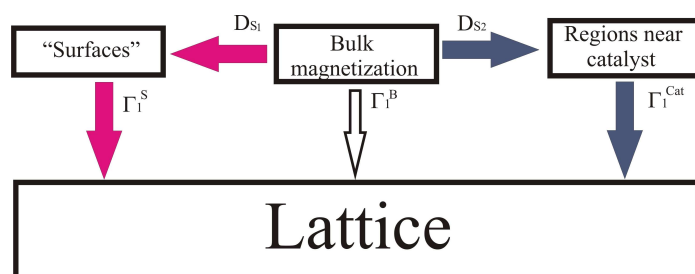


Figure 5.31: Relaxation mechanisms in catalyzed samples. The magnetization on the bulk develops through spin diffusion in regions near the “surfaces” (D_{S_1}) or near the catalyst (D_{S_2}), or through the atoms in the bulk (Γ_1^B). The relaxation centers of the spin diffusion will be given by the atoms near the surface (Γ_1^S) and those near the catalyst (Γ_1^{Cat}).

⁷“Surfaces” are defined as the grain surfaces and the internal interfaces (not loaded with catalyst).

⁸The spin diffusion was established on the ball-milled samples by three criteria. The first criteria was the single exponential behavior of the relaxation rates despite the heterogeneity of the samples (the samples consist of atoms in regions either around the surface or in the bulk). The second criteria was that the relaxation rates tendency did not change as a function of temperature (to discard hydrogen diffusion as a possible magnetization transport). Finally, the third criteria was the low temperature dependence also of the relaxation rates with the temperature (the very small activation enthalpies).

The behavior of the ***fast component*** is splitted in two temperature regions below and above 340 K. In the low temperature region (below 340 K) the *fast component* shows very low or even zero temperature dependence. Therefore, in analogy with the samples without catalyst, the relaxation mechanism will be given by spin diffusion. In the high temperature region (above 340 K), the *fast component* of Γ_{11} has a strong temperature dependence. A similar phenomena characterized by the coupling of the entire system via spin diffusion at low temperature and a process of high activation enthalpy at high temperature was before found in Ref. [90]. The high activation enthalpy was ascribed in Ref. [90] to a motion induced relaxation. In analogy, it is quite probably that the high activation enthalpy process should be due to a motion induced relaxation of the bulk (Γ_1^B).

In order to see if the last assumption is right, one can make use of the results in section 5.2.1. In that section, we studied the spectra as a function of temperature. Each spectrum clearly shows 2 dominant lines, one representing the rigid lattice regime and another representing the part of the sample related to the rotation of the AlH_4 -tetrahedra, called incomplete motional narrowing. Looking at Figure 5.19, one can observe the decrease of the spectral weight of the line related with the rigid lattice regime and the simultaneous increase of the spectral weight of the line related with the incomplete motional narrowing. Comparing now the behavior of the *fast* and *slow components* in Figure 5.28 and the two dominant lines of Figure 5.19, one can see that both graphs are very similar, even their cross-points. Thus, one can also ascribe the motion induced relaxation with the same thermally activated process, i.e., with the rotation of the AlH_4 -tetrahedra.

This motional process will in that way dominate over the relaxation via spin diffusion of the relaxation centers around the catalyst (Γ_1^{Cat}) at temperatures above 340 K. Furthermore, from the increase of the spectral weight of *fast component* at temperatures above 340 K, the relaxation of the bulk (Γ_1^B) will start to dominate also the total magnetization while the temperature is increased.

It is interesting to realize that also at 340 K in all catalyzed samples the hydrogen losses shoot up. This coincidence therefore indicate that at about 340 K an energetic threshold is exceeded, which allows the rotation of the tetrahedra. This rotation can thus be considered as a precursor of the faster hydrogen desorption in the catalyzed the samples.

When the relaxation of the bulk (Γ_1^B) begins to dominate the total magnetization, (i.e., when the amplitude of the *fast component* starts to grow up) one finds a *cross-point*. One can thus conclude that these *cross-points* give us a way to estimated which sample starts to be thermally activated first. The temperature at which the samples could be thermally activated was in fact reduced as soon as more catalyst was used.

That the relaxation rate of the *fast component* is at least one order of magnitude higher than the *slow component* can indicate that either the catalyst (relaxation center) is working as a paramagnetic center, or the hydrogen atoms around catalyst are more mobile. We cannot completely exclude that there are no paramagnetic impurities involve in this process, however, there are at least two strong arguments to assume that this increment will be mainly due to a higher mobility. The first argument comes from what other groups already found (see e.g. [36], [37] or [9]). According to those references, it should be expected that spin

relaxation is much faster in samples with catalyst because hydrogen is desorbed faster and at lower temperatures by the use of catalysts (see e.g. Figure 1.7). The second argument is the obtained activation enthalpies at high temperatures, which indicate a motion induced relaxation (not found in samples without catalyst). Furthermore, the higher catalyst contents were needed the lower activation enthalpies, i.e., catalyst favors the motion in the sample. This is also in agreement with the Refs. [36], [37] and [9]. Specifically in [36] found that the hydrogen desorption was faster the more catalyst $Ti_{13} \cdot 6THF$ catalyst was used.

Frequency dependence of Γ_1

The frequency dependence of Γ_1 at the low-temperature side of the relaxation maximum is significantly lower than ω_0^{-2} . A ω_0^{-2} frequency dependence is expected for a single thermally activated diffusion process. This reduced frequency dependence suggests that the relaxation is caused by motional process with a broad distribution in activation enthalpies [91], [92], [93].

The activation enthalpy of the *slow component* at 300 MHz is very similar to the value obtained for the *fast component*. This is unexpected and may be caused by the fact that when the thermic activation process appears, the rotations in the distant could influence the environment of the atoms in the bulk. This could give rise to very low Γ_1 rates.

5.3 NMR studies of hydrogen desorption on $NaAlH_4$ samples ball-milled with catalyst (at a constant temperature)

This section intends to understand first how hydrogen is desorbed and second the structural and compositional changes suffered by $NaAlH_4$ (ball-milled with catalyst) due to decomposition into Na_3AlH_6 . To study this process a serie of spectra and their relaxation rates (Γ_1) were measured at a constant temperature as a function of time. The interpretation of both types of measurements is shown in Section 5.3.3. Further technical details of the measurements are presented in Section 4.2.2. In addition, all specifications of the samples are given in Section 4.1 and summarized in Table 4.4.

5.3.1 Hydrogen desorption studied by changes on the NMR spectra

The spectra of a 1 mole % sample measured during about 900 minutes (maintaining the temperature constant at around 336 K) are shown in Figure 5.32. As in Section 5.2.1, the spectra can be fitted to a wide and a narrow component plus a spike-like line (with a fixed linewidth of 3 kHz). The linewidths of the components were about 17 and 62 kHz. Even though in this section the temperature was set constant, as time proceeded the amplitude of the wide component became lower, and the amplitude of the narrow component became higher.

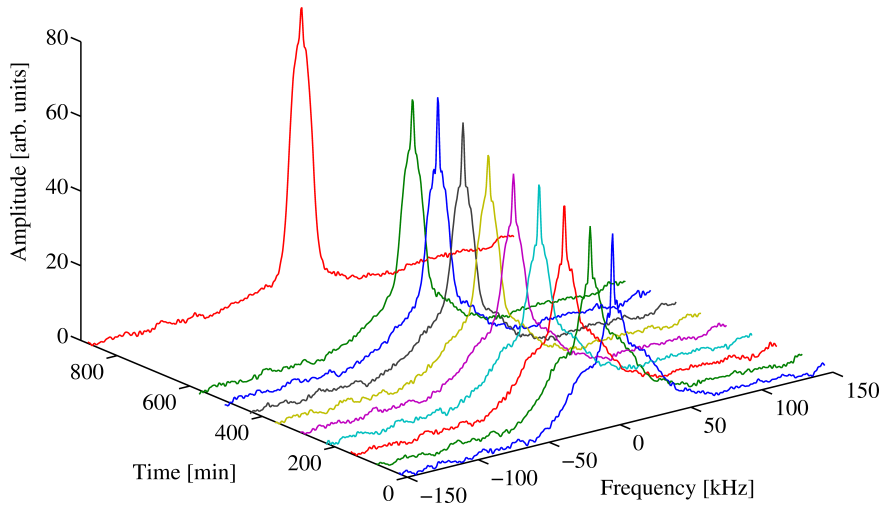


Figure 5.32: Change in the spectra of the 1 mole % sample at 336 K for about 900 minutes.

As outlined above, a pronounced change in the spectra of the 1 mole % sample has been observed over a time interval of 900 minutes at 336 K (see Figure 5.32). The spectrum observed after 900 minutes is very similar to that measured on pure Na_3AlH_6 (compare Figure 5.1). Based on this observation only, one could conclude that $NaAlH_4$ sample has completely decomposed into Na_3AlH_6 . However, the total spectral weight changes only approximately 10 % of its value after e.g. 570 minutes. This corresponds to a hydrogen release of 10 % indicating that 20 % of the $NaAlH_4$ transformed into Na_3AlH_6 (which has only half the hydrogen content). Part of the spectral changes can be ascribed to a partial line narrowing (to a linewidth of about 17 kHz) related to the rotation of $[AlH_4]$ tetrahedral in $NaAlH_4$ around the C_3 axis (compare Table 5.1). In order to investigate both, the decomposition reaction and the motional processes in more detail, time dependent measurements of the spin-lattice relaxation rates and the corresponding NMR signal amplitudes were performed. The results of these investigations are presented below.

5.3.2 Hydrogen desorption studied by spin-lattice relaxation measurements

The spin-lattice relaxation rates were measured at constant temperatures on the 1, 2, and 5 mole % samples. As previously found the Γ_1 - rate measurements on samples ball-milled with catalyst can only be completely described if two exponential rates and their corresponding amplitudes are used. In these measurements, the highest rate will be called *fast component* (Γ_{11}) and the lowest rate, *slow component* (Γ_{12}).

Relaxation rates

In Figures 5.33, 5.34 and 5.35 the *slow* and *fast* relaxation rates of the 1, 2, and 5 mole % sample, respectively, are plotted as a function of time. The *slow components* in Figures 5.33 (b), 5.34 (b), and 5.35 (b) have practically no relaxation time dependence during the initial interval. The *slow*

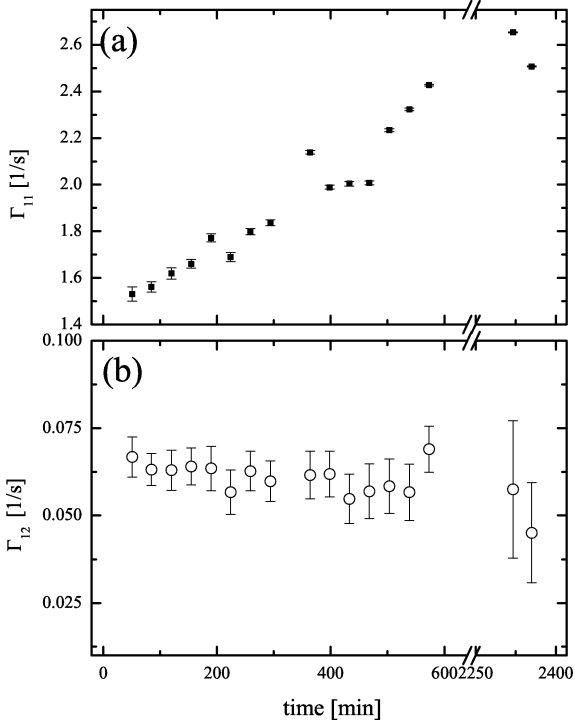


Figure 5.33: 1 mole % sample measured at $T = 336\text{ K}$: (a) *Fast component* (Γ_{11}) vs. time, (a) *Slow component* (Γ_{12}) vs. time.

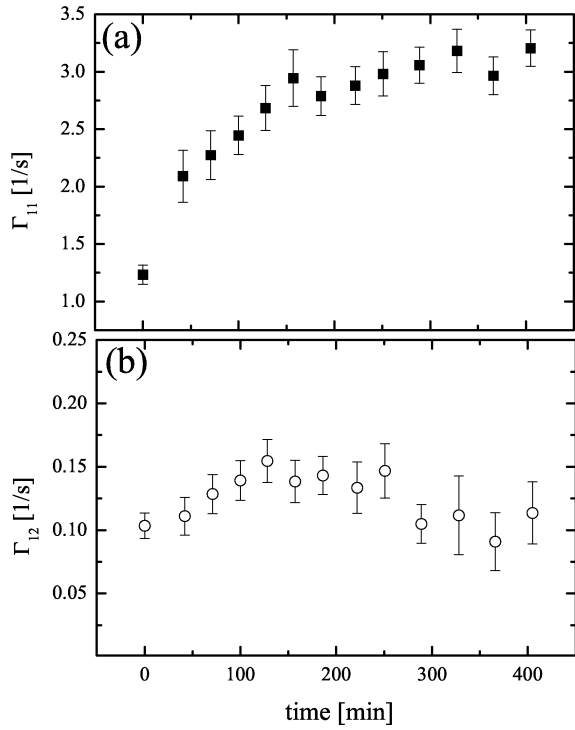


Figure 5.34: 2 mole % sample measured at $T = 338\text{ K}$: (a) *Fast component* (Γ_{11}) vs. time, (a) *Slow component* (Γ_{12}) vs. time.

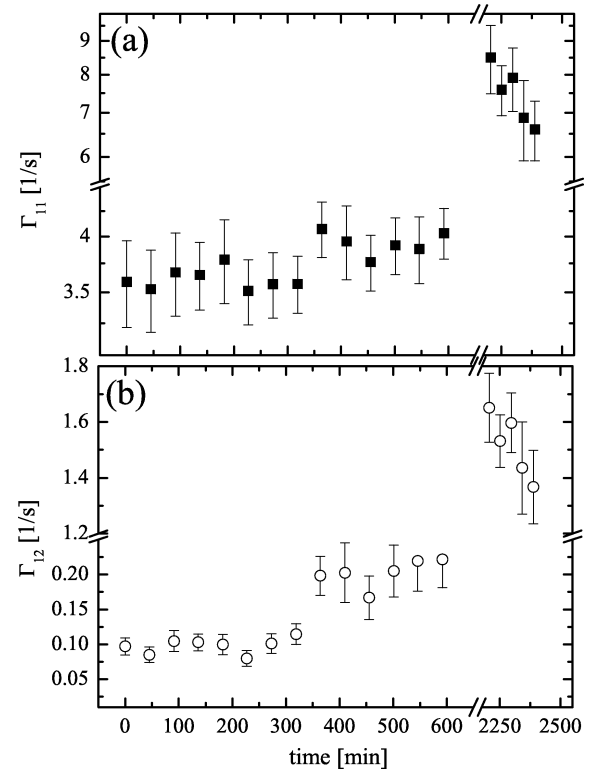


Figure 5.35: 5 mole % sample measured at $T = 329\text{ K}$: (a) *Fast component* (Γ_{11}) vs. time, (a) *Slow component* (Γ_{12}) vs. time.

components Γ_{12} of the 1, 2, and 5 mole % sample stay initially around 0.062 1/s, 0.12 1/s, and 0.15 1/s, respectively. Only the last values of the *slow component* of the 5 mole % sample show a discontinuity of one order of magnitude to 1.5 1/s on the last measurements (after 2200 minutes).

The *fast components* of the 1 and 2 mole % sample increase their value initially as a function of time (See Figure 5.33 (a) and 5.34 (a)). The Γ_{11} rates of the 2 mole % sample increase asymptotically to about 3.0 1/s. Even though we were unable to determine the form of the increment for the 1 mole % sample, one can extrapolate that the increase will also be asymptotical as all samples have similar “behavior”⁹. In this case, however, it will most probably go to around 2.6 1/s, i.e., to the last measured value at about 2300 minutes. The *fast component* of the 5 mole % sample is already at around 3.75 1/s at the first measurement. The values of the *fast component* - 2.6 1/s for the 2 % sample and 3.75 1/s for the 5 mole % sample - are roughly the obtained in the measurements as a function of temperature (around the same temperatures). The Γ_{11} values of the 5 mole % sample shown another jump of their value after 2200 minutes around 8 1/s. The value of this measurement roughly corresponds to the expected value for Na_3AlH_6 around that temperature [8].

Amplitudes

The corresponding amplitudes of the exponential decays of the 1, 2, and 5 mole % samples are shown in Figures 5.36 (b), 5.37 (b), and 5.38 (b), respectively. Similarly, as in the Γ_1 measurements against temperature, the amplitude of the *slow component* decreases inversely proportional to the *fast component*. Only that in this case the change of the amplitudes occur as a function of time and not of temperature. This tendency is inversed only in the case of the 5 mole % sample at the end of the measurement, where the final amplitude of the *slow component* increases inversely proportional to the *fast component* as a function of time.

Hydrogen lost during the measurements

The total amplitude of the Γ_1 -measurements (the sum of both amplitudes of the Γ_1 rates) can also be used to estimate the change in hydrogen content. The total amplitude of the equilibrium magnetization can be related to the initial hydrogen content. Here, the total magnetization is normalized to its highest value. In Figures 5.36 (a), 5.37 (a), and 5.38 (a), the changes in total amplitudes are shown of the samples with 1, 2, and 5 % samples, respectively.

In all measured samples and at the given temperatures, the total amplitudes decreased as a function of time. Hydrogen desorption, of the 1, 2, and 5 mole % samples during the measured time intervals were about 14, 12, and 15 %, respectively. With the measurement done in the 5 mole % sample (Figure 5.38), the amplification of the NMR signal was adjusted (to improve the measurement signal) after 600 minutes. Based on these measurements it is not possible to compare the amplitudes (hydrogen content) of the 5 mole % sample from before and after 600 minutes.

⁹This means from the results obtained until now (e.g. the measurements as a function of temperature), one knows that with more catalyst the hydrogen desorption is more efficient (faster and at lower temperatures).

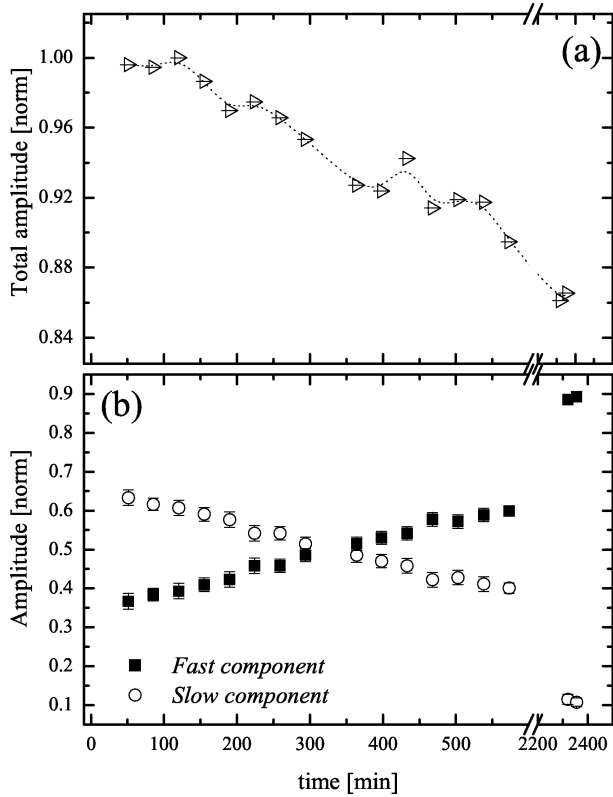


Figure 5.36: 1 mole % sample measured at $T = 336\text{ K}$: (a) Total amplitude *vs.* time, (b) Amplitudes of the *slow* and *fast component* *vs.* time.

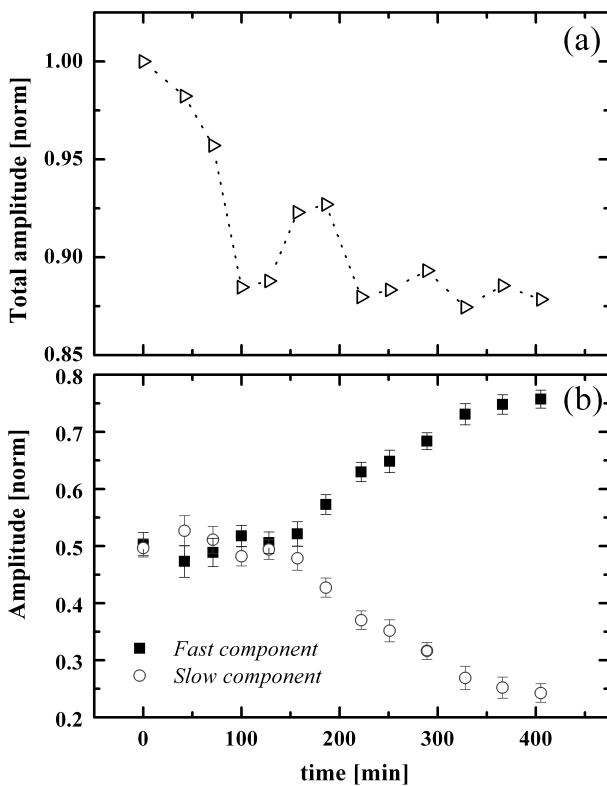


Figure 5.37: 2 mole % sample measured at $T = 338\text{ K}$: (a) Total amplitude *vs.* time, (b) Amplitudes of the *slow* and *fast component* *vs.* time.

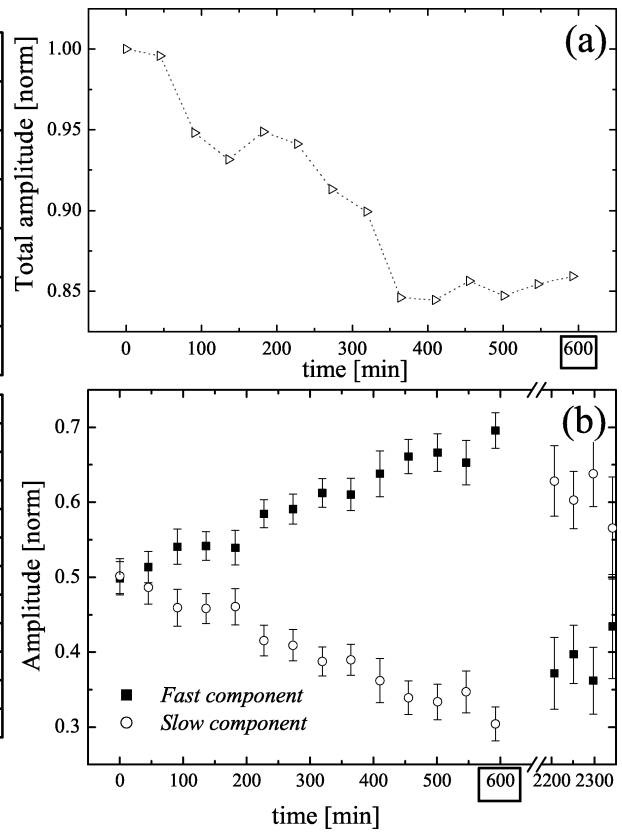


Figure 5.38: 5 mole % sample measured at $T = 329\text{ K}$: (a) Total amplitude *vs.* time, (b) Amplitudes of the *slow* and *fast component* *vs.* time.

In addition to the quantity of hydrogen atoms, the amplitudes of these measurements are also correlated to the quality of the inversion-recovery experiment. If the signal is not so well matched or if the magnetization has not completely recovered to its equilibrium state, the apparent amplitude is reduced (see Figure 2.10). Because of the experimental errors the final total amplitudes in the Figures 5.36, 5.37, and 5.38 seem to be oscillating.

In order to be able to compare the samples themselves, we looked at a common interval, i.e., at the first 250 minutes. In that time interval the change of the total amplitudes of the 1, 2, and 5 mole % sample changed 4, 5, and 10 %, respectively. From this change, as in the measurements as a function of temperature, it was determined that the more catalyst is used the more hydrogen desorption occurs.

5.3.3 Interpretation of the measurements as a function of time

The hydrogen desorption in a given time interval is related to the decomposition of $NaAlH_4$ and the formation of Na_3AlH_6 during that period. As the hydrogen content of Na_3AlH_6 is only half the value of $NaAlH_4$, one can estimate from the total loss of hydrogen, how much $NaAlH_4$ must have been transformed into Na_3AlH_6 during the experiment. The sample with 1 mole % catalyst released, for example, 11 % of hydrogen within 570 minutes at 336 K (see Figure 5.36). During the same time period, the fraction of the amplitude of the fast component increased from 36 % to about 60 %, and, accordingly, the fraction of the slow component decreased from 64 % to about 40 %. Assuming that at the beginning of the experiment most hydrogen atoms are bound in $NaAlH_4$ (and 36 % in Na_3AlH_6) a release of 11 % of hydrogen would result in 42 % (64 % - 22 %) hydrogen in $NaAlH_4$, 47 % (36 % + 11%) hydrogen in Na_3AlH_6 and 11 % hydrogen in the gas phase. Normalized to the remaining hydrogen content in the sample after the hydrogen release (which is only 89 % of the starting value), only approximately 47 % of the hydrogen would be in $NaAlH_4$ and 53 % in Na_3AlH_6 . These values differ from the fractions of *fast* and *slow components*, which are about 40 % and 60 % (see Figure 5.36). At first glance it seemed to be reasonable to assume that the two contributions to the spin-lattice relaxation rate Γ_1 could be directly ascribed to the two components $NaAlH_4$ and Na_3AlH_6 (as Γ_1 at 336 K is significantly higher in Na_3AlH_6 than in $NaAlH_4$ [8]). However, the changes of amplitude of the fast and slow components of Γ_1 are stronger than expected under this assumption.

These results may indicate that in some of the environments of $NaAlH_4$, the hydrogen atoms show a motion-induced Γ_1 rate similar to that in Na_3AlH_6 . The temperature at which the time depend measurements were performed (at 336 K) is close to the onset temperature for the rapid rotation of the $[AlH_4]$ -tetrahedra around their C_3 -axis (see Section 5.2.1). Such rotations cause a partial line narrowing (to a linewidth of about 17 kHz), and they are expected to also increase the motion-induced spin-lattice relaxation. It is reasonable to assume that the partial decomposition of $NaAlH_4$ under formation of Na_3AlH_6 and metallic Al causes structural defects in the remaining $NaAlH_4$. Close to lattice defects the energy barrier for the rotation of the $[AlH_4]$ -groups in $NaAlH_4$ may be reduced. This rather simple picture gives one possible explanation why the increase of the fast component of Γ_1 is more pronounced than expected on the basis of Na_3AlH_6 formation only.

Lattice defects related to the partial decomposition of Ti-doped $NaAlH_4$ are not only expected to reduce the average energy barrier for the rotation of the $[AlH_4]$ -groups but also to cause a rather broad distribution of barrier heights. Such a distribution of energy barriers for a motional process results in a reduced frequency dependence of a motion-induced dipolar spin-lattice relaxation at low-temperature side of the relaxation maximum. Γ_1 measurements on $NaAlH_4$ samples with 2 mole % catalyst at 300 MHz and at 68 MHz indicated indeed a frequency dependence which is significantly lower than ω_0^{-2} (see Section 5.2.2).

In the 5 mole % sample after 600 minutes, the final parameters of the measurement (e.g. the amplification) were changed. This change of experimental parameters does not permit to estimate how much hydrogen was left within the sample. Therefore it is not certain that the sample had already decomposed to Na_3AlH_6 after the interruption at 600 minutes. We may, nevertheless, make use of the similarities in the “behavior” that the samples have shown. Observing how small the amplitudes of the last points of the *slow component* were for the 2 mole % sample in Figure 5.37 (b), one could infer that the initially called *slow component* disappeared. The last 4 measurements in Figure 5.38 might be caused by another compound. This conclusion may be supported by the fact that the corresponding Γ_1 values of the last measurements (see Figure 5.35) are similar to the expected for the noncatalyzed Na_3AlH_6 at approximately the same temperature [8].

The double exponential behavior indicated an incomplete spatial averaging by spin diffusion [88], [89]. That the initial amplitude of the fast component became higher and higher seems to indicate that the spatial averaging is improved as a function of time, i.e., the distance between the moving and not moving vicinities should become shorter. By contrast, the reason of why the motional narrowing is not mediated is the distance between the moving and not moving vicinities.

5.4 Structural analysis of $NaAlH_4$ by NMR

The structure of $NaAlH_4$ determined in Ref. [25], [26] by X-ray, and the structure of $NaAlD_4$ determined by neutron scattering in Refs. [27] and [26] resulted in the same space group ($I41/a$), with only a change of 0.1 % of the lattice parameters for a Ti-doped $NaAlD_4$ sample. Ab initio calculations of the lattice parameters based on a generalized gradient approximation (GGA) were in good agreement with data obtained by Rietveld refinement of X-ray and neutron diffraction data [26]. GGA calculations yielded 1.631 Å for the Al–D bond length and 2.631 Å for the D–D distance within a tetrahedron. The corresponding value of the shortest distance between two deuterium atoms on adjacent tetrahedra was 2.680 Å.

As previously explained in Section 2.9.3, in the rigid lattice regime the linewidth is related to the second moment or to the inverse of the distance between the atoms to the power of six ($1/r^6$). Using the distances given in Ref. [26], we computed the second moment and their corresponding linewidths. The atoms taken into account were localized within a sphere of 8.0 Å radius. The center of the sphere is located at the hydrogen atom for which the powder second moment was calculated. The contributions of nuclei at a larger distance were estimated to be less than 1 % of the calculated values. All extra details related to how the second moment calculations were performed are presented in Section 4.2.3.

Using the van Vleck formulae (see Section 2.9.1), we obtained $M_{2,II} = 69.2 \times 10^8 \text{ Hz}^2$ and $M_{2,IS} = 55.7 \times 10^8 \text{ Hz}^2$. Therefrom the total second moment would be $M_{2,T} = 124.9 \times 10^8 \text{ Hz}^2$, which corresponds to a $\Delta\nu = 41.9 \text{ kHz}$ ¹⁰. A way to determine the linewidth (from the Gaussian approximation) and/or its corresponding second moment experimentally is to measure the decay of the FID (assuming a negligible field inhomogeneity) or, much better, of the second half of the MHE.

Ball-milled samples (without catalyst)

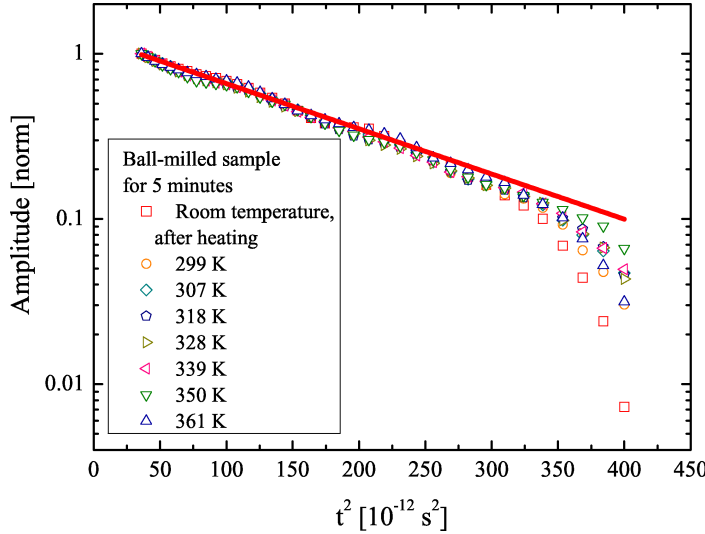


Figure 5.39: FIDs followed after a $\pi/2$ -pulse (with a dead time of $6 \mu\text{s}$) of the sample ball-milled for 5 minutes as a function of t^2 at diverse temperatures.

In Section 5.2.1 we found that the dominant part of the spectra of the untreated samples (without catalyst and not milled) does not change its linewidth as a function of temperature. Therefore, all spectra were in the rigid lattice regime and it is possible to analyze the decay of the FIDs as a function of temperature to find an approximation of the corresponding second moment M_2 , even if the FIDs had an experimental dead time of $6 \mu\text{s}$.

In Figure 5.39, the FIDs followed after a $\pi/2$ -pulse (with a dead time of $6 \mu\text{s}$) of the ball-milled sample for 5 minutes are shown as a function of t^2 at diverse temperatures. According with the decay of the FIDs, $M_2 = (126 \pm 4) \times 10^8 \text{ Hz}^2$. Using the Gaussian approximation (see Eq. 2.48), we find that $\Delta\nu = 42.1 \text{ kHz}$. **These data confirm the structure reported in the literature** in Ref. [26] and also by M. H. W. Verkuijlen *et al.* in Ref. [51].

¹⁰This value deviates from the linewidth obtained from the Gaussian approximation of the spectra ($\Delta\nu = 44.5 \text{ kHz}$) in Figure 5.8. These spectra were obtained after truncating after the first $23 \mu\text{s}$ the FIDs (taken from the second half of the MHEs). In this graph, the spectra of treated samples (ball-milled with catalyst) at 215 K overlaps with the one at room temperature as well as with spectra of the non-treated samples at room temperature. It should be considered though, that this method is not as precise since it depends on how well the center of the echo is determined.

Samples ball-milled together with catalyst

The spectra of the samples with catalyst in Section 5.2.1 were found to be composed by two **dominant lines** (broader components) plus a spike-like line (shown in Figure 5.14). The linewidths of those dominant lines do not change with increasing temperature, only their spectral weight. The widest dominant line was ascribed to the rigid lattice line and its amplitude becomes smaller at higher temperatures. As already discussed in Section 5.2.1, the spectra at the temperature range between room temperature (297 K) and 338 K consist mainly of the rigid lattice line (inspect the spectra in Figure 5.14 of the 1 mole % sample).

The corresponding FIDs of the previously mentioned spectra are shown in Figure 5.40. These FIDs followed after a $\pi/2$ -pulse applied on the 1 mole % sample (with a dead time of 6 μs). From the discussion in the last paragraph, we take the points overlapping in the FIDs between the temperatures 297 K up to 338 K, i.e., from $t = 6..16 \mu\text{s}$ (the first 6 μs were cut due to the experimental dead time). The points after 16 μs (for $t > 16 \mu\text{s}$) change even at temperatures below 338 K. So they do not represent the rigid lattice decay. From the first part of the FIDs, we obtain a $M_2 = (139 \pm 18) \times 10^8 \text{ Hz}^2$, which corresponds to a linewidth of 44.3 kHz.

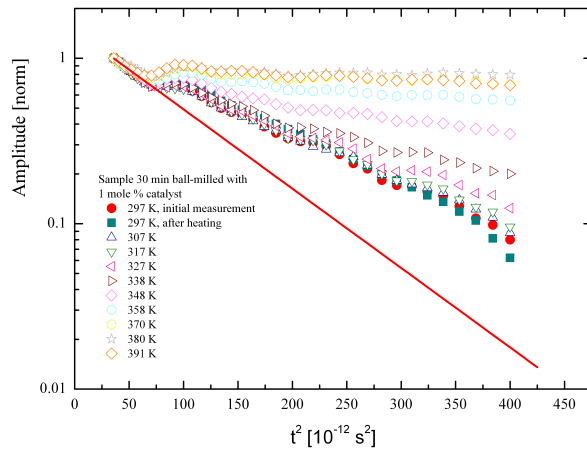


Figure 5.40: FIDs followed after a $\pi/2$ -pulse (with a dead time of 6 μs) of the 1 mole % sample as a function of t^2 at diverse temperatures.

The accuracy of the second moment M_2 deduced from the data shown in Figure 5.40 is, of course, rather limited. Within the experimental uncertainty, the results $M_2 = (139 \pm 18) \times 10^8 \text{ Hz}^2$ is even compatible with the value $M_2 = 124.9 \times 10^8 \text{ Hz}^2$ calculated for pure NaAlH_4 . However, in spite of its low accuracy, the value $M_2 = (139 \pm 18) \times 10^8 \text{ Hz}^2$ indicates a slightly larger second moment in the Ti-doped sample compared to M_2 of a pure sample. Such an increase in M_2 is expected due to the additional dipolar interactions between the magnetic moments of the protons and the titanium ions.

Proposed experimental method for determination of the homo- and heteronuclear second moment

All experimental details of this section are presented in Section 4.2.3. In addition a summary of the important parameters for the measurements and samples in this section is presented in Table 4.1.

In order to gain structural information of $NaAlH_4$, the different contributions to the dipolar second moment M_2 ($M_{2,II}$ and $M_{2,IS}$) have been obtained experimentally. As explained in Sect. 2.10, with the decay of the ME, MHE, and simple FID_{MHE} (2nd part of the MHE), it is possible to deduce each of the dipolar contributions, as well as the contributions due to experimental imperfections.

Ball-milled samples (without catalyst)

The plotted lines in Figure 5.41 show that all initial decays can be well fitted to a Gaussian ($y = A \exp(-\frac{M_2}{2}\tau^2)$). By fitting the decay of the MHE versus the evolution time (in this case t^* is 6τ), we obtain $M_{2,MHE}$. A weak dependence of the echo amplitude on the spin-evolution time is expected, as both homonuclear and heteronuclear dipolar interactions should be refocused. This second moment is equivalent to ϵ_0 in Eq. (2.51) and indicates the decay given by the experimental imperfections.

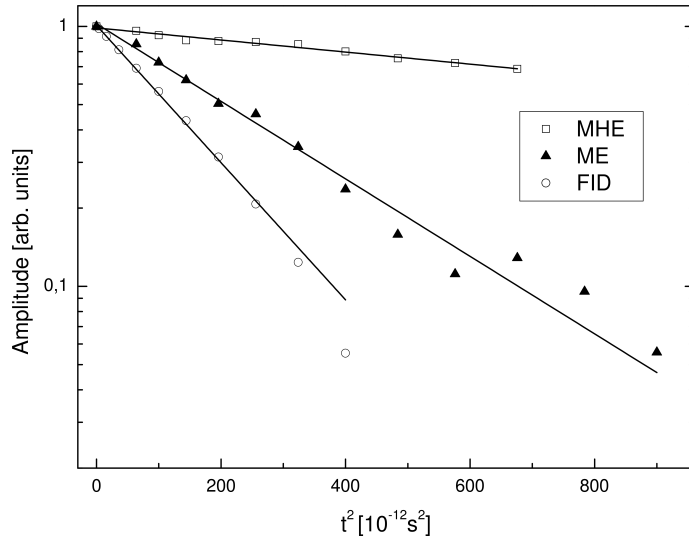


Figure 5.41: Decay of a MHE, ME, and the FID of a sample ball-milled but without catalyst.

The decay of the ME in Figure 5.41 as a function of t^2 of a ball-milled sample without catalyst, subtracting ϵ_0 gives rise to $M_{2,IS} = (58.5 \pm 5.0) \times 10^8 \text{ Hz}^2$. Furthermore, from the obtained decay of the second half of the magic echo (FID) a total second moment $M_2 = (125 \pm 3) \times 10^8$ is deduced. Subtracting now ϵ_0 and $M_{2,IS}$ from $M_2 = (125 \pm 3) \times 10^8 \text{ Hz}^2$, we obtain $M_{2,II} = (66.5 \pm 8.0) \times 10^8 \text{ Hz}^2$.

The experimental result $M_2 = (125 \pm 3) \times 10^8 \text{ Hz}^2$ is in excellent agreement with $M_2 = 124.9 \pm 3 \times 10^8 \text{ Hz}^2$, as calculated for the published structure of $NaAlH_4$ using the van Vleck formulae. It is also consistent with $M_2 = 126 \pm 4 \times 10^8 \text{ Hz}^2$ as deduced from the

decay of the FID (see Figure 5.39). These data thus confirm the correctness of the structure of NaAlH_4 published in Refs. [25], [26], and [27].

Samples ball-milled together with catalyst

Figure 5.42 shows the decay of a MHE and FID_{MHE} (the 2nd half of a MHE) of the second 2 mole % sample (sample ball-milled with 2 mole % $\text{Ti}_{13} \cdot 6\text{THF}$ catalyst). With this sample, the decay of the MHE results into a $\epsilon_0 = 1.1 \times 10^8 \text{ Hz}^2$. Furthermore, the fit of the initial slope of the FID (taking the first $13 \mu\text{s}$ into account) removing the experimental imperfections (ϵ_0) results in a total second moment of $(142 \pm 2) \times 10^8 \text{ Hz}^2$. According to Eq. (2.48), the linewidth estimated from this value is 44.7 kHz.

The initial decays of the FID_{MHE} as well as of the ‘normal’ FIDs (followed after a $\pi/2$ -pulse) correspond to the broad part of the spectra discussed in Section 5.2.1.

The total second moment $M_2 = (142 \pm 2) \times 10^8 \text{ Hz}^2$ calculated from the initial decay of the FID_{MHE} is consistent with $M_2 = (139 \pm 18) \times 10^8 \text{ Hz}^2$ deduced from the FIDs shown in Figure (5.40). Those second moments correspond to a $\Delta\nu = 44.7$ and 44.2 kHz, respectively, which are about 5 % larger than the value obtained for pure NaAlH_4 . Such an increment can be explained by the admixture of Ti results in an increase in the second moment of the doped samples due to the additional dipolar interactions with titanium ions.

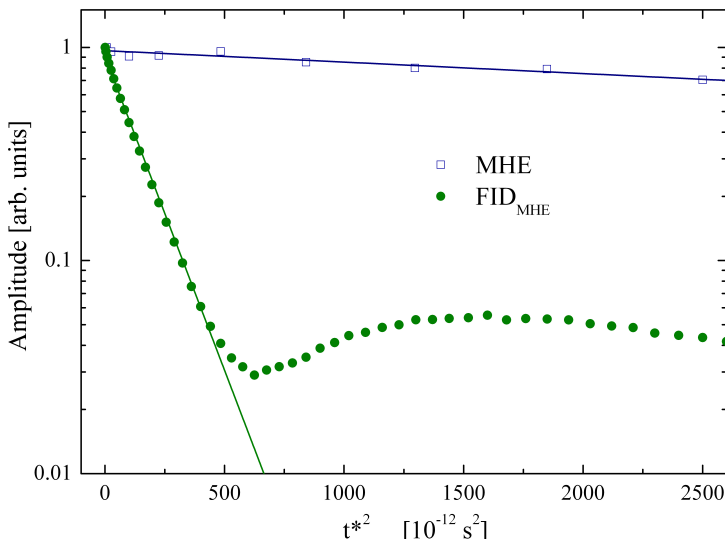


Figure 5.42: Decay of a MHE and the FID of a 2 mole % sample [94], [95].

6 Summary and Conclusions

In order to be able to use alanates as hydrogen storage material it is necessary to know how the hydrogen atoms behave during loading, discharge and reloading of differently treated materials. This $^1\text{H-NMR}$ study was conducted to know how the hydrogen discharge depends on the treatment of the samples. In order to achieve this goal, two kinds of samples were produced with purified sodium alanate (NaAlH_4). The first kind of samples was prepared by ball-milling NaAlH_4 crystals for 5 minutes, 30 minutes and 12 hours (each milling time was divided in periods of 15 minutes with pauses in between of 30 minutes). The samples prepared in this way were designated as **ball-milled samples**. The second kind of samples was obtained by ball-milling NaAlH_4 crystals for 30 minutes along with 1, 2, or 5 mole % of Ti clusters ($\text{Ti}_{13} \cdot 6\text{THF}$). This type of samples was denoted as **Ti catalyst doped samples**, and (in specific depending on the catalyst proportion used) as **1-, 2-, or 5-mole % sample**.

Spin-lattice relaxation rates and spectra are usually mediated by motional processes like e.g. lattice vibrations or diffusion of particles. To get a better understanding of the hydrogen desorption process and of the hydrogen dynamics, measurements of the $^1\text{H-NMR}$ spectra and spin-lattice relaxation rates (Γ_1) were performed on both kinds of samples as a function of temperature. The range of temperatures used went from room temperature up to about 360 K (the specific temperature ranges are summarized in Tables 4.2 and 4.3). Measurements at lower temperatures (below room temperature down to 260 K) were only carried out on the 2-mole % sample.

In order to explicitly investigate the hydrogen desorption from catalyzed samples at constant temperature, $^1\text{H-NMR}$ spectra and spin-lattice relaxation rates (Γ_1) were measured **as a function of time**. The time was measured from the initial measurement. All specifications of these measurements are summarized in Table 4.4.

In addition, a structural analysis of NaAlH_4 by $^1\text{H-NMR}$ was done.

Main results

The $^1\text{H-NMR}$ linewidth of NaAlH_4 at low temperature – obtained from the initial decay of the FID as a function of t^2 at the rigid lattice limit – confirmed the structure of NaAlH_4 proposed in the literature [25], [26], [27]. The determination of the hydrogen location in NaAlH_4 had only been done prior to this work by neutron scattering. This implicitly implies that the neutron scattering experiments were performed on NaAlD_4 (not in NaAlH_4). To test if the structure of NaAlH_4 itself is in agreement with that of NaAlD_4 , the homo- and heteronuclear contributions

to the linewidth were measured independently. The experimental data – obtained by combination of the Magic Echo (ME) and Magic Hahn Echo (MHE) sequences – corroborated the structure of $NaAlH_4$. The admixture of Ti catalyst resulted in an increase of the linewidth (of about 5 %) due to additional dipolar interaction of protons with Ti ions.

The spectral line characteristics of Na_3AlH_6 [8] and $NaAlH_4$ indicated that during ball milling process, the samples of $NaAlH_4$ might have already partially decomposed into Na_3AlH_6 (i.e., hydrogen on the sample may have partially been desorbed). Approximately 20 % of a sample without catalyst decomposed after a total of 12 hours ball milling. Comparatively, in the 5-mole % sample also about 20 % decomposed but only after 30 minutes of ball milling.

The hydrogen content of each component of the samples was inferred from their corresponding spectral weights, i.e., the normalized areas under the fitted lines to the experimental spectra. The normalization was done dividing by the sum of the areas. Those measurements reveal a slightly different **onset temperature** of hydrogen release depending on the catalyst proportion. Accordingly with the spectral weights obtained by the three-component fits, hydrogen atoms start to desorb at approximately **340 K, 330 K and 320 K** for the 1-, 2- and 5-mole % samples, respectively.

In addition to the effect related to hydrogen desorption, the 1H -NMR spectra of Ti catalyst doped samples showed a motion induced narrowing as a function of temperature. The linewidths at temperatures higher than approximately 340 K, plotted as a function of temperature, give rise to a plateau. A thermally activated rapid rotation of AlH_4 tetrahedra around their C_3 symmetry axis explained consistently that plateau. The temperatures, at which the transition from rigid lattice behavior to motional narrowing took place, concurred with the onset temperatures of the hydrogen release.

A more detailed analysis of the spectra revealed the coexistence of motional narrowing and rigid lattice regimes within the same spectrum. That coexistence implied that motional narrowing was heterogeneous over the sample. Narrowing in different spatial regions of the sample might, therefore, be characterized by different average distances to Ti-catalyst. Samples with more catalyst would thus have more atoms near catalyst, and slightly lower onset temperatures. The activation energies associated with rotations of AlH_4 tetrahedra might be presumably substantially higher than the obtained values ($H_a \approx 200$ meV, 240 meV, 260 meV for 1-, 2- and 5-mole % sample, respectively).

No partial motional narrowing was observed on any of the samples without catalyst. In those samples, despite of their heterogeneity, only one relaxation rate (Γ_1) could be detected. This fact can be explained if the relaxation took place indirectly via spin diffusion between the so-called surfaces¹ and the atoms of the bulk. Also due to spin diffusion the activation energies found were nearly negligible ($H_a \approx 56$ meV, 56 meV, 78 meV for the samples ball milled for 5 minutes, 30 minutes and 12 hours, respectively). These activation energies might be associated only with fractions of the activation enthalpies of hydrogen motion in the vicinities of surfaces or interfaces.

¹ “Surfaces” were defined as the grain surfaces and the internal interfaces. In the jargon of spin diffusion, those “surfaces” are the relaxation centers.

A double-exponential had to be used to describe all relaxation data of the Ti catalyst doped samples. The high (Γ_{11}) and a low relaxation rate (Γ_{12}) were called *fast* and *slow component*, respectively. The relaxation rates (as well as their corresponding activation energies) of samples with no catalyst were practically identical with the *slow component*, Γ_{12} . Therefore, Γ_{12} was associated with relaxation taking place indirectly via spin diffusion between the so-called surfaces (not charged with catalyst) and the atoms of the bulk.

The *fast relaxation component* (Γ_{11}) was related to the influence of the catalyst in the sample by simple exclusion. Relaxation of the *fast component* (Γ_{11}) took place indirectly via spin diffusion below the onset temperatures, as in the samples just ball-milled. However, in this time the spin diffusion took place between the so-called surfaces charged with catalyst and the atoms in the bulk. Above the onset temperatures, the *fast component* showed stronger temperature dependence ($H_a \approx 770$ meV, 410 meV, 370 meV for 1-, 2-, 5-mole % samples, respectively). Those dependences might be related to hydrogen motion accelerated by the presence of catalyst. Thus, the above given interpretation is consistent with the before mentioned partial motional line narrowing (observed in $^1\text{H-NMR}$ spectra starting also around onset temperatures).

The dynamics of hydrogen desorption was also analyzed by using measurements of NMR spectra and Γ_1 rates on the Ti catalyst doped samples at a constant temperature. Strong changes were observed on the shape of the NMR spectrum when measured on the 1 mole % sample over a time period of 900 minutes at 336 K. A spectrum, observed after 900 minutes at 336 K, consisted of a single line with a linewidth of approximately 17 kHz. Decomposition reduces the total hydrogen content at the sample (and thus total spectral area). A detailed analysis of the spectral area though showed that after 570 minutes only 10 % of the hydrogen content was desorbed, i.e., about 20 % of NaAlH_4 transformed into Na_3AlH_6 . Therefore the shape of that spectrum alone did not provide enough evidence to distinguish between decomposition into Na_3AlH_6 and e.g. rotation of AlH_4 tetrahedra around their C_3 -axis in NaAlH_4 .

The *slow relaxation component* (Γ_{12}) at constant temperature showed almost no time dependence (similar to the measurements as a function of temperature). Whereas the *fast component* (Γ_{11}) increased its value as a function of time in a form which seemed to be asymptotical to a value around 3 1/s. The hydrogen desorbed (estimated from the total amplitude of the Γ_1 measurements) was approximately the same value as the estimated from the spectra measured also at constant temperature.

The changes between the amplitudes from the *slow* and *fast components* were stronger than expected, if hydrogen desorption would be the only process happening within the sample. A possible explanation is that at elevated temperatures, partial decomposition of Ti catalyst doped samples are under formation of Na_3AlH_6 and metallic Al . This might give rise to structural defects in the remaining NaAlH_4 and reduction of the energy barrier for e.g. rotation of the AlH_4 tetrahedra around their C_3 -axis in NaAlH_4 . These phenomena would give rise to an increase on amplitude of the *fast component* Γ_{11} and aid the already mentioned fast rotation of the AlH_4 tetrahedra.

7 Resümee und Zusammenfassung

Wasserstoff kann sich zu einem hervorragenden Brennstoff entwickeln, wenn es gelingt, ihn umweltfreundlich herzustellen und geeignete Materialien zu finden, um ihn sicher und effizient zu speichern. In der vorliegenden Arbeit wurde das **komplexe chemische Hydrid Natriumalanat** ($NaAlH_4$) untersucht, welches von großem Interesse für die Entwicklung eines Wasserstoffspeichers ist. Dieses Material weist eine relativ große Speicherkapazität für Wasserstoff auf.

Die thermische Zersetzung von $NaAlH_4$ und damit die Freisetzung von Wasserstoff erfolgt in drei Stufen. In jeder Stufe findet eine Phasenumwandlung statt: $NaAlH_4$ wandeln sich hauptsächlich zu Natrium-Aluminium-Hexahydrid – Na_3AlH_6 (Gleichung (1.1)), und Na_3AlH_6 zu NaH um, das wiederum zu Al und H (Gleichung (1.3)) aufgespalten werden kann. Während der ersten zwei Reaktionen setzen $NaAlH_4$ und Na_3AlH_6 insgesamt 5.6 Gew. % Wasserstoff frei. Da NaH ein sehr stabiles Material ist, sind Temperaturen über 697 K erforderlich, um auch noch den Wasserstoff dieser Verbindung freizusetzen [9]. Deswegen wurde die dritte Reaktion für eine praktische Umsetzung nicht weiter in Betracht gezogen. Die **verfügbare Kapazität** bleibt somit bei 5.6 Gew. %.

$NaAlH_4$ besitzt eine tetragonale Kristallstruktur mit den Gitterparametern $a = 5.0119(1)$ Å und $c = 11.3147(5)$ Å. Die zugehörige Raumgruppe ist $I4_1/a$ [24], [25], [26]. Die Struktur wurde durch eine Rietveldverfeinerung der an $NaAlD_4$ Pulverproben gemessenen Neutronenstreudaten bestimmt [27], [26]. Um jedes Aluminium-Atom sind vier Deuterium-Atome gelagert, die einen Tetraeder ausbilden. Man nimmt an, dass die Wasserstoff-Atome in $NaAlH_4$ dieselben Positionen besetzen wie die Deuterium-Atome in $NaAlD_4$. Die Struktur von Na_3AlH_6 (zweite Phasenumwandlung von $NaAlH_4$) ist in Abb. 1.6 dargestellt. Für dieses Material sind die Wasserstoff-Atome in einer Oktaeder-Struktur um die Al -Atome angeordnet. Die Gitter-Parameter sind $a = 5.408(2)$, $b = 5.538(2)$, $c = 7.757(2)$ Å und $\beta = 89.83(2)^\circ$. Die Positionen der Wasserstoff-Atome wurden aus den Positionen einer deuterierten Probe Na_3AlD_6 [13] hergeleitet. Die Struktur hat eine $P2_1/n$ Raumgruppe. Die Oktaeder sind deformiert mit Abständen 1.746, 1.758 und 1.770 Å und ein wenig gekippt (die Winkelgröße wurde durch E. Rönnebro *et al* [28] nicht eindeutig bestimmt).

Trotz etlicher Vorteile der $NaAlH_4$ Proben (sie sind zudem preiswert und die Speicherung des Wasserstoffs kann ohne Druck erfolgen) wurden sie erst 1997 als geeignetes Speichermaterial

in Betracht gezogen, als Bogdanović und Schwickardi [12] zum ersten Mal einen *Ti*-basierten Katalysator verwendeten. Erst durch die Verwendung des Katalysators wird die energetische Barriere zur Freisetzung von Wasserstoff so weit reduziert, dass die Desorption des Wasserstoffs bereits bei moderaten Temperaturen einsetzt. Der Prozess der Wasserstoff-Desorption wird durch den Katalysator reversibel, wodurch das System für die Entwicklung eines Speichers interessant wird¹. In dieser Arbeit wurde als Katalysator ausschließlich $\text{Ti}_{13} \cdot 6\text{THF}$ verwendet, da es sich hierbei um den effektivsten Katalysator hinsichtlich der Desorption und Absorption des Wasserstoffs handelt [36], [37]. Die Frage, auf welche Weise sich der Wasserstoff aufgrund des Katalysators besser lösen kann, konnte bis jetzt noch nicht umfassend geklärt werden.

Ziel der Arbeit

Um Alanate als Wasserstoffspeicher nutzen zu können, ist es notwendig zu wissen, wie sich die Wasserstoff-Atome in unterschiedlich behandelten Materialien bei „Auf-, Be- und Entladungs-Prozessen“ verhalten. Diese $^1\text{H-NMR}$ -Studie wurde durchgeführt, um die Wasserstoff-Entladung in Abhängigkeit von der Behandlung der Probe zu untersuchen. Dafür wurden zwei Arten von Proben mit gereinigtem Natriumalanat (NaAlH_4) hergestellt. Die erste umfasst Proben ohne Katalysator, die 5 Minuten, 30 Minuten und in einem Fall auch 12 Stunden gemahlen wurden. Die Proben, die auf diese Weise hergestellt wurden, wurden als **kugelgemahlene Proben** bezeichnet. Eine zweite Probenart besteht aus Proben die 30 Minuten mit 1, 2, oder 5 Mol% $\text{Ti}_{13} \cdot 6\text{THF}$ Katalysator gemahlen wurden. Diese Art von Proben wurde als **Ti-Katalysator dotierte Proben** bezeichnet, und je nach verwendetem Katalysatoranteil als **1, 2, oder 5 Mol% Probe**.

Die Spin-Gitter-Relaxationen und die Spektren hängen in der Regel von Bewegungsprozessen wie z. B. Gittervibrationen oder der Diffusion von Teilchen ab. Um ein besseres Verständnis der Wasserstoff-Desorption und der Wasserstoff-Dynamik zu erhalten, wurden Messungen der $^1\text{H-NMR}$ -Spektren und der Spin-Gitter-Relaxationen (Γ_1) an beiden Arten von Proben **als Funktion der Temperatur** durchgeführt. Die verwendeten Temperaturen gingen von Raumtemperatur bis zu etwa 360 K (die Temperaturbereiche wurden in den Tabellen 4.2 und 4.3 zusammengefasst). Messungen bei tieferen Temperaturen (unterhalb der Raumtemperatur bis zu 260 K) wurden nur an der 2 Mol% Probe durchgeführt.

Um die Wasserstoff-Desorption von katalysierten Proben bei konstanter Temperatur zu untersuchen, wurden $^1\text{H-NMR}$ -Spektren und Spin-Gitter-Relaxationen (Γ_1) **als Funktion der Zeit** gemessen. Die Zeit wurde von der ersten Messung an gemessen. Alle technischen Angaben dieser Messungen sind im Tabelle 4.4 zusammengefasst.

Zudem wurde auch mit $^1\text{H-NMR}$ die Struktur von NaAlH_4 mit und ohne Katalysator mit Hilfe verschiedener Methoden der Kernspinresonanz (*NMR*) analysiert.

¹Die Beladungs- und Entladungs-Prozesse des Wasserstoffs sind reversibel, jedoch nicht ausreichend stabil, d. h., ein Teil der *H*-Speicherkapazität geht schon nach einigen Zyklen verloren.

7.1 Notwendige NMR-Theorie

Bei Kernspins, die nicht gleich null sind, sind die magnetischen Momente direkt proportional. Für Protonen mit $I = \pm 1/2$ hat man zwei verschiedene Orientierungen, die entsprechend ein niedrigeres oder höheres Energieniveau haben. Wenn die Spins in ein Magnetfeld eingelegt sind, weist das energetisch tiefer-liegende Niveau im thermodynamischen Gleichgewicht eine höhere Besetzung auf, was eine makroskopische Kernmagnetisierung zur Folge hat. Bei der NMR-Spektroskopie werden durch Hochfrequenzpulse (HF-Pulse) Übergänge zwischen diesen Energieniveaus induziert, wobei die Gesamt magnetisierung der Probe gedreht wird. Die Pulslänge ist proportional zum Drehwinkel der Magnetisierung. Daher spricht man von einem π -Puls, wenn die Magnetisierung invertiert wird.

Für ^1H -NMR-Messungen in Festkörpern spielt die direkte dipolare Wechselwirkung zwischen den Kernspins die wichtigste Rolle. Zwischen identischen oder unterschiedlichen Arten von Kernen spricht man entweder von homo- oder heteronuklearen Wechselwirkungen.

NMR-Spektren

Nach einem $\pi/2$ -Puls führt die Kernmagnetisierung eine freie Präzession durch, bis sie wieder in das Gleichgewicht zurückrelaxiert. Diese Präzession verursacht ein messbares Induktionssignal, genannt *Free Induction Decay (FID)*. Die NMR-Spektren werden üblicherweise durch Fourier-Transformation der FID Signale erhalten².

Häufig werden die Tief temperaturspektren durch die Methode der Momentenentwicklungen von van Vleck [73] näherungsweise beschrieben. Die FID Funktion kann gewöhnlich in Resonanz durch $G_x(t) = \exp(-\frac{1}{2}M_2t^2)$ beschrieben werden, wobei M_2 dem zweiten Moment der van Vleck Näherung entspricht [73], [74]. Wenn man die Struktur kennt, kann man M_2 berechnen und z. B. die Linienbreite der Spektren abschätzen.

Wenn die Temperatur hoch genug ist, kommt es zu einer Bewegung der Kernspins, was die dipolare Wechselwirkung zumindest teilweise ausmittelt. Dieser Effekt verursacht eine Verlängerung des FIDs und damit eine Abnahme der NMR-Linienbreite. Im Fall von Na_3AlH_6 wurde M_2 unter Berücksichtigung möglicher Rotationen der AlH_6 Oktaeder rund um ihre unterschiedlichen Symmetrieachsen berechnet [49], [51]. Diese Abnahme der NMR-Linienbreite wurde hier „unvollständige bewegungsinduzierte Linienverschmälerung“ genannt.

Abschätzung der Abstände durch das *Magic* sowie das *Magic-Hahn* Echo

Die unabhängige Messung vom homo- und heteronuklearen Beiträge zur Linienbreite liefert einen Nachweis, ob die für NaAlD_4 gefundene Struktur mit der von NaAlH_4 übereinstimmt. Um die starke homonukleare Wechselwirkung zu refokussieren, haben wir die *Magic Echo (ME)* Puls Sequenz angewandt [62], [63], [66]. Die von uns benutzte Variation ist schematisch in Abb. 2.8 dargestellt [59]. Diese ME Sequenz besteht aus einem $(\pi/2)_x$ -Puls sowie einem so genannten *Magic Sandwich*

²Man kann auch die Hälfte eines Echos benutzen, um die Spektren zu erhalten. Das wird angewandt, um experimentelle „Totzeiten“ zu umgehen.

$[(\pi/2)_y - (\alpha)_x - (\alpha)_{-x} - (\pi/2)_{-y}]$. Der komplette dipolare Hamilton-Operator ist während des *Magic Sandwichs* nur durch eine Hälfte des homonuklearen Hamilton-Operators gegeben ($-\frac{1}{2}H_{II}$), d. h., der heteronukleare Hamilton-Operator löst sich während des *Magic Sandwichs* auf. Dadurch werden beim *ME* die homonuklearen Wechselwirkungen kompensiert, wenn die Evolutionszeit innerhalb und außerhalb des *Magic Sandwichs* dem Verhältnis 2 : 1 entspricht.

Das klassische Hahn Echo [61] refokussiert die Dephasierung der heteronuklearen Wechselwirkung. Um das *ME* und die Hahn Puls-Sequenz zu kombinieren, muss ein π -Puls in die *ME* Sequenz eingefügt oder die Phase des $(\pi/2)$ Pulses am Ende des *Magic Sandwichs* [61], [64] invertiert werden. Die Form des *Magic-Hahn Echos* ist damit der Form des „normalen“ *ME* sehr ähnlich. Der einzige Unterschied besteht darin, dass der letzte Puls gleich $(\pi/2)_y$ ist, der eine positive Phase hat. Mit dieser Puls-Sequenz kann man jedoch sowohl die homonuklearen, als auch die heteronuklearen Wechselwirkungen refokussieren.

Die dipolare Wechselwirkung zwischen den Kernspins einer Probe ist umgekehrt proportional zu der sechsten Potenz des Abstands zwischen den Kernen. Wird die dipolare Wechselwirkung mit der *NMR* gemessen, beispielsweise durch Bestimmung des zweiten Moments M_2 , kann damit der Abstand zwischen den Kernen abgeschätzt werden.

Bei einem gaußförmigen *NMR*-Signal kann der freie Induktionszerfall (*FID*) durch die Funktion $G_{FID} = G_1 \exp((M_2 + \epsilon_0)t^2/2)$ beschrieben werden. Hierbei ist M_2 das gesamte zweite Moment des Spinsystems ($M_2 = M_{2,II} + M_{2,IS}$) und ϵ_0 repräsentiert eine zusätzliche geringe Abnahme des *NMR*-Signals infolge möglicherweise vorhandener Inhomogenitäten. Aus dem Zerfall des *FIDs* sowie des *MEs* und des *MHEs* als Funktion der entsprechenden Spin-Evolutionszeiten lassen sich das gesamte zweite Moment und die hetero- und homonuklearen Beiträge bestimmen.

Relaxation

Wenn das thermische Gleichgewicht des Spin-Systems gestört ist (z. B. durch die Anwendung eines *HF* Pulses), nähert sich die Magnetisierung nach dieser Störung wieder exponentiell ihrem Gleichgewichtszustand. Die Spin - Gitter Relaxationszeit oder auch longitudinale Relaxationszeit ($T_1 = 1/\Gamma_1$) ist die charakteristische Zeit, um das thermische Gleichgewicht nach einem HF-Puls zu erreichen. Dieser Relaxationsprozess erfordert einen Energie-Austausch zwischen dem Spin-System und dem Gitter. Der Verlust der Phasenkohärenz zwischen den Spins in der xy -Ebene – senkrecht zum stationären Magnetfeld B_0 – erfolgt mit der transversalen Relaxationszeit oder Spin-Spin-Relaxationszeit (T_2).

Experimentell wird Γ_1 beispielsweise mithilfe einer Inversionserholung bestimmt (Abb. 2.9). Die zugehörige Puls-Sequenz besteht aus einem π -Puls gefolgt von einem $\pi/2$ -Puls. Der erste Puls invertiert \mathcal{M} . In der Zeit zwischen den Pulsen nähert sich das System dem Gleichgewichtszustand wieder an. Der zweite Puls wird angewandt, um den Zustand der Magnetisierung zu detektieren. Die gleiche Messung wird mehrere Male wiederholt, während die Zeit zwischen den Pulsen (τ) erhöht wird.

Die Spin-Gitter-Relaxation entsteht in der Regel im Zusammenhang mit molekularen Bewegungsprozessen, Diffusion von Partikeln oder Gitterschwingungen. Dynamische Prozesse

in Festkörpern führen zu einer Modulation der dipolaren Wechselwirkung und somit zu einer Spin-Gitter-Relaxation. Ein Bewegungsinduzierterprozess wurde durch die Frequenz ν charakterisiert. Eine solche Frequenz ist bei der Wahrscheinlichkeit gegeben, dass ein Partikel genug Thermal-Energie besitzt, um die Energiebarriere zu überwinden. Ein einzelner thermisch aktiver Bewegungsprozess (mit einer Sprungfrequenz ν) folgt in vielen Fällen einer Arrhenius-Gleichung, $\nu^* = \nu_p \exp(-H_a/k_B T)$, wo H_a die Aktivierungsenthalpie und ν_p normalerweise eine Schwingungsfrequenz des Ions um seine Gleichgewichtsposition ist. Die charakteristische Zeit für die Änderung der dipolaren Wechselwirkung ist andererseits durch die sogenannte Korrelationszeit, τ_c , charakterisiert. Gemäß dem BPP-Relaxationsmodell [76] wird bei der höheren Temperatur-Grenze ($\omega_0 \cdot \tau_c \ll 1$) eine Relaxationsrate Γ_1 erwartet, die proportional zu τ_c und $\exp(H_a/k_B T)$ ist (s. Gl. (2.53)), während bei der tiefen Temperatur-Grenze ($\omega_0 \cdot \tau_c \gg 1$) die Relaxationsrate proportional zu $1/(\tau_c \omega_0^2)$ und $\exp(-H_a/k_B T)$ sein soll (s. Gl. (2.54)). Wenn τ_c dem Kehrwert der *NMR*-Frequenz ω_0 entspricht, d.h. wenn die Bedingung $\omega_0 \cdot \tau_c \simeq 1$ erfüllt ist, dann kann τ_c abgeschätzt werden (s. Abb. 2.14).

7.2 Experimentelle Grundlagen

Die Proben wurden bei Dr. Maximilian Fichtner vom Karlsruhe Research Centre hergestellt. Die Synthese der $NaAlH_4$ und Na_3AlH_6 Proben ist in Ref. [36] beschrieben. Die NaH Probe wurde durch Kugelmahlen von gereinigtem $NaAlH_4$ und anschließender thermischer Desorption unter Vakuum bei 443 K erhalten.

Die Proben wurden kugelmahlen, um eine bessere Verteilung des Katalysators zu erreichen. Beim Kugelmahlen wurden aber auch Fehlstellen in das Material eingebracht, und zudem die Größe der kristallinen Körner verringert, was bereits zu einer Reduktion der Desorptionstemperatur führt (das Verhältnis zwischen Oberfläche und Volumen nimmt zu und der Wasserstoff wird aus der Oberfläche desorbiert [9]). Die Kinematik der Wasserstoff-Desorption wurde den Fakten zufolge verbessern.

Das Kugelmahlen der Proben wurde in einem Mahlbecher (Abb.4.2(a)) aus Siliziumnitrid durchgeführt, um magnetische Verunreinigungen der Probe weitestgehend zu vermeiden. Dafür wurde der Katalysator zusammen mit dem Material unter inerten Bedingungen (in einer Ar-gefüllten Handschuhbox)³ in den Mahlbecher eingefüllt. Der Mahlbecher wurde anschließend versiegelt und in eine Fritsch P6 Planeten-Mühle (vgl. Abb. 4.2(b)) eingesetzt. Alle behandelte Proben wurden bei 600 Umdrehungen pro Minute und in Intervallen von 15 Minuten (mit Zwischenpausen von 10 Minuten) gemahlen.

Einzelheiten des experimentellen Versuchsaufbaus

Die *NMR*-Experimente wurden an zwei unterschiedlichen Spektrometern durchgeführt. Für Messungen der Spin-Gitter-Relaxation sowie für Untersuchungen der Wasserstoff-Desorption anhand der *NMR*-Spektren wurde hauptsächlich ein Eigenbau-Spektrometer verwendet. Dieses

³ $NaAlH_4$ ist sehr reaktiv mit Sauerstoff und Luftfeuchtigkeit [78].

Spektrometer hatte eine Protonen-Resonanzfrequenz von 67.7 MHz und die Länge des $\pi/2$ -Pulses betrug $2.1 \mu s$. Die *ME* und *MHE* Messungen erfolgten mit einem Bruker CXP 300 Spektrometer welche eine Protonen-Resonanzfrequenz von 301.7 MHz und einer $\pi/2$ -Pulslänge von $2.7 \mu s$ hatte. Die Länge der *ME Sandwiches* wurde zwischen 1.25 und $25 \mu s$ variiert. Die *NMR*-Spektren wurden jeweils mittels Fourier-Transformation der freien Induktionszerfälle oder der zweiten Hälfte der *MEs* oder *MHEs* erhalten.

Die Probenbehälter für die *NMR*-Messungen waren aus Teflon gefertigt, um dem desorbierten Wasserstoff aus dem Innern das Herausdiffundieren zu ermöglichen. Es wurde sichergestellt, dass sich die Proben auch während der *NMR*-Messungen in einer inerten Atmosphäre befanden. Hierzu wurde die Raumtemperaturbohrung des supraleitenden Magneten zunächst evakuiert und anschließend mit Stickstoff geflutet.

Messungen zur Untersuchung der Struktur

Die Untersuchungen der $NaAlH_4$ Struktur wurden an einer nur kugelgemahlenen Probe (ohne Katalysator) und an einer 2 Mol% Probe durchgeführt.

Die mit der *ME* und *MHE* Pulssequenz gemessenen Echos wurden im Zeitraum aufgenommen und die zweite Hälfte der Echos im Anschluss Fourier transformiert. Die Echoamplituden ergaben sich dann durch Integration über die Spektren im Frequenzraum. Wie in Abb. 5.7 dargestellt, bestehen die Spektren häufig aus einer breiten Linie, die von einer schmalen zentralen Linie überlagert ist. Diese schmale Linie kann Na_3AlH_6 zugeordnet werden, das sich durch teilweises Zersetzen der Probe gebildet hat. Dieser Anteil wurde vor einer weiteren Auswertung der Daten abgetrennt.

Berechnung des zweiten Moments

Um das zweite Moment zu berechnen, wurde die von V. Ozolins *et al* [26] vorgeschlagene Kristallstruktur für alle Atome verwendet, deren Abstand von einem gegebenen Wasserstoff-Atom eine Distanz maximal 8.0 Å besitzt. Die Beiträge für das zweite Moment von den Kernen mit größeren Abständen wurden auf weniger als 1 % geschätzt. Die Abstände wurden bei Dr. Ivan Halasz mit dem Programm Diamond Version 3.1f, Crystal Impact, 2008 bestimmt.

7.3 NMR Messungen – Ergebnisse

NMR Spektren – Strukturanalyse von $NaAlH_4$

Bei niedriger Temperatur im Bereich der dipolaren Linienverbreitung (*rigid lattice regime*) erhält man – aus dem Zerfall des ersten Teils des *FIDs* als Funktion von t^2 – die „absolute“ $^1\text{H-NMR}$ Linienbreite. Die so erhaltenen Linienbreiten stützen die in der Literatur vorgeschlagene Struktur von $NaAlH_4$ [25], [26], [27].

Die experimentellen Daten der Struktur aus den homo- und heteronuklearen Beiträgen zu den Linienbreiten bestätigen auch die oben angegebene Struktur von $NaAlH_4$. Die Beimischung von

$Ti_{13} \cdot 6THF$ Katalysator hat einen Anstieg der Linienbreite (von etwa 5 %) zur Folge. Der Anstieg wurde durch zusätzliche Dipol-Wechselwirkung von Protonen mit Ti-Ionen erklärt.

Wasserstoffdynamik

Die **spektralen Eigenschaften** von Na_3AlH_6 [8] und $NaAlH_4$ deuten an, dass bereits während des Kugelmahlens die $NaAlH_4$ Proben teilweise in Na_3AlH_6 zersetzt worden sind (d. h., Wasserstoff in der Probe könnte teilweise desorbiert worden sein). Eine Probe ohne Katalysator hatte nach insgesamt 12 Stunden Kugelmahlen etwa 20 % verloren. Zum Vergleich: die 5 Mol% Probe hatte auch etwa 20 % verloren, aber schon nach 30 Minuten Kugelmahlen.

Der Wasserstoff-Gehalt von jeder einzelnen Komponente in den Proben wurde aus der entsprechenden Spektraldichte (aus den normierten Flächen unter den angepassten Linien der gemessenen Spektren) geschätzt. Die Normierung wurde durch die Summe der Anfangsflächen erhalten. Diese Messungen zeigten eine etwas andere **Anfangstemperatur** der Wasserstoff-Freisetzung abhängig vom Katalysatoranteil. Bei den Proben mit 1, 2, und 5 Mol% Katalysator beginnt die Wasserstoffdesorption bei ca. **340, 330 bzw. 320 K**.

Zusätzlich zum Effekt der Wasserstoff-Desorption zeigten die 1H -NMR-Spektren von Ti dotierten Proben eine bewegungsinduzierte Linienverschmälerung in Abhängigkeit von der Temperatur. Die Linienbreiten bildeten ein Plateau bei Temperaturen höher als etwa 340 K. Eine thermisch aktivierte schnelle Rotation des AlH_4 Tetraeders um seine C_3 Symmetrieachse erklärt das Plateau. Die Temperaturübergänge vom Bereich der dipolaren Linienverbreiterungen zu den bewegungsinduzierten Linienverschmälerung Regimen stimmt mit den *Anfangstemperaturen* der Freisetzung von Wasserstoff überein.

Eine genauere Analyse der Spektren zeigte die Koexistenz von den bewegungsinduzierten und *rigid-lattice* Regimen innerhalb des gleichen Spektrums. Solche Koexistenz impliziert, dass die bewegungsinduzierte Linienverschmälerung heterogen in der Probe war. Linienverschmälerung in verschiedenen räumlichen Bereichen der Probe könnte daher durch unterschiedliche mittlere Entfernung des Ti-Katalysators hervorgerufen werden. Proben mit mehr Katalysator haben somit mehr Atome in der Nähe des Katalysators und etwas niedrigere *Anfangstemperaturen*. Die Aktivierungsenergien verbunden mit Drehungen des AlH_4 Tetraeders könnten vermutlich wesentlich höher sein als die erhaltenen Werte ($H_A \approx 200$ meV, 240 meV, 260 meV bzw. für die 1, 2 und 5 Mol% Proben).

Es wurde keine bewegungsinduzierte Linienschmälerung auf allen undotierten Proben beobachtet. Außerdem konnte man bei diesen Proben (trotz ihrer Heterogenität) nur eine Relaxationsrate (Γ_1) feststellen. Die Relaxation erfolgte indirekt über Spindiffusion zwischen den sogenannten „Oberflächen“⁴ und den Atomen im Innern. Auch aufgrund der Spindiffusion waren die gefundene Aktivierungsenergien fast vernachlässigbar ($H_A \approx 56$ meV, 56 meV, 78 meV bzw. für die kugelmahlenden Proben für 5 Minuten, 30 Minuten und 12 Stunden). Diese Aktivierungsenergien könnten mit Bruchteilen der Aktivierungsenthalpien der Wasserstoffbewegung in der Nähe der Oberflächen oder Grenzflächen in Verbindung gebracht werden.

⁴„Oberflächen“ wurden als die Korn-Oberflächen und die internen Schnittstellen definiert. Im Jargon der Spindiffusion, sind diese „Oberflächen“ die Relaxationszentren.

Die Relaxationsdaten der dotierten Proben konnten nur durch eine doppelexponentielle Funktion beschrieben werden. Die *hohe* (Γ_{11}) und die *niedrige Relaxationsrate* (Γ_{12}) wurde **schnelle** beziehungsweise **langsame Komponente** genannt. Die Relaxationsraten (sowie deren entsprechende Aktivierungsenergien) der Proben ohne Katalysator waren praktisch identisch mit der *langsamem Komponente*, Γ_{12} . Daher wurde Γ_{12} mit indirekter Relaxation über Spindiffusion zwischen den sogenannten Oberflächen (ohne Katalysator) und den Atomen im Innern des Materials assoziiert.

Durch Ausschluss stand die *schnelle Relaxationskomponente* (Γ_{11}) in Beziehung zum Einfluss des Katalysators in der zugehörigen Probe. Die Relaxation der *schnellen Komponente* (Γ_{11}) trat indirekt über Spindiffusion unterhalb der *Anfangstemperatur*, genau wie in den nur kugelgemahlenen Proben, ein. Allerdings fand Spindiffusion dieses Mal zwischen den Oberflächen (aufgeladen mit Katalysator) und den Atomen im Innern statt. Oberhalb der *Anfangstemperaturen* zeigte die *schnelle Komponente* eine stärkere Temperaturabhängigkeit ($H_A \approx 770$ meV, 410 meV, 370 meV bzw. für 1, 2, 5 Mol% Proben). Diese Abhängigkeiten sollten sehr wahrscheinlich, wie in Ref. [90], in Bezug zur Beschleunigung des Wasserstoffs der Präsenz des Katalysators zugeschrieben werden. Somit stände die oben angegebene Interpretation im Einklang mit den zuvor erwähnten partiellen Bewegungslinienverschmälerungen (beobachtet bei $^1\text{H-NMR}$ -Spektren auch um *Anfangstemperaturen*).

Die Dynamik der Wasserstoff-Desorption wurde auch durch Messungen der **NMR-Spektren und der Γ_1 Relaxationsraten** auf Ti-Katalysator dotierten Proben **bei konstanter Temperatur** erforscht. Starke Veränderungen in der Form der *NMR*-Spektren der 1 Mol% Probe wurden über einen Zeitraum von 900 Minuten bei 336 K beobachtet. Ein Spektrum – beobachtet nach 900 Minuten bei 336 K – bestand aus einer einzigen Linie mit einer Linienbreite von ca. 17 kHz. Der Abbau des Wasserstoff-Gehalts in der Probe betraf die gesamte spektrale Oberfläche. Eine detaillierte Analyse der spektralen Fläche hat gezeigt, dass nach 570 Minuten nur 10 % des Wasserstoff-Gehalts desorbiert ist, d. h., dass nur etwa 20 % von NaAlH_4 in Na_3AlH_6 ungewandelt ist. Allein anhand der Form des Spektrums kann man daher nicht zwischen dem Signal von Na_3AlH_6 und dem Signal von der AlH_4 Tetraedern unterscheiden.

Die *langsame Relaxationsrate* (Γ_{12}) bei konstanter Temperatur zeigte fast keine Zeitabhängigkeit (ähnlich wie bei den Messungen in Abhängigkeit von der Temperatur). Die *schnelle Rate* (Γ_{11}) dagegen erhöht ihren Wert als Funktion der Zeit in einer Form, die asymptotisch wirkt (nach ca. 3 1/s). Die Wasserstoff-Desorption – geschätzt aus der gesamten Amplitude der Γ_1 Messungen – war etwa gleich groß wie bei den Spektren (auch bei konstanter Temperatur).

Der starke Amplitudeanstieg bei erhöhten Temperaturen von Γ_{11} kann nicht erklärt werden, wenn Wasserstoff-Desorption der einzige Prozess innerhalb der Probe wäre. Möglicherweise liegt es daran, dass die Proben mit Ti-Katalysator teilweise schon in Na_3AlH_6 und metallischen Al zerstört sind. Dies könnte im verbleibenden NaAlH_4 einen Anstieg von strukturellen Mängeln, sowie eine Reduzierung der Energiebarriere für die Drehung des AlH_4 Tetraeders (um seine C_3 -Achse) zur Folge haben. Solche Phänomene würden den Amplitudeanstieg von Γ_{11} und die bereits erwähnte schnelle Rotation des AlH_4 Tetraeder untermauern.

Acknowledgments

Diese Arbeit widme ich meinem Vater und Prof. Dr. Klaus Müller.

Ich danke meinem Doktorvater Priv.-Dozent Günter Majer für alles, was er mir beigebracht hat und, dass er dieser Arbeit zu einem guten Ende gebracht hat, trotz allem was in dieser Zeit passiert ist: Laborschließung, Sektionsänderung usw., sowie die Geburt von meiner Tochter.

Prof. Dr. Joachim Spatz danke ich dafür, dass er mir die Möglichkeit gegeben hat, meine Doktorarbeit beenden zu können.

Herrn Prof. Gert Denninger danke ich für seine Bereitschaft, den Mitbericht zu übernehmen, sowie für seine Korrekturen. Ich danke ihm darüber hinaus für seine Vorlesungen des Graduiertenkollegs Magnetische Resonanz, die stets voller Ideen, Enthusiasmus und vielen mag-net(t)-ischen Momenten steckten.

An meine virtuellen Doktor-Väter geht ein ganz besonderer Dank: Ohne Dr. Lothar Schimmele wäre diese Arbeit nie fertig geworden. Prof. Dr. Rainer Kimmich danke ich für seine liebevolle Art und dafür, dass ich ihn stets mit meinen Fragen löchern durfte. Dr. Aswin Verhoeven danke ich dafür, dass er stets bereit war, mir zu helfen.

Prof. Emil Roduner und den weiteren Professoren des Graduiertenkollegs danke ich für alles, was ich im Graduiertenkolleg Magnetische Resonanz lernen durfte. Ganz besonders Prof. Dr. Klaus Müller danke ich für seine Betreuung und seinen schwarzen Humor. Wir werden ihn vermissen. Von seiner ehemaligen Gruppe danke ich Dr. Fabrizia Poli, Matthias Abele und Dr. Otgonuu Tsetsgee.

Dr. Maximilian Fichtner, Dr. Oliver Kircher, Dr. Christoph Frommen und Dr. Wiebke Lohstroh danke ich dafür, dass Sie mir in allen Materialfragen sogar am Wochenende zur Seite gestanden und mir die Proben überlassen haben.

Ahmad Telfah aus meinem Labor danke ich dafür, dass er ein für mich so exzellenter Arbeitskollege war und mich bei der Schließung des Labors tatkräftig unterstützt hat. Dr. Eva Stanik danke ich für ihre Hinweise zum Thema NMR, wodurch es mir möglich war, nahtlos an ihre Arbeit anzuknüpfen.

Aus dem MPI-FKF danke ich Dr. Ivan Halasz für seine Hilfe.

CONACyT, DAAD und der DFG danke ich für die mir gewährten Stipendien.

Allen Kollegen und Mitarbeitern, die mir bei den zahlreichen Pannen meines Spektrometers geholfen haben, danke ich von ganzem Herzen, vor allem den Mitarbeitern des Tieftemperaturservices, Peter Gorzellik von der Elektronikwerkstatt sowie allen Mitarbeiterinnen der Feinmechanischen Werkstatt.

Danken will ich allen Frauen, die mich auf diesem Weg begleitet haben, und die für mich ein Beispiel sind. An erster Stelle danke ich meiner Mutter und meiner Schwester, meiner mexikanische Professorin Cati Stern, Jutta Weber-Bock (auch für die Korrektur meiner deutschen Texte), Anke Geigle, Dr. Nadine Walters, Dr. Esther Barena und Marion Kelsch (für ihre Unterstützung, ihr Vertrauen und ihren Optimismus in der letzten Phase meiner Arbeit).

Ich danke all den Freunden und Kollegen, die mir sowohl in glücklichen, als auch frustrierenden Zeiten Halt und Unterstützung gegeben haben, insbesondere den Mitarbeitern der EDV-Abteilung – meiner Familie im Institut – Michael Krech, Wolfgang Hägele, Heinz Zapatito und Franz-Werner Gergen.

Schließlich danke ich allen meinen Brüdern dafür, dass jeder auf seine Weise ein gutes Beispiel für mich ist. Vor allen Dingen danke ich meinem Bruder Juan für seine Unterstützung bei der Revision der englischen Texte und seinen Überlebenstipps für das Land der „blonden Lulatsche“. Meiner deutschen Familie danke ich ebenfalls, besonders Heidi und Carlitos. Allen Freunden danke ich, dass sie immer bei mir waren, auch wenn einige weit weg sind.

Zum Schluss danke ich meiner Tochter Maji und meinem Ehemann Cordi Just für die Kraft und Motivation, um weiterarbeiten zu können.

Da meine Familie ihre Deutschkenntnisse wahrscheinlich noch immer nicht perfektioniert hat, wiederhole ich etwas verkürzt noch einmal auf Spanisch: A mi padre, a quien por culpa de este trabajo interminable no pude despedirme. Igualmente al Prof. Dr. Klaus Müller. Le agradezco a toda la gente que en el intituto que me ayudo. A mi nena y a mi güerito cuerpo de uva les doy las gracias por darme la fuerza para seguir luchando hasta al final. En general a las mujeres que han estado a mi alrededor, sobretodo a mis viejas (mi mamá y mi hermana Lupita) por su ejemplo de lucha y su cariño. A todos mis hermanos por ser, cada uno a su manera, un ejemplo a seguir. En especial a Juan por sus correcciones a mi flido inglés y por convencerme que en estas tierras de güeros "Si se puede". Y por último a los cuates.

Bibliography

- [1] L. Schlapbach and A. Züttel, “Hydrogen-storage materials for mobile applications,” Nature, vol. 414, pp. 353–358, 2001.
- [2] A. Züttel, “Materials for hydrogen storage,” Materials today, vol. 6, pp. 24–33, 2003.
- [3] A. Heinzel, F. Mahlendorf, and J. Roes, Brennstoffzellen. C. F. Müller Verlag, 2005.
- [4] U. Eberle, “Hydrogen storage-technology status and research needs,” in H-Workshop, 361. WE-Heraus Seminar, (www.h-workshop.uni-konstanz.de), 2006.
- [5] HONDA, Honda Fuel Cell Power.
<http://world.honda.com/FuelCell/FCX/overview/layout..>, 2008.
- [6] G. Majer, Die Methoden der Kernspinresonanz zum Studium der Diffusion von Wasserstoff in Metallen und intermetallischen Verbindungen (Habilitationsschrift). Cuvillier Verlag Göttingen, 2000.
- [7] D. G. Westlake, “Site occupancies and stoichiometries in hydrides of intermetallic compounds: Geometric considerations,” J. of Less-Common Metal, vol. 90, pp. 251–273, 1983.
- [8] E. Stanik, Dynamik von Wasserstoff in nanokristallinen Systemen. PhD thesis, Universität Stuttgart, 2004.
- [9] B. Sakintuna, F. Lamari-Darkrim, and M. Hirscher, “Metal hydride materials for solid hydrogen storage: A review,” International Journal of Hydrogen Energy, vol. 32, pp. 1121–1140, 2007.
- [10] M. Fichtner and O. Fuhr, “Synthesis and structure of magnesium alanate and two solvent adducts,” J. Alloys Compd., vol. 345, pp. 286–296, 2002.
- [11] M. Fichtner, O. Fuhr, and O. Kircher, “Magnesium alanate-a material for reversible hydrogen storage?,” J. Alloys Compd., vol. 356-357, pp. 418–422, 2003.
- [12] B. Bogdanović and M. Schwickardi, “Ti-doped alkali metal aluminium hydrides as potential novel reversible hydrogen storage material,” J. Alloys Compd., vol. 253-254, pp. 1–9, 1997.
- [13] M. E. Arroyo y de Dompablo and G. Ceder, “First principles investigations of complex hydrides AMH_4 and A_3MH_6 ($A = Li, Na, K$ and $M = B, Al, Ga$) as hydrogen storage systems,” J. Alloys Compd., vol. 364, pp. 6–12, 2004.

- [14] R. L. Davis and C. H. L. Kennard, "Structure of sodium tetradeuteroborate $NaBH_4$," *J. Solid State Chem.*, vol. 59, pp. 393–396, 1985.
- [15] S. C. Chung and H. Morioka, "Thermochemistry and crystal structures of lithium, sodium and potassium alanates as determined by ab initio simulations," *J. Alloys Compd.*, vol. 372, pp. 92–96, 2004.
- [16] J.-P. Soulié, G. Renaudin, R. Černý, and K. Yvon, "Lithium boro-hydride $LiBH_4$: I. Crystal structure," *J. Alloys Compd.*, vol. 346, pp. 200–205, 2002.
- [17] G. Renaudin, S. Gomes, H. Hagemann, L. Keller, and K. Yvon, "Structural and spectroscopic studies on alkali borohydrides MBH_4 ($M = Na, K, Rb, Cs$)," *J. Alloys Compd.*, vol. 375, pp. 98–106, 2004.
- [18] P. Fischer and A. Züttel, "Order-disorder phase transition in $NaBD_4$," *Mat. Scienc. Forum*, vol. 443–444, pp. 287–290, 2004.
- [19] A. Züttel, S. Rentsch, P. Fischer, P. Wenger, P. Sudan, Ph. Mauron, and Ch. Emmenegger, "Hydrogen storage properties of $LiBH_4$," *J. Alloys Compd.*, vol. 356–357, pp. 515–520, 2003.
- [20] A. M. Soldate, "Crystal structure of sodium borohydride," *J. Amer. Chem. Soc.*, vol. 69, pp. 987–988, 1947.
- [21] Website: www.doe.gov, Energy sources. US Deparment of Energy, 2007.
- [22] U. Eberle, G. Arnold, and R. von Helmolt, "Hydrogen storage in metal-hydrogen systems and their derivatives," *J. Power Sources*, vol. 154, pp. 456–460, 2006.
- [23] K. J. Gross, S. Guthrie, S. Takara, and G. Thomas, "In-situ X-ray diffraction study of the decomposition of $NaAlH_4$," *J. Alloys Compd.*, vol. 297, pp. 270–281, 2000.
- [24] J. W. Lauer, D. Dougherty, and P. J. Herley, "Sodium tetrahydroaluminate," *Acta Cryst.*, vol. B35, pp. 1454–1456, 1979.
- [25] V. K. Bel'skii, B. M. Bulychev, and A. V. Golubeve, "A redetermination of the structure of $NaAlH_4$," *Russ. J. Inorg. Chem.*, vol. 28, pp. 1528–1529, 1983.
- [26] V. Ozolins, E. H. Majzoub, and T. J. Udovic, "Electronic structure and Rietveld refinement parameters of Ti -doped sodium alanates," *J. Alloys Compd.*, vol. 375, pp. 1–10, 2004.
- [27] B. C. Hauback, H. W. Brinks, C. M. Jensen, K. Murphy, and A. J. Maeland, "Neutron diffraction structure determination of $NaAlD_4$," *J. Alloys Compd.*, vol. 358, pp. 142–145, 2003.
- [28] E. Rönnebro, D. Noréus, K. Kadir, A. Reiser, and B. Bogdanović, "Investigations of the perovskite related structures of $NaMgH_3$, $NaMgF_3$ and Na_3AlH_6 ," *J. Alloys Compd.*, vol. 299, pp. 101–106, 2000.
- [29] H. Yukawa, N. Morisaku, Y. Li, K. Komiya, R. Rong, Y. Shinzato, R. Sekine, and M. Moringa, "Raman scattering and lattice stability of $NaAlH_4$ and Na_3AlH_6 ," *J. Alloys Compd.*, vol. 446–447, pp. 242–247, 2007.

- [30] R. A. Zidan, S. Takara, A. G. Hee, and C. M. Jensen, "Hydrogen cycling behavior of zirconium and titanium-zirconium-doped sodium aluminum hydride," *J. Alloys Compd.*, vol. 285, pp. 119–122, 1999.
- [31] B. Bogdanović, R. A. Brand, A. Marjanović, M. Schwickardi, and J. Tölle, "Metal-doped sodium aluminium hydrides as potential new hydrogen storage materials," *J. Alloys Compd.*, vol. 302, pp. 36–58, 2000.
- [32] T. Kiyobayashi, S. S. Srinivasan, D. Sun, and C. M. Jensen, "Kinetic study and determination of the enthalpies of activation of the dehydrogenation of titanium- and zirconium-doped $NaAlH_4$ and Na_3AlH_6 ," *J. Phys. Chem. A*, vol. 107, pp. 7671–7674, 2003.
- [33] G. P. Meisner, G. G. Tibbetts, F. E. Pinkerton, C. H. Olk, and M. P. Balogh, "Enhancing low pressure hydrogen storage in sodium alanates," *J. Alloys Compd.*, vol. 337, pp. 254–263, 2002.
- [34] G. Sandrock, K. Gross, G. Thomas, C. Jensen, D. Meeker, and S. Takara, "Engineering considerations in the use of catalyzed sodium alanates for hydrogen storage," *J. Alloys Compd.*, vol. 330–332, pp. 696–701, 2002.
- [35] G. Sandrock, K. Gross, and G. Thomas, "Effect of *Ti*-catalyst content on the reversible hydrogen storage properties of the sodium alanates," *J. Alloys Compd.*, vol. 339, pp. 299–308, 2002.
- [36] M. Fichtner, O. Fuhr, O. Kircher, and J. Rothe, "Small *Ti* clusters for catalysis of hydrogen exchange in $NaAlH_4$," *Nanotechnology*, vol. 14, pp. 778–785, 2003.
- [37] B. Bogdanović, M. Felderhoff, F. Kaskel, A. Pommerin, K. Schlichte, and F. Schüth, "Improved hydrogen storage properties of *Ti*-doped sodium alanate using titanium nanoparticles as doping agents," *Adv. Mater.*, vol. 15, pp. 1012–1015, 2003.
- [38] E. H. Majzoub and K. J. Gross, "Titanium-halide catalyst-precursors in sodium aluminum hydrides," *J. Alloy Compd.*, vol. 356–357, pp. 363–367, 2003.
- [39] H. W. Brinks, C. M. Jensen, S. S. Srinivasan, B. C. Hauback, D. Blanchard, and H. Murphy, "Synchrotron X-ray and neutron diffraction studies of $NaAlH_4$ containing *Ti* additives," *J. Alloys Compd.*, vol. 376, pp. 215–221, 2004.
- [40] J. Íñiguez and T. Yildirim, "First-principles study of *Ti*-doped sodium alanate surfaces," *App. Phys. Lett.*, vol. 86, pp. 103109:1–3, 2005.
- [41] E.-K. Lee, Y. W. Cho, and J. K. Yoon, "Ab-initio calculation of titanium solubility in $NaAlH_4$ and Na_3AlH_6 ," *J. Alloys Compd.*, vol. 416, pp. 245–249, 2006.
- [42] H. W. Brinks, B. C. Hauback, S. S. Srinivasan, and C. M. Jensen, "Synchrotron X-ray studies of $Al_{1-y}Ti_y$ formation and re-hydriding inhibition in *Ti*-enhanced $NaAlH_4$," *J. Phys. Chem. B*, vol. 109, pp. 15780–15785, 2005.
- [43] K. J. Gross, G. J. Thomas, and C. M. Jensen, "Catalyzed alanates for hydrogen storage," *J. Alloys Compd.*, vol. 330–332, pp. 683–690, 2002.

- [44] S. S. Srinivasan, H. W. Brinks, B. C. Hauback, D. Sun, and C. M. Jensen, “Long term cycling behavior of titanium doped $NaAlH_4$ prepared through solvent mediated milling of NaH and Al with titanium dopant precursors,” *J. Alloys Compd.*, vol. 377, pp. 283–289, 2004.
- [45] D. Sun, S. S. Srinivasan, G. Chen, and C. M. Jensen, “Rehydrogenation and cycling studies of dehydrogenated $NaAlH_4$,” *J. Alloys Compd.*, vol. 373, pp. 265–269, 2004.
- [46] V. P. Balema, J. W. Wiench, K. W. Dennis, M. Pruski, and V. K. Pecharsky, “Titanium catalyzed solid-state transformation in $LiAlH_4$ during high-energy ball-milling,” *J. Alloys Compd.*, vol. 329, pp. 108–114, 2001.
- [47] J. W. Wiench, V. P. Balema, V. K. Percharski, and M. Pruski, “Solid-state ^{27}Al NMR investigation of thermal decomposition of $LiAlH_4$,” *J. of Solid State Chem.*, vol. 177, pp. 648–653, 2004.
- [48] M. Mamatha, B. Bogdanović, M. Felderhoff, A. Pommerin, W. Schmidt, F. Schüth, and C. Wiedenthaler, “Mechanochemical preparation and investigation of properties of magnesium, calcium and lithium-magnesium alanates,” *J. Alloy Compd.*, vol. 407, pp. 78–86, 2006.
- [49] J. Senegas, A. M. Villepastour, and B. Bonnetot, “Etude par RMN de la structure dynamique de l’alanate Na_3AlH_6 ,” *J. Phys. Chem. Solids*, vol. 42, pp. 1061–1069, 1981.
- [50] G. Majer, E. Stanik, L. E. Valiente Banuet, F. Grinberg, O. Kircher, and M. Fichtner, “Effects of catalysts on the dehydridding of alanates monitored by proton-NMR,” *J. Alloys Compd.*, vol. 404-406, pp. 738–742, 2005.
- [51] M. H. W. Verkuijlen, P. J. M. van Bentum, E. R. H. van Eck, W. Lohstroh, M. Fichtner, and A. P. M. Kentgens, “Wide-line solid state NMR characterization of sodium alanates,” *J. Phys. Chem. C*, vol. 113, pp. 15467–15472, 2009.
- [52] B. Bogdanović, M. Felderhoff, M. Germann, M. Härtel, A. Pommerin, F. Schüth, C. Weidenthaler, and B. Zibrowius, “Investigation of hydrogen discharging and recharging processes of Ti -doped $NaAlH_4$ by X-ray diffraction analysis (XRD) and solid-state NMR spectroscopy,” *J. Alloys Compd.*, vol. 350, pp. 246–255, 2003.
- [53] E. H. Majzoub, J. L. Herberg, R. Stumpf, S. Spangler, and R. S. Maxwell, “XRD and NMR investigation of Ti-compound formation in solution-doping of sodium aluminum hydrides: solubility of Ti in $NaAlH_4$ crystals grown in THF,” *J. Alloy Compd.*, vol. 394, pp. 265–270, 2005.
- [54] J. L. Herberg, R. S. Maxwell, and E. H. Majzoub, “ ^{27}Al and 1H MAS NMR and ^{27}Al multiple quantum studies of Ti-doped $NaAlH_4$,” *J. Alloy Compd.*, vol. 417, pp. 39–44, 2006.
- [55] V. P. Tarasov and G. A. Kirakosyan, “Lattice vibrations and barriers to hindered rotation in sodium tetrahydroaluminate and tetradeuteroaluminate as determined by NMR,” *Russ. J. Inorg. Chem.*, vol. 42, pp. 1223–1227, 1997.
- [56] K. Schmidt-Rohr, “A double-quantum solid-state NMR technique for determining torsion angles in polymers,” *Macromolecules*, vol. 29, no. 11, pp. 3975–3981, 1996.

- [57] K. Schmidt-Rohr, "Complete dipolar decoupling of ^{13}C and its use in two-dimensional double-quantum solid-state NMR for determining polymer conformations," *J. Magn. Res.*, vol. 131, pp. 209–217, 1998.
- [58] A. Maus, C. Hertlein, and K. Saalwachter, "A robust proton NMR method to investigate hard/soft ratios, crystallinity, and component mobility in polymers," *Macromol. Chem. Phys.*, vol. 207, no. 13, pp. 1150–1158, 2006.
- [59] R. Kimmich, *NMR: Tomography, diffusometry, relaxometry*. Springer, 1997.
- [60] M. H. Levitt, *Spin dynamics: Basics of NMR*. Great Britain: Wiley, 2005.
- [61] E. L. Hahn, "Spin echoes," *Phys. Rev.*, vol. 80, no. 4, pp. 580–601, 1950.
- [62] W.-K. Rhim, A. Pines, and J. S. Waugh, "Time-reversal experiments in dipolar-coupled spin systems," *Phys. Rev. B*, vol. 3, no. 3, pp. 684–696, 1971.
- [63] W.-K. Rhim and H. Kessemeier, "Transverse-magnetization recovery in the rotating frame," *Phys. Rev. B*, vol. 3, no. 11, pp. 3655–3661, 1971.
- [64] S. Matsui, "Solid-state NMR imaging by magic sandwich echoes," *Chem. Phys. Rev.*, vol. 179, no. 1,2, pp. 187–190, 1991.
- [65] R. C. Bowman, Jr. and W.-K. Rhim, "A simple magic-echo sequence for second-moment measurements," *J. Mag. Res.*, vol. 49, pp. 93–98, 1982.
- [66] K. Takegoshi and C. A. McDowell, "A "magic echo" pulse sequence for the high-resolution NMR spectra of abundant spins in solids," *Chem. Phys. Letters*, vol. 116, no. 2–3, pp. 100–104, 1985.
- [67] R. R. Ernst, G. Bodenhausen, and A. Wokaun, *Principles of NMR in one and two dimensions*. Clarendon Pr., 1994.
- [68] G. Jeschke, *Structure determination II (EPR and NMR)*. www.mpiip-mainz.mpg.de/jeschke/lect_NMR_EPR.html, 2004.
- [69] M. Bak, J. T. Rasmussen, and N. C. Nielsen, "SIMPSON: A general simulation program for solid-state NMR spectroscopy," *J. Mag. Res.*, vol. 147, pp. 296–300, 2000.
- [70] M. Bak, R. Schultz, T. Vosegaard, and N. C. Nielsen, "Specification and visualization of anisotropic interaction tensor in polypeptides and numerical simulations in biological solid-state-NMR," *J. Mag. Res.*, vol. 154, pp. 28–45, 2002.
- [71] T. Vosegaard and N. C. Nielsen, "Towards high-resolution solid-state NMR on large uniformly ^{15}N - and [$^{13}\text{C}, ^{15}\text{N}$]-labeled membrane proteins in oriented lipid bilayers," *J. Biomolecular NMR*, vol. 22, pp. 225–247, 2002.
- [72] T. Vosegaard, A. Malmendal, and N. C. Nielsen, "The Flexibility of SIMPSON and SIMMOL for numerical simulations in solid- and liquid-state NMR spectroscopy," *Monatshefte für Chemie*, vol. 133, pp. 1555–1574, 2002.

- [73] J. H. van Vleck, "The dipolar broadening of magnetic resonance lines in crystals," *Phys. Rev.*, vol. 74, no. 9, pp. 1168–1183, 1948.
- [74] A. Abragam, *Principles of nuclear magnetism*. Oxford University Press, 1961.
- [75] M. Mehring and V. A. Weberruß, *Object-oriented magnetic resonance: Classes and objects, calculations and computations*. Academic Press, 2001.
- [76] N. Bloembergen, E. M. Purcell, and R. V. Pound, "Relaxation effects in nuclear magnetic resonance absorption," *Phys. Rev.*, vol. 73, no. 7, pp. 679–712, 1948.
- [77] D. Wolf, ed., *Spin-temperature and nuclear-spin relaxation in matter*. Clarendon Press, 1979.
- [78] G. J. Thomas, K. J. Gross, N. Y. C. Yang, and C. Jensen, "Microstructural characterization of catalyzed $NaAlH_4$," *J. Alloys Compd.*, vol. 330–332, pp. 702–707, 2002.
- [79] J. D. van Beek, "matNMR: A flexible toolbox for processing, analyzing and visualizing magnetic resonance data in Matlab.," *J. Magn. Res.*, vol. 187, pp. 19–26, 2007.
- [80] S. K. Brady, M. S. Conradi, G. Majer, and R. G. Barnes, "Proton magnetic resonance spectra of YH_3 and LuH_3 ," *Phys. Rev. B*, vol. 72, no. 21, pp. 214111:1–4, 2005.
- [81] A. D. S. Telfah, "NMR studies of hydrogen in the trihydrides of yttrium and lutetium," Master's thesis, Universität Stuttgart, 2003.
- [82] G. Majer, A. Telfah, and F. Grinberg, "Unusual doublet structure in proton magnetic-resonance spectra of yttrium and lutetium trihydrides," *Phys. Rev. B*, vol. 70, pp. 134111:1–6, 2004.
- [83] P. Canton, M. Fichtner, C. Frommen, and A. Léon, "Synchrotron X-ray studies of Ti-doped $NaAlH_4$," *J. Phys. Chem. B*, vol. 110, pp. 3051 – 3054, 2006.
- [84] I. J. Lowe and R. E. Norberg, "Free-induction decays in solids," *Phys. Rev.*, vol. 107, no. 1, pp. 46–61, 1957.
- [85] R. J. Barlow, *Statistics: A guide to use of statistical methods in the physical sciences*. Wiley, 1997.
- [86] J. C. Lindon, G. E. Tranter, and J. L. Holmes, eds., *Encyclopedia of spectroscopy and spectrometry*, pp. 1048–1057. Academic Press, 2000.
- [87] T. C. Farrar and E. D. Becker, *Pulse and Fourier transform NMR: Introduction to theory and methods*. Academic Press, 1971.
- [88] D. M. Grand, ed., *Encyclopedia of nuclear magnetic resonance*, vol. 7, ch. Spin diffusion in solids, pp. 4518–4524. Wiley, 1996.
- [89] V. J. McBrierty and D. C. Douglass, "Recent advances in the NMR of solid polymers," *J. Polym. Sci.: Macromol. Rev.*, vol. 16, pp. 295–366, 1981.
- [90] D. C. Douglass and G. P. Jones, "Nuclear magnetic relaxation of *n*-Alkanes in the rotating frame," *J. Chem. Phys.*, vol. 45, no. 3, pp. 956–963, 1966.

- [91] J. Shinar, D. Davidov, and D. Shaltiel, "Proton NMR study of diffusion in continuous, nonstoichiometric metal-hydrogen systems: HfV_2H_x and ZrV_2H_x ," Phys. Rev. B, vol. 30, no. 11, pp. 6331–6341, 1984.
- [92] J. T. Markert, E. J. Cotts, and R. M. Cotts, "Hydrogen diffusion in the metallic glass a- $Zr_3RhH_{3.5}$," Phys. Rev. B, vol. 37, no. 11, pp. 6446 – 6452, 1988.
- [93] A. V. Skripov, S. V. Rychkova, M. Y. Belyaev, and A. P. Stepanov, "NMR study of hydrogen motion in hydrogen-stabilized C15-type compounds $ZrTi_2H_x$," Solid State Commun., vol. 71, no. 12, pp. 1119–1121, 1989.
- [94] L. E. Valiente-Banuet, G. Majer, and K. Müller, "Proton NMR studies of the $NaAlH_4$ structure," J. Magn. Res., vol. 200, no. 2, pp. 280–284, 2009.
- [95] L. E. Valiente-Banuet, G. Majer, and K. Müller, "Erratum to 'Proton NMR studies of the $NaAlH_4$ structure,'" J. Magn. Res., vol. 205, p. 180, 2010.

Curriculum vitae

Name: Valiente Banuet, Laura Esther
 Date and place of birth: April 7th, 1975, Mexico City
 Gender: Female
 Nationality Mexican

Education and professional experience

- 03/2013 Ph.D Exam
- 10/2011 – 02/2012 Leader of tutorial lesson (in german *Übungsgruppenleiter*)
“*Mathematische Methoden der Physik*”, University of Stuttgart
- 08/2010 Birth of my daughter Maja (Baby break).
- 09/2006 Recognition of the Mexican physics study.
Report of activities (*Diplomarbeit*): “Characterization of the dehydrogenation of alanates with different catalysts monitored by proton NMR”.
- 04/2004 Exam of the “Solid State Physics” Lecture.
- 07/2003 Exam of German licentiate degree (*Diplom*).
- 05/2003 Admision Application for PhD at Stuttgart University,
Germany.
- 05/2003 – 10/2007 Attendance at the *Graduiertenkolleg Magnetische Resonanz (GKMR)*,
University of Stuttgart
- 2004 Stundents speaker *GKMR*
- 10/2002 – 04/2003 Attendance at the program “Bonn International Graduate Students”.
- 06/1993 – 06/2002 Physics studies at the National University of Mexico (*UNAM*).
- 11/1999 – 06/2000 Obligatory social service.
- 08/1990 – 06/1993 High School.

Stuttgart, 21st June 2013.

Laura Esther Valiente Banuet.